TOPOLOGICAL PHASES OF MATTER: CLASSIFICATION, REALIZATION AND APPLICATION

by

Dong-Ling Deng

A dissertation submitted in partial fulfillment
of the requirements for the degree of
Doctor of Philosophy
(Physics)
in the University of Michigan
2015

Doctoral Committee:

Professor Luming Duan, Chair
Assistant Professor Emanuel Gull
Professor Alex Kuzmich
Professor Duncan G. Steel
Assistant Professor Kai Sun

To my parents Liu-Xing Deng and Jin-Rong Deng

ACKNOWLEDGMENTS

First and foremost, I would like to immensely acknowledge my advisor, Professor Luming Duan, for his invaluable guidance, endless inspiration, and generous supports during my last five years at Michigan. To me, Luming is not only a tremendous advisor, but also an awesome mentor, a brilliant collaborator and the ultimate physicist. He keeps surprising me by his broad knowledge, great taste and sharp insight in physics. Whatever topic I bring to him, he has the magic to catch the essential ideas immediately. As a pure physicist, Luming keeps a low profile and dedicates all of his time and energy to research. His humble personality and great dedication to physics have been essential in shaping me as a scientist. I feel very fortunate and blessed to have him as my advisor.

I am also grateful to the other members of my thesis committee, Prof. Duncan Steel, Prof. Kai Sun, Prof. Alex Kuzmich, and Prof. Emanuel Gull. They are always very nice and patient whenever I stop by their offices or labs to have an impromptu discussion. In the last two years, I have had a lot of inspiring discussions with Kai. Much of my knowledge about fractional Chern insulators and Green's function is derived from these discussions. Our collaborations are both fun and fruitful.

Nearly eight years ago, I joined Prof. Mo-Lin Ge and Prof. Jing-Ling Chen's group at Chern Institute of Mathematics as a master student majored in theoretical physics. I started my very first research project in quantum information science under the supervision of my master advisor

Prof. Jing-Ling Chen. This is the start point of my physics career. For countless times, Jing-Ling came into my office and taught me on a piece of paper how to do complex calculations and how to interpret the physics from these calculations. I deeply thank Mo-Lin and Jing-Ling for bringing me into physics and for their persistent encouragement and support.

I have also benefited from numerous collaborations and discussions outside Michigan. I would like to thank, in particular, Prof. Choo Hiap Oh at National University of Singapore. Visiting his group in 2009 was a milestone for my study and research. It was during this visit that I became interested in topological phases of matter. Choo Hiap's everlasting encouragement and support are the driving force along the way to my dream in physics. I thank Prof. Gerardo Ortiz for his hospitality at Indiana University and for teaching me to think critically. I am also greatly indebted to Prof. Congjun Wu at UC San Diego, Prof. Shiliang Zhu at South China Normal University, Prof. Leong Chuan Kwek at Centre for Quantum Technologies, Prof. Kihwan Kim at Tsinghua University, Prof. Tzu-Chieh Wei at Stony Brook University and Prof. Shijian Gu at the Chinese University of Hong Kong for their kind invitation, warm hospitality and continuous support and encouragement. In addition, I have been extremely fortunate to discuss or collaborate with Prof. Jason Alicea and Prof. Xie Chen at Caltech, Prof. Joel Moore at Berkeley, Prof. Liang Jiang at Yale, Prof. Xiao-Gang Wen at MIT, Prof. Mark S. Rudner at Niels Bohr Institute, and Prof. Joseph Maciejko at Alberta. I thank them deeply for sharing their ingenious ideas with me and for their patience and time in helping me clarify my confusions.

It has been an immense pleasure to work with other members in Luming's group. I feel extremely lucky to have Mr. Shengtao Wang as a ultimate friend and a terrific collaborator. From countless rewarding discussions in Randall 4245 to unexpected lunch at the U.S. Capitol to delicious hot pot every restaurant near Tsinghua to exhausting battle in the Ann Arbor badminton tournaments, Shengtao has made the last three years of my graduate school simply the most precious memories.

Most of the results presented in this thesis are collaborations with him. I remember the pleasant years sharing an office with Dr. Zhexuan Gong, when he taught me a lot about time crystals and trapped ions. Dr. Yang-Hao Chan picked me up at the airport when I first came to Michigan. He and Dr. Chao Shen answered me many "naive" questions on numerical simulations and cold atoms. I am also grateful to many other former and current group members: Zhen Zhang, Yue Wu, Yong-Jian Han, Wei Yi, Zhaohui Wei, Zhangqi Yin, Tanvi Gujarati, Zhengyu Zhang, and Jiangmin Zhang.

My research has benefited a lot from many people in other areas as well: Prof. Yaoyun Shi and Dr. Carl Miller at UM EECS have enlightened me about the security issues in quantum key distributions and random number generations; I learnt the basics of Riemannian geometry from Prof. Zuoqing Wang; My knowledge in algebraic topology and K-theory comes largely from the discussions with Prof. Dylan Thurston at Indiana University. In addition, I would like to acknowledge several other mathematicians, including Prof. Zhengqiu Zhang and Prof. Duanzhi Zhang, for teaching me math and for sharing their mathematical intuitions.

Undoubtedly, any of my progress made in the last five years is also heavily based on the constant support from my friends. In particular, I thank Mr. Ming-Guang Hu for his hospitality at JILA and for explaining the idea of cooling molecules by chemical reactions; I thank Prof. Xiong-Jun Liu for answering my question on spin-orbit coupling and for inviting me to visit Peking University; I thank Dr. Norman Yao for not only teaching me many-body localization physics, but also playing ping pong and badminton with me. I acknowledge many others of my friends, including but not limitted to, Hok Chuen (Tom) Cheng, Xiao-Peng Li, Xin Liu, Chun-Feng Wu, Si-Xia Yu, Qing Chen, Peng-Hui Yao, Zhao-Hui Wei, Rahul Datta, Mile Gu, Yi Li, Zhong Wang, Zheng-Xin Liu, Lin Li, Skyler Degenkolb, Yun Suk Eo, Yuanyuan Zhang, Yang Ming, Bob Zheng, Tianpei Xie, Hao Sun, Chong Zu, Xiuying Chang, Wei-Ran Huang, Zhou Zhou, Hsiang-Hsuan Hung, Tyler

Hill, Hong-Chen Jiang, Daniel Shafer, S. Seckin Senlik, Bo Zhang, and Lei Wang.

Last but not least, I would like to thank my parents for their persistent love and support. Although they may never understand what I am doing, they always stand by and encourage me to pursuit my dream in physics. Besides, I thank my younger brother Mr. Quling Deng and sister Miss. Lingyan Deng and my fiancee Miss. Zisui Zhou. The cold winters at Ann Arbor have only been bearable because of their love and encouragement.

TABLE OF CONTENTS

LIST OF FIGURES

LIST OF TABLES

LIST OF APPENDICES

ABSTRACT

The recent discovery of topological insulators has led to a tremendous interest in the exploration of topological phases of matter which do not fit into Landau's symmetry breaking paradigm. Numerous exotic topological materials are theoretically predicted. Some of them have been experimentally reported, but many remain not. In this thesis, we explore topological phases of matter from three aspects: their classification, realization and application.

We first review some basic classification theories, which provide us a "big picture" and lay the foundation for the rest of the thesis. We then move on to propose a systematic method based on quaternion algebra to construct toy tight-binding Hamiltonians for all the exotic phases in a recently developed periodic table for topological insulators and superconductors. We also introduce two peculiar families of topological phases that are beyond the table—the Hopf and four-dimensional topological insulators without time reversal symmetry. Prototypical Hamiltonians are constructed and their topological properties, such as robust edge states, are numerically studied.

Motivated by rapid experimental progress in engineering spin-orbit coupling and artificial gauge field, we continue the thesis by proposing a feasible experimental scheme to realize a three-dimensional chiral topological insulator with cold fermionic atoms in an optical lattice. To unambiguously probe topological phases for cold atoms, we also bring forth systematic and generic methods to measure the characteristic topological invariants, for both free and strongly interacting

systems. Moreover, we demonstrate that a kaleidoscope of knot and link structures is encoded in the spin texture of Hopf insulators and show how to observe different knots and links in cold atoms via time-of-flight images.

The last part of the thesis is about the application of topological materials. After a demonstration of how to create, braid and detect Majorana fermions with cold atoms, we put forward a proposal to construct a self-test quantum random number generator by using Majorana fermions. Majorana random number generators are able to generate certifiable true random numbers with unconditional security. They offer a new perspective to the utilization of topological materials and may have vital applications in cryptography and related areas.

CHAPTER I

Introduction

1.1 Background

In condensed matter physics, a central task is to find out how many distinct states of matter (phases) can exist in nature. It is well known that atoms and electrons can be organized in different ways to form different states of matter, such as liquid, solid, gas, superfluid, magnet, superconductor, etc. A remarkable theory developed in the last century, which classifies these distinct phases, is Landau's symmetry-breaking theory [1–3]. According to this theory, different phases correspond to different symmetries in the organization of the constituent building blocks. As a material goes from one phase to another (i.e., undergoes a phase transition), the underlying symmetries change accordingly. For instance, a liquid has a continuous translational symmetry. It can turn into a crystal after a phase transition. The corresponding symmetry then changes from continuous translational symmetry to discrete translational symmetry. Thus, the essential difference between a liquid and a crystal is the fact that they have different symmetries in the organization of the constituent atoms, and the phase transition is essentially a transition of symmetries (symmetry breaking). Moreover, a order parameter can be established from the pattern of symmetry-breaking. It identifies the corresponding phase with a nonvanishing expectation value. Based on the order parameter, an effective

field theory (generally called Landau-Ginzburg theory) can be formulated to give a universal description of states of matter [1–3].

Landau's symmetry-breaking theory is very successful. For a long time, people believed that it can describe all possible phases of matter and all possible continuous phase transitions. However, this belief was gradually changed in the 1980s. Thanks to the discovery of integer and fractional quantum Hall effects [5, 6], physicists became to realize that symmetry alone was not sufficient to characterize all different phases. In the quantum Hall states, the bulk of the two-dimensional sample is insulating but the edge carries chiral dissipationless current with a precisely quantized Hall conductance. Different Hall states with different quantized conductance belong to different phases but have exactly the same symmetry. Thus both the integer and fractional quantum Hall state cannot be fit into Landau's paradigm and a new theory has to be established to understand these exotic phases and their transitions.

In recent years, remarkable progress has been made along this direction. Besides quantum Hall liquid, many other topological phases, such as topological band insulators and superconductors [7–9] , have been theoretically predicted [10–13] and experimentally observed [14–16]. All these phases escape Landau's paradigm and we still lack a systematic understanding of them. Motivated by all these progresses and problems, this thesis studies several important aspects of topological phases.

1.2 Outline of the dissertation

As indicated by the title, this thesis is all about topological phases of matter. We will focus on three important aspects: the classification, simulation and application of topological phases of matter. In chapter II, we introduce the concepts of symmetry protected and enriched topological phases. We

then briefly review two approaches to the classifications of these phases, one for interacting bosons and the other for free fermions. For strongly interacting bosonic systems, we mainly introduce the group cohomology approach developed by Wen *et. al* [17, 18]. For free fermionic systems, we present the periodic table for topological insulators (TIs) and superconductors (TSCs) discovered by Kitaev [19] and Schnyder *et. al* [20, 21].

Chapter III continues the discussion of the periodic table, but now centers on constructing prototypical tight-binding Hamiltonians for each nontrivial phase predicted by the table. We first introduce a general and systematic method based on the quaternion algebra [22]. Then, as examples, we use this method to construct tight-binding Hamiltonians for all the 3D topological phases in the periodic table with arbitrary integer topological invariants. These examples include spin-singlet TSCs in symmetry class CI, spin-triplet TSCs in class DIII, chiral TIs in class AIII, and Hopf insulators in class A.

In chapter IV, we introduce two classes of topological phases that are outside of the periodic table. The first class is the so called Hopf insulators in symmetry class A. We explain why Hopf insulators exist and demonstrate, based on a generalized Hopf map, how to construct a family of tight-binding Hamiltonians which realize all kinds of Hopf insulators with arbitrary integer Hopf index [23]. A geometric picture is given to analytically obtain the topological invariants for each Hamiltonian. Hopf insulator phases have topologically protected surface states and we numerically demonstrate the robustness of these topologically protected states under general random perturbations. The other class is the $\mathbb{Z}_2$ topological insulators in four dimensions. Based on the homotopy group theory, we explain why this exception exists and show how to construct a model Hamiltonian for the nontrivial phase through the suspension technique.

After we introduce the basic classification theory, we move on to discuss how to realize and detect the predicted different topological phases in chapter V–VII. To be more specific, in chapter V, we

present our result on how to implement and detect three-dimensional (3D) chiral topological insulators with cold fermionic atoms in optical lattices [24]. Unlike the conventional $\mathbb{Z}_2$ TIs protected by time reversal symmetry, the chiral TIs considered here are protected by the chiral (also known as sublattice) symmetry and belong to the symmetry class AIII with a $\mathbb{Z}$ classification. Chapter VI is dedicated to measuring topological invariants in cold atom systems [25]. This chapter can be divided into two parts. The first part deals with a general method on how to directly measure the topological invariants of Bloch bands for free fermionic systems. The second part introduces a versatile scheme to detect various topological invariants for strongly interacting systems, where the concept of Bloch bands does not apply. In chapter VII, we explore the topological properties of topological materials from a new perspective. We first show that the spin textures of Hopf insulators are highly twisted with kaleidoscopic knot and link structures encoded. Moreover, we also propose an experiment to realize Hopf insulators with ultracold fermions in optical lattices and show how to extract the Hopf invariant and the knotted spin textures form the time-of-flight imaging data.

Chapter VIII remains on the simulations of topological phases with cold atoms, but is now focused on 2D topological superconductors which can host Majorana fermions. Roughly speaking, this chapter is about how to create, braid, and detect Majorana fermions with cold atoms in optical lattices [26]. We demonstrate that the Majorana-Shockley fermions associated with line defects can be braided with non-Abelian statistics through adiabatic shift of the local chemical potentials. We also demonstate robustness of the braiding operation against practical noise and propose a scheme to measure the topological qubits using local measurement of the atom number.

In chapter IX, we propose a new possible practical application of topological phases of matter. We show that the topological manipulation of Majorana fermions alone can provide the full set of operations required to generate certified random numbers [27]. Thus a fault-tolerant quantum ran-

dom number generator might be constructed using Majorana fermions. Unlike traditional random number generators that only produce unsafe pseudo-random numbers, Majorana random number generators are able to generate certifiable true random numbers that are private and secure against even quantum adversaries. We conclude the thesis in chapter X with several future directions.

CHAPTER II

Classification of topological phases

2.1 Introduction

Topological phases of matter, such as topological insulators and superconductors [7–14, 16, 28–45], are quantum phases of matter beyond the Landau-Ginzburg symmetry-breaking paradigm. They are gapped in the bulk but have robust gapless edge states at surfaces protected by the bulk topology.

In general, topological phases of matter may be divided into two classes: the intrinsic ones and the symmetry-protected ones. Symmetry-protected topological (SPT) phases are gapped quantum phases that are protected by system symmetries and cannot be smoothly connected to the trivial phases under perturbations that respect the same kind of symmetries. They are short-range-entangled quantum phases [17, 18]. When the corresponding symmetry is broken, all these phases are smoothly connected to the trivial phase of product states. Remarkable examples of SPT phases include the Haldane phase of the spin-1 chain which is protected by the $SO(3)$ spin rotation symmetry [46, 47], and topological insulators and superconductors which are protected by the time reversal symmetry [7, 8]. For interacting bosonic systems with on-site symmetry G, distinct SPT phases can be systematically classified by $\mathbb{H}^{d+1}[G, U_T(1)]$, the Borel $(d+1)$-group cohomology

of G over the G-module $U_T(1)$ [17, 18]. While, for free fermions, the SPT phases can be systematically described by the K-theory or homotopy group theory [48], which lead to the well known periodic table for topological insulators and superconductors [19–21]. For interacting fermionic systems, a large class of SPT phases can be described by the group supercohomology theory [49] and Chern-Simons field theory [50].

Intrinsic topological (IT) phases, on the other hand, are gapped long-range-entangled phases that cannot be smoothly connected to the trivial phase even we break the symmetry. Fractional quantum Hall states [5, 51] and spin liquids [52–56] are prominent examples of this family. Unlike the SPT case, which is trivial in the bulk, intrinsic topologically ordered phases may have fractional excitations bearing fractional statistics or even non-Ablelian quasiparticles bearing non-Abelian statistics in the bulk [57]. Another distinction between SPT phases and IT phases concerns the robustness of their gapless edge states to different local perturbations. Edge states of SPT phases are only robust to local perturbations that respect the system symmetries. Nevertheless, edge states of IT phases are robust to any local perturbations that maintain the bulk energy gap. Intrinsic topological phases may be further classified according to the system symmetries, leading to the so called symmetry enriched topological (SRT) phases [58–61]. Recently, projective symmetry group was introduced to describe the SRT phases [58, 62], but a systematic understanding is still lacking.

In this chapter, we briefly review several classification theories of topological phases to introduce the general background for the whole thesis. First, we will introduce the group cohomology approach to classify interacting bosons based on Ref. [17, 18]. We then move on to the free fermionic system. The periodic table for topological insulators and superconductors discovered by Kitaev [19] and Schnyder et. al [20, 21] will be introduced here. For interacting fermionic systems, the classification is very challenging and a systematic method is still under study.

2.2 Bosonic systems

To start with, let us first introduce the concept of local unitary (LU) transformation and the definition of quantum phases. A LU transformation with depth M is a product of piecewise LU operators [17, 18]:

$$U_L = \Pi_{i=1}^{M} U_{pl}^{(i)},$$

where $U_{pl}^{(i)} = \Pi_j U_j^{(i)}$ is a piecewise LU operator with $\{U_j^{(i)}\}$ a set of unitary operators that act locally on nonoverlapping regions. We define that two gapped quantum states belong to the same quantum phase if and only if they can transform to each other through a LU transformation. Without any symmetry, quantum phases of gapped systems can be divided into two classes: short range entangled (SRE) states which can be transformed into direct product states through a LU transformation, and long range entangled (LRE) states which cannot. As all SRE states can be transformed into each other via LU transformation, they belong to the same quantum phase. However, many LRE states cannot be transformed into each other and they represent different phases. In fact, these LRE phases are nothing but the intrinsic topological phases mentioned previously.

When certain symmetry is considered, only the LU transformations that respect the symmetry can be used to connect states. In this case, even SRE states with the same symmetry can belong to different phases, leading to the so called symmetry protected topological phases. In order to classify all SPT phases, let us consider a d dimensional system with an on-site symmetry group G. We can always change a SPT state via a symmetric LU transformation to a symmetric tensor-network state of the canonical form [17, 18]. In the canonical form, the symmetry transformation

should keep the SRE state $|\Psi_{\text{SRE}}\rangle$ invariant, leading to the following equation:

$$\otimes_{\mathbf{j}} U_{\mathbf{j}} |\Psi_{\text{SRE}}\rangle \quad = \quad |\Psi_{\text{SRE}}\rangle, \tag{2.2.1}$$

where $U_{\mathbf{j}}$ forms a linear representation of the group G which generates the symmetry transformation on the effective site-$\mathbf{j}$. Thus the task of classifying SPT phases reduces to the task of finding out all the equivalent classes of pairs $(U_{\mathbf{j}}, |\Psi_{\text{SRE}}\rangle)$ that satisfy Eq. (2.2.1). However, for a general many-body system, Eq. (2.2.1) is not solvable. In Ref. [17, 18], Chen, Gu, Liu, and Wen's basic idea is, rather than to solve the above equation and find all the representative solutions directly, to explicitly construct as general as possible the solutions of this equation by using cocycles from the corresponding group cohomology $\mathbb{H}^{d+1}[G,\, U_T(1)]$. Here, we only reproduce parts of their results in Table 2.1.

While this table contains these well-known SPT phases such as the Haldane phase, it is worthwhile to point out that the above classification based on group cohomology is incomplete [63]. There exist other SPT phases that are beyond this classification [64–66].

2.3 Fermionic systems

The classification of topological phases for fermionic systems is still under intense investigation. For free fermions, a remarkable periodic table for topological insulators and superconductors has been developed recently by Kitaev [19] and Schnyder et. al [20, 21]. This table has included most of the familiar topological phases as its special elements. For strongly interacting fermionic systems, Gu and Wen have shown that a large class of interacting fermionic SPT phases can be systematically described by group supercohomology theory [49]. It is also found that there exist

Symm. group G	$d=0$	$d=1$	$d=2$	$d=3$
Z_n	Z_n	0	Z_n	0
Z_2^T	0	Z_2	0	Z_2
$Z_n \rtimes Z_2^T$	Z_n	$Z_2 \times Z_{(2,n)}$	$Z_{(2,n)}^2$	$Z_2 \times Z_{(2,n)}^2$
$Z_n \rtimes Z_2$	$Z_2 \times Z_{(2,n)}$	$Z_{(2,n)}$	$Z_2 \times Z_{(2,n)} \times Z_n$	$Z_{(2,n)}^2$
$Z_n \times Z_2^T$	$Z_{(2,n)}$	$Z_2 \times Z_{(2,n)}$	$Z_{(2,n)}^2$	$Z_2 \times Z_{(2,n)}^2$
$Z_n \times Z_m$	$Z_n \times Z_m$	$Z_{(n,m)}$	$Z_n \times Z_{(n,m)} \times Z_m$	$Z_{(n,m)}^2$
$D_2 \times Z_2^T$	Z_2^2	Z_2^4	Z_2^6	Z_2^9
$U(1)$	Z	0	Z	0
$SU(2)$	0	0	Z	0
$SO(3)$	0	Z_2	Z	0
$U(1) \times \mathrm{Trn}$	Z	Z	Z^2	Z^4
$U(1) \rtimes Z_2^T$	Z	Z_2	Z_2	Z_2^2
$U(1) \times Z_2^T \times \mathrm{Trn}$	0	Z_2^2	Z_2^4	Z_2^9
$U(1) \rtimes Z_2^T \times \mathrm{Trn}$	Z	$Z \times Z_2$	$Z \times Z_2^3$	$Z \times Z_2^8$
$SO(3) \times \mathrm{Trn}$	0	Z_2	$Z \times Z_2^2$	$Z^3 \times Z_2^3$
$U(1) \times Z_2^T \times \mathrm{Trn}$	0	Z_2^2	Z_2^5	Z_2^{12}

Table 2.1: Classification of bosonic SPT phases. SPT phases in d dimension with a on-site symmetry group G are classified by the cohomology group $\mathbb{H}^{d+1}[G, U_T(1)]$. Here Z_2^T denotes the time reversal symmetry, "Trn" represents translation symmetry, and (m,n) is the greatest common divisor of m and n [17, 18].

six interacting electronic topological insulators that have no noninteracting counterpart [67]. Here, we only briefly review the discovery of the periodic table, which will be repeatedly mentioned throughout the thesis.

The periodic table is developed in terms of the system symmetry and dimensionality. There are three generic symmetries relevant for any system, namely the time-reversal (T), particle-hole (charge conjugation C), and chiral ($S = TC$) symmetry. Let us specify the definition of these symmetries. A Hamiltonian is represented by a finite matrix $\mathscr{H}(\mathbf{k})$ in the $\mathbf{k}$ space (kernel of the Hamiltonian). It has the time reversal symmetry if there exists a unitary matrix T_m such that

$$T_m \mathscr{H}^*(\mathbf{k}) T_m^{-1} = \mathscr{H}(-\mathbf{k}). \tag{2.3.1}$$

Similarly, $\mathscr{H}(\mathbf{k})$ has the particle-hole symmetry if there is a unitary matrix C_m such that

$$C_m \mathscr{H}^*(\mathbf{k}) C_m^{-1} = -\mathscr{H}(-\mathbf{k}). \tag{2.3.2}$$

The anti-unitary nature of the time reversal and the particle-hole symmetries is manifested in the complex conjugate $\mathscr{H}^*(\mathbf{k})$ in Eqs. (2.3.1) and (2.3.2). Finally, as $S = TC$, the chiral symmetry is unitary and represented by ($S_m = T_m C_m^*$)

$$S_m \mathscr{H}(\mathbf{k}) S_m^{-1} = -\mathscr{H}(\mathbf{k}). \tag{2.3.3}$$

Pertaining to the presence or absence of these symmetries, ten classes of single-particle Hamiltonians can be specified, which is intimately related to the classification of random matrices by Altland and Zirnbauer (AZ) [68]. Based on these ten symmetry classes, a periodic table for topological insulators and superconductors can be developed by the K-theory [19] or homotopy theory [20,21].

	AZ	T	C	S	1D	2D	3D	4D	5D	6D	7D	8D
Wigner-Dyson	A	-	-	-	0	$\mathbb{Z}$	0	$\mathbb{Z}$	0	$\mathbb{Z}$	0	$\mathbb{Z}$
	AI	$+1$	-	-	0	0	0	$\mathbb{Z}$	0	$\mathbb{Z}_2$	$\mathbb{Z}_2$	$\mathbb{Z}$
	AII	-1	-	-	0	$\mathbb{Z}_2$	$\mathbb{Z}_2$	$\mathbb{Z}$	0	0	0	$\mathbb{Z}$
Chiral	AIII	0	0	1	$\mathbb{Z}$	0	$\mathbb{Z}$	0	$\mathbb{Z}$	0	$\mathbb{Z}$	0
	BDI	$+1$	$+1$	1	$\mathbb{Z}$	0	0	0	$\mathbb{Z}$	0	$\mathbb{Z}_2$	$\mathbb{Z}_2$
	CII	-1	-1	1	$\mathbb{Z}$	0	$\mathbb{Z}_2$	$\mathbb{Z}_2$	$\mathbb{Z}$	0	0	0
BdG	D	-	$+1$	-	$\mathbb{Z}_2$	$\mathbb{Z}$	0	0	0	$\mathbb{Z}$	0	$\mathbb{Z}_2$
	C	-	-1	-	0	$\mathbb{Z}$	0	$\mathbb{Z}_2$	$\mathbb{Z}_2$	$\mathbb{Z}$	0	0
	DIII	-1	$+1$	1	$\mathbb{Z}_2$	$\mathbb{Z}_2$	$\mathbb{Z}$	0	0	0	$\mathbb{Z}$	0
	CI	$+1$	-1	1	0	0	$\mathbb{Z}$	0	$\mathbb{Z}_2$	$\mathbb{Z}_2$	$\mathbb{Z}$	0

Table 2.2: Periodic table for topological insulators and superconductors [19–21]. AZ denotes the ten symmetry classes. We denote by "-" if certain symmetry is absent, and by "± 1" if this symmetry is present and its corresponding operator squares to ± 1. The symbols $\mathbb{Z}$ and $\mathbb{Z}_2$ imply that the topological phases within the given symmetry class are classified by the integer ($\mathbb{Z}$) or cyclic ($\mathbb{Z}_2$) group. The symbol "0" means that there exists no nontrivial topological phases in the given symmetry class and dimension.

Here, we reproduce this table in Table 2.2.

In order to catch a basic understanding of how this table is obtained, let us consider a generic free Hamiltonian $\mathscr{H}(\mathbf{k})$ in the momentum space. The energy spectrum is obtained by solving the Schrodinger equation

$$\mathscr{H}(\mathbf{k})|u_b(\mathbf{k})\rangle = E_b(\mathbf{k})|u_b(\mathbf{k})\rangle,$$

where b denotes the Bloch band index. Without loss of generality, we assume that m bands are filled and n bands are empty. For every momentum $\mathbf{k}$ in the Brillouin zone (BZ), let us define the

projector onto the filled Bloch bands [20]

$$P(\mathbf{k}) \;=\; \sum_{b}^{\text{filled}} |u_b(\mathbf{k})\rangle\langle u_b(\mathbf{k})|$$

and a $(m+n)\times(m+n)$ "Q matrix"

$$Q(\mathbf{k}) \;=\; \mathbf{1} - 2P(\mathbf{k}).$$

The Hermitian matrix $Q(\mathbf{k})$ captures the essential information of the Hamiltonian $\mathscr{H}(\mathbf{k})$. Thus, the classification of $\mathscr{H}(\mathbf{k})$ reduces to the classification of $Q(\mathbf{k})$. Without additional symmetry, the set of $m+n$ eigenvectors forms a unitary matrix, i.e., an element of $U(m+n)$. Also, there is a "gauge symmetry": the system is unchanged if one relabels the filled and empty bands amongst themselves. Thus, $Q(\mathbf{k})$ is actually an element of Grassmannian manifold $Q(\mathbf{k}) \in \mathbb{G}_{m,m+n} = U(m+n)/[U(m)\times U(n)]$. Noting that $\mathbf{k}$ runs over the Brillouin zone, $Q(\mathbf{k})$ can also be regarded as a map from the Brillouin zone to the Grassmannian $Q:\ \mathrm{BZ} \to \mathbb{G}_{m,m+n}$. Mathematically, distinct maps can be topologically classified by the homotopy group. It is well known in the mathematical literature that for large enough m and n

$$\pi_d(\mathbb{G}_{m,m+n}) \;=\; \begin{cases} 0 & \text{if } d \text{ is odd} \\ \mathbb{Z} & \text{if } d \text{ is even} \end{cases}.$$

As a result, for the symmetry class A in the table, we have only trivial phase in odd dimensions and an integer $\mathbb{Z}$ classification in even dimensions.

When additional symmetry is considered, extra conditions are imposed on $Q(\mathbf{k})$. This puts certain restrictions on the Grassmannian and changes the classification. Taking the symmetry class AIII

for example, it has a chiral symmetry. This symmetry requires that $Q(\mathbf{k})$ can be brought into a block off-diagonal form through basis changing

$$Q(\mathbf{k}) \;=\; \begin{pmatrix} \mathbf{0} & q(\mathbf{k}) \\ q^{\dagger}(\mathbf{k}) & \mathbf{0} \end{pmatrix},$$

where $q(\mathbf{k}) \in U(m)$ is a unitary $m \times m$ matrix. As a result, $Q(\mathbf{k})$ lives only in a subspace of the Grassmannian and the relevant homotopy group changes to

$$\pi_d[U(m)] \;=\; \begin{cases} \mathbb{Z} & \text{if } d \text{ is odd} \\ 0 & \text{if } d \text{ is even} \end{cases}.$$

This implies that in symmetry class AIII, all phases are topologically trivial in even dimensions but we have infinitely many distinct topological phases in odd dimensions. Similarly, one can obtain the results for all other symmetry classes by adding extra conditions on $Q(\mathbf{k})$ and considering the homotopy group of the resulting subspace.

The table will repeat itself in higher dimensions. Mathematically, the symmetry classes A and AIII correspond to two types of complex Clifford algebra and have a periodicity of 2 in dimensions. The rest of the classes corresponds to eight types of real Clifford algebras and have a periodicity of 8 [19]. The 2 and 8 periodicity are known as Bott periodicity in K-theory. Yet, it is important to clarify that these regular patterns only appears in the stable homotopy range, where the dimension of the classifying space is large enough (here simply means that m and n are large enough). For low dimensional classifying space, accidental exceptions will occur. The 3D Hopf insulators and 4D $\mathbb{Z}_2$ insulators in class A are such exceptions. We will discuss in more details about these exceptions in the following chapters.

CHAPTER III

Tight-binding Hamiltonians for the periodic table

3.1 Introduction

Topological insulators (TIs) and superconductors (TSCs) are symmetry protected topological phases of non-interacting fermions described by quadratic Hamiltonians [7, 8], which have robust gapless boundary modes protected by the system symmetry [18]. These protected boundary modes have exotic properties and in some cases are characterized as anyons with fractional statistics [57], which could be used for the realization of topological quantum computation [69]. Notable examples of TIs include the integer quantum Hall states [70] and the recently discovered two-dimensional (2D) quantum spin Hall states [10, 14] and the three-dimensional (3D) $\mathbb{Z}_2$ TIs [11,16,36,40]. Examples of TSCs include the 2D $p+ip$ superconductors of spinless fermions [71] and the Helium superfluid B-phase [19, 21].

It turns out that the above TI/TSC examples are just a part of a larger scheme: they sit inside a periodic table for TIs/TSCs developed according to symmetry and dimensionality of the system [19–21]. The periodic table predicts possible existence of a number of new topological phases, and

it is of great interest to search for these new phases in nature. However, the periodic table does not tell where to look for or how to realize these phases. To physically realize these exotic phases and study their properties, it is of critical importance to construct tight-binding Hamiltonians so that they could be realized in real quantum materials such as optical lattice systems [72]. So far, some clever example Hamiltonians have been found for a few new topological phases [20, 41, 73, 74], typically with the topological invariant $\Gamma = \pm 1$, but we lack a systematic method to construct tight-binding Hamiltonians for generic topological phases with arbitrary integer topological invariants.

In this chapter, we propose a general and systematic method to construct tight binding Hamiltonians for new topological phases based on the use of quaternion algebra. By this method, we construct the tight-binding Hamiltonians for all the 3D topological phases in the periodic table with arbitrary integer topological invariants, which include the spin-singlet and the spin-triplet TSCs, the chiral and the Hopf TIs as prototypical examples. For each class, the topological invariant is explicitly calculated for the constructed Hamiltonian, using both geometric analysis and numerical simulation, which confirm that we indeed realize all the topologically distinct phases in the corresponding class characterized by a topological invariant of arbitrary integer values. The construction method proposed here should also work for the 2D and 1D cases, and we believe its direct generalization to Clifford algebra should provide a powerful tool to construct tight-binding Hamiltonians for all the integer topological phases in the periodic table.

3.2 Quaternion algebra approach

Before showing the method, let us first briefly introduce the quaternion algebra $\mathbb{H}$, which is a generalization of the familiar complex algebra, with the imaginary basis-vectors extended from one ($\boldsymbol{i}$) to three ($\boldsymbol{i}, \boldsymbol{j}, \boldsymbol{k}$). The basis-vectors ($\boldsymbol{i}, \boldsymbol{j}, \boldsymbol{k}$) multiply according to the following non-commutative

product table [48]:

$$\begin{aligned} \boldsymbol{i}^2 = \boldsymbol{j}^2 = \boldsymbol{k}^2 = -1, \qquad & \boldsymbol{ij} = -\boldsymbol{ji} = \boldsymbol{k}, \\ \boldsymbol{jk} = -\boldsymbol{kj} = \boldsymbol{i}, \qquad & \boldsymbol{ki} = -\boldsymbol{ik} = \boldsymbol{j}. \end{aligned} \tag{3.2.1}$$

Any element of $\mathbb{H}$ can be expanded as $q = q_0 + q_1\boldsymbol{i} + q_2\boldsymbol{j} + q_3\boldsymbol{k}$, where q_i $(i = 0,1,2,3)$ are real numbers. Quaternion has been used recently as a tool to analyze the 3D Landau levels [75, 76].

For our purpose, it is more convenient to write q in the polar-like coordinate with $q = \rho(\cos\theta + \hat{\mathbf{a}}\sin\theta)$, where $\rho \equiv |q| = \sqrt{q_0^2 + q_1^2 + q_2^2 + q_3^2}$ is the norm of q, θ is the angle, and $\hat{\mathbf{a}} = \hat{a}_1\boldsymbol{i} + \hat{a}_2\boldsymbol{j} + \hat{a}_3\boldsymbol{k}$ with $\hat{a}_1^2 + \hat{a}_2^2 + \hat{a}_3^2 = 1$ is a unity vector denoting the direction in the imaginary space. From the definition, we immediately get

$$q^n = \rho^n(\cos n\theta + \hat{\mathbf{a}}\sin n\theta). \tag{3.2.2}$$

To construct tight-binding lattice Hamiltonians for the TIs or TSCs, we typically work in the momentum space. The Hamiltonian coefficients are taken as components q_i of a quaternion q, which in general depend on the momentum through the notation $q_i(\mathbf{k})$. In a d-dimensional $(d = 1,2,3)$ space, the momentum $\mathbf{k}$ takes values from the Brillouin zone (BZ) characterized by a d-dimensional torus $\mathbb{T}^d$. The norm $|q|$ of the quaternion q characterizes the energy scale (energy gap) of the Hamiltonian, which can be taken as 1 (the energy unit) without loss of generality, and the topological space of q is thus characterized by the sphere $\mathbb{S}^d$. The Hamiltonian with $q_i(\mathbf{k})$ as the coefficients can be considered as a map from the space $\mathbb{T}^d$ to $\mathbb{S}^d$. If this map is topologically nontrivial characterized by a topological invariant (usually taken as the winding number or Chern number) $\Gamma = 1$, geometrically (in the sense of homotopy) it means that the space $\mathbb{T}^d$ wraps around

$\mathbb{S}^d$ one time through the map. Now consider a Hamiltonian where the coefficients are taken as the components of $q^n(\mathbf{k})$. From the geometric representation of q^n in the polar coordinate in Eq. (3.2.2), if the space $\mathbb{T}^d$ wraps around $\mathbb{S}^d$ one time through the map $\mathbf{k} \to q(\mathbf{k})$ with $\Gamma = 1$, it will wrap $\mathbb{S}^d$ n times through the map $\mathbf{k} \to q^n(\mathbf{k})$ with $\Gamma = n$. So, by this quaternion-power mapping, we can construct Hamiltonians for topologically distinct new phases with arbitrary integer topological invariants. This serves as our physical intuition to construct tight-binding Hamiltonians for new topological phases. In the following, we apply this method to construction of the Hamiltonians for all the 3D topological phases in the periodic table characterized by the integer group $\mathbb{Z}$, which include the spin-singlet and the spin-triplet TSCs, the chiral and the Hopf TIs.

3.3 Examples

3.3.1 Spin-singlet TSC (class CI)

Spin singlet TSC is described by a Bogoliubov-de-Gennes (BdG) type of mean-field Hamiltonian and belongs to the symmetry class CI in the periodic table, which means the BdG Hamiltonian has both T and C symmetries with $T^2 = 1$ and $C^2 = -1$. The topological phase is characterized by a topological invariant Γ_{CI}, which takes values from $2\mathbb{Z}$ (even integers). Ref. [77] has proposed a Hamiltonian in a diamond lattice which realizes a special instance of the CI TSC with $\Gamma_{\mathrm{CI}} = \pm 2$. Here, we construct tight binding Hamiltonians which can realize all the topologically distinct phases for the CI TSC with arbitrary even integer Γ_{CI} in a simple cubic lattice. The simplified lattice geometry could be important for an experimental implementation.

To construct the BdG Hamiltonian in the momentum space, first we define a quaternion q with the

following dependence on the momentum $\mathbf{k}$

$$q = t\cos k_x - \boldsymbol{i}(\sin k_x + \sin k_y + \sin k_z) + \boldsymbol{j}\cos k_y + \boldsymbol{k}\cos k_z, \tag{3.3.1}$$

where t is a dimensionless parameter. A family of the BdG Hamiltonians can be constructed on the 3D cubic lattice with the form $H_{\mathrm{CI}} = \sum_{\mathbf{k}} \Psi^{\dagger}_{\mathbf{k}} \mathscr{H}_{\mathrm{CI}}(\mathbf{k}) \Psi_{\mathbf{k}}$ in the momentum space, where $\Psi_{\mathbf{k}} = (a_{\mathbf{k}\uparrow}, b_{\mathbf{k}\uparrow}, a^{\dagger}_{-\mathbf{k}\downarrow}, b^{\dagger}_{-\mathbf{k}\downarrow})^T$ denotes the fermionic mode operators with spin $\uparrow,\downarrow$ and momentum $\mathbf{k}$. The 4×4 Hamiltonian matrix reads

$$\mathscr{H}_{\mathrm{CI}}(\mathbf{k}) = \begin{pmatrix} \mathbf{m}\cdot\boldsymbol{\sigma} & (q^n)_3 \mathbf{I_2} \\ (q^n)_3 \mathbf{I_2} & -\mathbf{m}\cdot\boldsymbol{\sigma} \end{pmatrix}, \tag{3.3.2}$$

where $\mathbf{m} = ((q^n)_0, (q^n)_1, (q^n)_2)$ with $(q^n)_i$ denoting the ith-components of the quaternion q^n, $\mathbf{I_2}$ is the 2×2 identity matrix, and $\boldsymbol{\sigma} = (\sigma^x, \sigma^y, \sigma^z)$ are the Pauli matrices. Expressed in the real space, the Hamiltonian H_{CI} contains spin-singlet d-wave pairing described by the quaternion component $(q^n)_3$, and has local hopping and pairing terms up to the nth neighboring sites. One can check that $\mathscr{H}_{\mathrm{CI}}(\mathbf{k})$ indeed has both T and C symmetries (and thus also the chiral symmetry $S = TC$) with $T^2 = 1$ and $C^2 = -1$ (see the Appendix A for an explicit check).

Now we show that the Hamiltonian H_{CI} has topologically distinct phases depending on the parameters n and t. For this purpose, we need to calculate the topological invariant Γ_{CI} for H_{CI}. Direct diagonalization of the Hamiltonian H_{CI} leads to the energy spectrum $E_{\pm}(\mathbf{k}) = \pm|q^n| = \pm\rho^n = \pm[t^2\cos^2 k_x + \cos^2 k_y + \cos^2 k_z + (\sin k_x + \sin k_y + \sin k_z)^2]^{n/2}$. It is always gapped if $t \neq 0$ and has a twofold degeneracy for each $\mathbf{k}$. To calculate the topological index Γ_{CI}, we first flatten the bands of H_{CI} (which is a continuous transformation that does not change its topological property) by

introducing the Q matrix,

$$Q(\mathbf{k}) = 1 - 2P(\mathbf{k}), \quad P(\mathbf{k}) = \sum_f |u_f(\mathbf{k})\rangle\langle u_f(\mathbf{k})|, \tag{3.3.3}$$

where $P(\mathbf{k})$ is the projector onto the filled Bloch bands (with energy $E_-(\mathbf{k})$ and wave-vectors $|u_f(\mathbf{k})\rangle$ from the diagonalization of $\mathscr{H}_{\rm CI}$). With the chiral symmetry, the Q matrix can be brought into the block off-diagonal form $Q(\mathbf{k}) = \begin{pmatrix} 0 & b(\mathbf{k}) \\ b^\dagger(\mathbf{k}) & 0 \end{pmatrix}$ by a unitary transformation, with

$$b(\mathbf{k}) = -\begin{pmatrix} (q^n)_3 - i(q^n)_2 & -i(q^n)_0 - (q^n)_1 \\ -i(q^n)_0 + (q^n)_1 & (q^n)_3 + i(q^n)_2 \end{pmatrix} / E_+(\mathbf{k}) \tag{3.3.4}$$

for the Hamiltonian $H_{\rm CI}$. With the matrix $b(\mathbf{k})$, the topological index $\Gamma_{\rm CI}$ is defined by the following winding number [21]:

$$\Gamma_{\rm CI} = \frac{1}{24\pi^2}\int_{\rm BZ} d\mathbf{k}\, \varepsilon^{\mu\rho\lambda}{\rm Tr}[(b^{-1}\partial_\mu b)(b^{-1}\partial_\rho b)(b^{-1}\partial_\lambda b)], \tag{3.3.5}$$

where $\varepsilon^{\mu\rho\lambda}$ is the antisymmetric Levi-Civita symbol and $\partial_\mu b \equiv \partial_{k_\mu} b(\mathbf{k})$. When $n = 1$, the integral in $\Gamma_{\rm CI}$ can be calculated analytically and we find $\Gamma_{\rm CI}\,(n=1) = 2{\rm sign}(t) = \pm 2$. In general cases, due to the geometric interpretation of the map q^n, we immediately get

$$\Gamma_{\rm CI}[\mathscr{H}_{\rm CI}] = 2n{\rm sign}(t) = \pm 2n. \tag{3.3.6}$$

This result is confirmed through direct numerical calculations. We integrate Eq. (3.3.5) numerically through discretization of the Brillouin zone. The calculation results for different n are shown in Fig. 1(a), which quickly converge to the exact results in Eq. (3.3.6) as the number of integration

grids increases. As one varies n, it is evident from Eq. (3.3.6) that we can realize all the spin-singlet TSC phases in the CI class through our constructed Hamiltonian H_{CI} with the topological index Γ_{CI} taking arbitrary even integers.

3.3.2 Spin-triplet TSC (class DIII)

Spin triplet TSCs are described by the BdG Hamiltonians that have both T and C symmetries with $T^2=-1$ and $C^2=1$. It belongs to the symmetry class DIII in the periodic table. The ^{3}He superfluid B phase is a well known example in this class [19, 21], but it is not described by a simple lattice model. Tight-binding lattice Hamiltonians have been constructed for the DIII-class spin triplet TSCs with the topological index $\Gamma_{\mathrm{DIII}}=\pm 1$ [38, 78, 79]. Here, we use the quaternion method to construct tight-binding Hamiltonians for the DIII-class TSCs with arbitrary integer topological indices Γ_{DIII} in a simple cubic lattice.

To construct the Hamiltonian, we define a quaternion $q(\mathbf{k})$ with the following dependence on $\mathbf{k}$

$$q = h+\cos k_x+\cos k_y+\cos k_z+\boldsymbol{i}t\sin k_x+\boldsymbol{j}\sin k_y+\boldsymbol{k}\sin k_z. \tag{3.3.7}$$

with t,h being dimensionless parameters. We will use this form of $q(\mathbf{k})$ for all our following examples. We construct a four-band BdG Hamiltonian with the form $H_{\mathrm{DIII}}=\sum_{\mathbf{k}}\Phi^{\dagger}_{\mathbf{k}}\mathscr{H}_{\mathrm{DIII}}(\mathbf{k})\Phi_{\mathbf{k}}$, with the fermionic mode operators $\Phi_{\mathbf{k}}=(a_{\mathbf{k}\uparrow},a_{\mathbf{k}\downarrow},a^{\dagger}_{-\mathbf{k}\uparrow},a^{\dagger}_{-\mathbf{k}\downarrow})^T$ and the 4×4 Hamiltonian matrix

$$\mathscr{H}_{\mathrm{DIII}}(\mathbf{k})=\mathbf{u}\cdot\boldsymbol{\Gamma}, \tag{3.3.8}$$

where $\mathbf{u}=((q^n)_1,(q^n)_2,(q^n)_3,(q^n)_0)$, $\boldsymbol{\Gamma}=(\gamma^0\gamma^1,\gamma^0\gamma^2,\gamma^0\gamma^3,-i\gamma^0\gamma^5)$, and γ^i denote the standard Dirac matrices with the explicit expressions given in the Appendix. This Hamiltonian has spin

triplet pairing with the energy spectrum $E_{\pm}(\mathbf{k}) = \pm|\mathbf{u}(\mathbf{k})| = \pm|q(\mathbf{k})|^n$, which is fully gapped when $|h| \neq 1,3$ and $t \neq 0$.

The DIII class TSC has the chiral symmetry, so its Q matrix for the Hamiltonian can be brought into the block off-diagonal form (see Appendix A) and the topological index Γ_{DIII} is also characterized by the winding number in Eq. (3.3.5). We find

$$\Gamma_{\mathrm{DIII}}[\mathscr{H}_{\mathrm{DIII}}] = \begin{cases} -2n\mathrm{sign}(t) & |h| < 1 \\ n\mathrm{sign}(t) & 1 < |h| < 3 \\ 0 & |h| > 3 \end{cases}. \tag{3.3.9}$$

It is evident that the topological index Γ_{DIII} can take arbitrary integer values for our constructed Hamiltonian depending on the parameters n,t,h. In the particular case with $n = t = 1$, the Hamiltonian reduces to the model Hamiltonian introduced in Ref. [20, 21], which has $\Gamma_{\mathrm{DIII}} = 1$ or -2.

3.3.3 Chiral TI (class AIII)

Chiral TIs do not have time-reversal or particle-hole symmetry (thus $T = C = 0$), but they possess chiral symmetry with $S = 1$ and belongs to the symmetry class AIII in the periodic table. Tight-binding Hamiltonians have been constructed for the chiral TIs with the topological index $\Gamma_{\mathrm{AIII}} = \pm 1$ [80]. Here, we use the quaternion method to construct Hamiltonians with arbitrary integer Γ_{AIII}. We consider a three-band Hamiltonian with the following form $H_{\mathrm{AIII}} = \sum_{\mathbf{k}} \xi_{\mathbf{k}}^{\dagger} \mathscr{H}_{\mathrm{AIII}}(\mathbf{k}) \xi_{\mathbf{k}}$, where the fermionic mode operators $\xi_{\mathbf{k}} = (a_{\mathbf{k}}, b_{\mathbf{k}}, c_{\mathbf{k}})^T$ and the 3×3 Hamiltonian matrix

$$\mathscr{H}_{\mathrm{AIII}}(\mathbf{k}) = \mathbf{u} \cdot \mathscr{G}. \tag{3.3.10}$$

In $\mathscr{H}_{\rm AIII}$, $\mathbf{u}$ denotes the same quaternion coefficients as defined below Eq. (3.3.8) and $\mathscr{G}=(\lambda_4,\lambda_5,\lambda_6,\lambda_7)$ are the four Gell-Mann matrices with the explicit form given in the Appendix. The Hamiltonian $H_{\rm AIII}$ is gapped when $|h|\neq 1,3$ and $t\neq 0$ and has a perfectly flat middle band with a macroscopic number of zero-energy modes due to the chiral symmetry [80]. A topological invariant classifying this family of Hamiltonians can be defined as [80]

$$\Gamma_{\rm AIII}=-\frac{1}{12\pi^2}\int_{\rm BZ} d\mathbf{k}\,\varepsilon^{\alpha\beta\gamma\rho}\varepsilon^{\mu\nu\tau}\frac{1}{|\mathbf{u}|^4}\mathbf{u}_\alpha\partial_\mu\mathbf{u}_\beta\partial_\nu\mathbf{u}_\gamma\partial_\tau\mathbf{u}_\rho. \tag{3.3.11}$$

We have calculated this invariant and found that

$$\Gamma_{\rm AIII}[\mathscr{H}_{\rm AIII}]=n\,\mathrm{sign}(t)=\pm n,\ \ (1<|h|<3) \tag{3.3.12}$$

for our constructed $H_{\rm AIII}$. This analytic result is confirmed with direct numerical calculations as shown in Fig. 1(b). In the particular case with $n=1$, the Hamiltonian $H_{\rm AIII}$ reduces to the model Hamiltonian constructed in Ref. [80]. Through the quaternion power, we extend the model Hamiltonian and realize the chiral TIs with the topological index taking arbitrary integer values.

3.3.4 Hopf insulators (class A)

The Hamiltonians in class A do not have any symmetry (T, C, or S) except the particle number conservation. Generically, this class of Hamiltonians have no topologically nontrivial phase in 3D, but there is a peculiar exception, called the Hopf insulator, which occurs when the Hamiltonian has just two bands due to existence of the topologically nontrivial Hopf map from $\mathbb{S}^3$ to $\mathbb{S}^2$ [23, 41]. To understand why Hopf insulators exist, note that the space of all 3D band Hamiltonians with m filled and n empty bands is topologically equivalent to the Grassmannian manifold $\mathbb{G}_{m,n+m}$ and

can be classified by the homotopy group of this Grassmannian [20]. Since $\pi_3(\mathbb{G}_{m,n+m}) = 0$ for all $(m,n) \neq (1,1)$, no nontrivial topological phase exists in general. However, when $m = n = 1$, $\mathbb{G}_{1,2}$ is topologically equivalent to 2-sphere $\mathbb{S}^2$ and $\pi_3(\mathbb{G}_{m,n+m}) = \pi_3(\mathbb{S}^2) = \mathbb{Z}$. This explains why the Hopf insulators may exist in 3D. The Hopf insulators are characterized by the topological Hopf index Γ_{H}, which takes values from the integer set $\mathbb{Z}$. A model Hamiltonian has been constructed for the Hopf insulator with $\Gamma_{\mathrm{H}} = \pm 1$ in Ref. [41] based on the Hopf map [81]. This method was extended in Ref. [23] to construct Hamiltonians for general Hopf insulators with arbitrary integer Γ_{H} based on the generalized Hopf map encountered in mathematics but not in physics literature. Here, with the quaternion algebra, we use only the simple Hopf map but still can construct tight-binding Hamiltonians for the Hopf insulators with arbitrary integer Γ_{H}.

To construct the Hamiltonian, we define two complex variables $\eta = (\eta_\uparrow, \eta_\downarrow)^{\mathrm{T}}$ from the quaternion $\eta_\uparrow = (q^n)_1 + i(q^n)_2$, $\eta_\downarrow = (q^n)_3 + i(q^n)_0$, where $q(\mathbf{k})$ is defined by Eq. (3.3.7). The Hopf map is defined as $\mathbf{v} = \eta^\dagger \boldsymbol{\sigma} \eta$, which is a quadratic map from $\mathbb{S}^3 \to \mathbb{S}^2$ up to normalization. The two-band Hamiltonians can then be constructed as $H_{\mathrm{Hopf}} = \sum_{\mathbf{k}} \psi^\dagger_{\mathbf{k}} \mathscr{H}_{\mathrm{Hopf}}(\mathbf{k}) \psi_{\mathbf{k}}$ with $\psi_{\mathbf{k}} = (a_{\mathbf{k}\uparrow}, a_{\mathbf{k}\downarrow})^T$ and

$$\mathscr{H}_{\mathrm{Hopf}}(\mathbf{k}) = \mathbf{v} \cdot \boldsymbol{\sigma}. \tag{3.3.13}$$

The Hopf insulators are characterized by the topological Hopf index, define as

$$\Gamma_{\mathrm{H}}[\mathscr{H}_{\mathrm{Hopf}}] = -\int_{\mathrm{BZ}} \mathbf{F} \cdot \mathbf{A}\, d^3\mathbf{k}, \tag{3.3.14}$$

where $\mathbf{F}$ is the Berry curvature with $F_\mu \equiv \frac{1}{8\pi} \varepsilon_{\mu\nu\tau} \mathbf{v} \cdot (\partial_\nu \mathbf{v} \times \partial_\tau \mathbf{v})$ and $\mathbf{A}$ is the associated Berry connection which satisfies $\nabla \times \mathbf{A} = \mathbf{F}$ [23,41]. From this definition and our geometric interpretation of q^n, we find

$$\Gamma_{\mathrm{H}}[\mathscr{H}_{\mathrm{Hopf}}] = n\,\mathrm{sign}(t) = \pm n, \quad (1 < |h| < 3) \tag{3.3.15}$$

AZ class	Symmetry			Numerical results for different n				
	T	C	S	1	2	3	4	5
AIII	0	0	1	1.000(1)	1.999(2)	2.997(3)	3.993(4)	4.986 (5)
CI	1	-1	1	1.999(2)	3.998(4)	5.992(6)	7.984(8)	9.972(10)
DIII	-1	1	1	1.000(1)	1.999(2)	2.997(3)	3.993(4)	4.986(5)
A (HIs)	0	0	0	0.999(1)	1.994(2)	2.979(3)	3.951(4)	4.910(5)

Table 3.3: Numerical results of the corresponding topological invariants for the constructed Hamiltonians in different symmetry classes. The symmetry property of each class is also indicated. The presence of time reversal symmetry T, particle-hole symmetry C, and chiral symmetry S is denoted by ± 1, with ± 1 specifying the values of T^2 and C^2. The absence of these symmetries is denoted by 0. The parameters for the corresponding Hamiltonians are chosen as $(t,h) = (1,2)$. The number of grid points is $N_{\text{grid}} = 320$ for all the cases. The integer numbers in the parentheses are theoretical values for the corresponding topological invariants.

This analytical expression is also confirmed with direct numerical calculations. Some numerical results for the topological indices are listed in Table (3.3) for different classes of TIs and TSCs, which agree very well with our analytical expressions.

It is noteworthy to point out that although the geometric picture is intuitive, it is not a mathematically rigorous proof. We therefore have done substantial numerical calculations to support our conclusion and parts of our results are shown in Table (3.3). All results are in line with the geometric argument and the topological invariants indeed have values proportional to the power n of the quaternions. Another subtlety to note is that we did not define the same quaternion for all four examples. This has its root in the parity restriction for each component of the quaternion. In the construction of $\mathscr{H}_{\text{CI}}^{(n)}(\mathbf{k})$, the symmetries require three components of the quaternion q to have even parity under the exchange $\mathbf{k} \to -\mathbf{k}$ and the remaining component odd parity. However, for $\mathscr{H}_{\text{DIII}}^{(n)}(\mathbf{k})$, three components should be odd and the other even. As a result, different quaternions are chosen for these two classes. We wish to underline the important fact that q^n preserves the parity property of q defined above. This crucial property of quaternion algebra enables us to write down a unified expression for Hamiltonians of each symmetry class with arbitrary integer topological

index.

3.4 Discussion and conclusion

Before ending this chapter, we briefly remark that the quaternion tool proposed here can be extended straightforwardly to the 1D and 2D cases although our focus in this chapter is on the 3D topological phases. We can set one (two) of the quaternion components to zero for the 2D (1D) case and observe that the map $q \longrightarrow q^n$ always preserves the subspace of $\mathbb{H}$ spanned by $\{1, \boldsymbol{i}, \boldsymbol{j}\}$) ($\{1, \boldsymbol{i}\}$). With the power mapping q^n which preserve the symmetry of the Hamiltonian, starting from one particular example of topological Hamiltonians with the topological index $\Gamma = \pm 1$, we can always construct a family of Hamiltonians which realize all the topological phases with arbitrary integer Γ. Another interesting topic is to study the application of our quaternion toolkit in interacting systems and how interaction will affect our constructed Hamiltonians. In the small interaction limit, our constructions should not be affected because of the finite energy gap in the constructed Hamiltonians.

In summary, we have proposed a powerful tool based on the quaternion algebra to systematically construct tight-binding Hamiltonians for all the topological phases in the periodic table that are characterized by arbitrary integer topological indices. The constructed Hamiltonians make the basis for further studies of properties of these topological phases and phase transitions and provide an important step for future experimental realization.

CHAPTER IV

Hopf insulators

4.1 Introduction

Three-dimensional (3D) topological insulators in general need to be protected by certain kinds of symmetries other than the presumed $U(1)$ charge conservation. A peculiar exception is the Hopf insulators which are 3D topological insulators characterized by an integer Hopf index. To demonstrate the existence and physical relevance of the Hopf insulators, in Sec. 4.2, we construct a class of tight-binding model Hamiltonians which realize all kinds of Hopf insulators with arbitrary integer Hopf index. These Hopf insulator phases have topologically protected surface states and we numerically demonstrate the robustness of these topologically protected states under general random perturbations without any symmetry other than the $U(1)$ charge conservation that is implicit in all kinds of topological insulators.

Moreover, the 4D topological phases in symmetry class A generally have a $\mathbb{Z}$ classification according to the periodic table for topological insulators and supercondutors. However, in Sec. 4.3, we show that there exists also an accidental $\mathbb{Z}_2$ classification when the Hamiltonian has only two effec-

tive bands. We construct explicitly a model Hamiltonian for the nontrivial phase and numerically show that the edge states are robust to random perturbations.

4.2 Hopf insulators with arbitrary Z index

Topological phases of matter may be divided into two classes: the intrinsic ones and the symmetry protected ones [17]. Symmetry protected topological (SPT) phases are gapped quantum phases that are protected by symmetries of the Hamiltonian and cannot be smoothly connected to the trivial phases under perturbations that respect the same kind of symmetries. Intrinsic topological (IT) phases, on the other hand, do not require symmetry protection and are topologically stable under arbitrary perturbations. Unlike SPT phases, IT phases may have exotic excitations bearing fractional or even non-abelian statistics in the bulk [57]. Fractional [5, 51] quantum Hall states and spin liquids [52–56] belong to these IT phases. Remarkable examples of the SPT phases include the well known 2D and 3D topological insulators and superconductors protected by time reversal symmetry [7, 8, 11, 16, 36, 40], and the Haldane phase of the spin-1 chain protected by the $SO(3)$ spin rotational symmetry [46,47]. For interacting bosonic systems with on-site symmetry G, distinct SPT phases can be systematically classified by group cohomology of G [17], while for free fermions, the SPT phases can be systematically described by K-theory or homotopy group theory [48], which leads to the well known periodic table for topological insulators and superconductors [19, 20].

Most 3D topological insulators have to be protected by some other symmetries [19, 20], such as time reversal, particle hole or chrial symmetry, and the $U(1)$ charge conservation symmetry [82]. A peculiar exception occurs when the Hamiltonian has just two effective bands. In this case, interesting topological phases, the so-called Hopf insulators [41], may exist. These Hopf insulator

phases have no symmetry other than the prerequisite $U(1)$ charge conservation. To elucidate why this happens, let us consider a generic band Hamiltonian in 3D with m filled bands and n empty bands. Without symmetry constraint, the space of such Hamiltonians is topologically equivalent to the Grassmannian manifold $\mathbb{G}_{m,m+n}$ and can be classified by the homotopy group of this Grassmannian [20]. Since the homotopy group $\pi_3(\mathbb{G}_{m,m+n}) = \{0\}$ for all $(m,n) \neq (1,1)$, there exists no nontrivial topological phase in general. However, when $m = n = 1$, $\mathbb{G}_{1,2}$ is topologically equivalent to $\mathbb{S}^2$ and the well-known Hopf map in mathematics shows that $\pi_3(\mathbb{G}_{1,2}) = \pi_3(\mathbb{S}^2) = \mathbb{Z}$ [48]. This explains why the Hopf insulators may exist only for Hamiltonians with two effective bands. The classification theory shows that the peculiar Hopf insulators may exist in 3D, but it does not tell us which Hamiltonian can realize such phases. It is even a valid question whether these phases can appear at all in physically relevant Hamiltonians. Moore, Ran, and Wen made a significant advance in this direction by constructing a Hamiltonian that realizes a special Hopf insulator with the Hopf index $\chi = 1$ [41].

In this section, we construct a class of tight-binding Hamiltonians that realize arbitrary Hopf insulator phases with any integer Hopf index χ. The Hamiltonians depend on two parameters and contain spin-dependent and spin-flip hopping terms. We map out the complete phase diagram and show that all the Hopf insulators can be realized with this type of Hamiltonians. We numerically calculate the surface states for these Hamiltonians and show that they have zero energy modes that are topologically protected and robust to arbitrary random perturbations with no other than the $U(1)$ symmetry constraint.

To begin with, let us notice that any two-band Hamiltonian in 3D with one filled band can be expanded in the momentum space with three Pauli matrices $\boldsymbol{\sigma} = (\sigma^x, \sigma^y, \sigma^z)$ as

$$\mathscr{H}(\mathbf{k}) = \mathbf{u}(\mathbf{k}) \cdot \boldsymbol{\sigma}, \tag{4.2.1}$$

where we have ignored the trivial energy-shifting term $u_0(\mathbf{k})\mathbf{I}_2$ with $\mathbf{I}_2$ being the 2×2 identity matrix. By diagonalizing $\mathscr{H}(\mathbf{k})$, we have the energy dispersion $E(\mathbf{k}) = \pm|\mathbf{u}(\mathbf{k})|$, where $|\mathbf{u}(\mathbf{k})| = \sqrt{u_x^2(\mathbf{k}) + u_y^2(\mathbf{k}) + u_z^2(\mathbf{k})}$. The Hamiltonian is gapped if $|\mathbf{u}(\mathbf{k})| > 0$ for all $\mathbf{k}$. For the convenience of discussion of topological properties, we denote $\mathbf{u}(\mathbf{k}) = |\mathbf{u}(\mathbf{k})|(x(\mathbf{k}), y(\mathbf{k}), z(\mathbf{k}))$ with $x^2(\mathbf{k}) + y^2(\mathbf{k}) + z^2(\mathbf{k}) = 1$. Topologically, the Hamiltonian (1) can be considered as a map from the momentum space $\mathbf{k} = (k_x, k_y, k_z)$ characterized by the Brillouin zone $\mathbb{T}^3$ ($\mathbb{T}$ denotes a circle and $\mathbb{T}^3$ is the 3D torus) to the parameter space $\mathbf{u}(\mathbf{k}) \propto (x(\mathbf{k}), y(\mathbf{k}), z(\mathbf{k}))$ characterized by the Grassmannian $\mathbb{G}_{1,2} = \mathbb{S}^2$. Topologically distinct band insulators correspond to different classes of maps from $\mathbb{T}^3 \to \mathbb{S}^2$.

The classification of all the maps from $\mathbb{T}^3 \to \mathbb{S}^2$ is related to the *torus homotopy group* $\tau_3(\mathbb{S}^2)$ [83]. To construct non-trivial maps form $\mathbb{T}^3 \to \mathbb{S}^2$, we take two steps, first from $\mathbb{S}^3 \to \mathbb{S}^2$ and then from $\mathbb{T}^3 \to \mathbb{S}^3$. We make use of the following generalized Hopf map $f : \mathbb{S}^3 \to \mathbb{S}^2$ known in the mathematical literature [81]

$$x + iy = 2\lambda \eta_\uparrow^p \bar{\eta}_\downarrow^q,\ z = \lambda(|\eta_\uparrow|^{2p} - |\eta_\downarrow|^{2q}), \tag{4.2.2}$$

where p, q are integers prime to each other and $\eta_\uparrow$, $\eta_\downarrow$ are complex coordinates for $\mathbb{R}^4$ satisfying $|\eta_\uparrow|^2 + |\eta_\downarrow|^2 = 1$ with the normalization $\lambda = 1/(|\eta_\uparrow|^{2p} + |\eta_\downarrow|^{2q})$. Equation (2) maps the coordinates $\big(\mathrm{Re}[\eta_\uparrow], \mathrm{Im}[\eta_\uparrow], \mathrm{Re}[\eta_\downarrow], \mathrm{Im}[\eta_\downarrow]\big)$ of $\mathbb{S}^3$ to the coordinates (x, y, z) of $\mathbb{S}^2$ with $x^2 + y^2 + z^2 = 1$. The Hopf index for the map f is known to be $\pm pq$ with the sign determined by the orientation of $\mathbb{S}^3$ [81]. We then construct another map $g : \mathbb{T}^3 \to \mathbb{S}^3$ (up to a normalization), defined by the

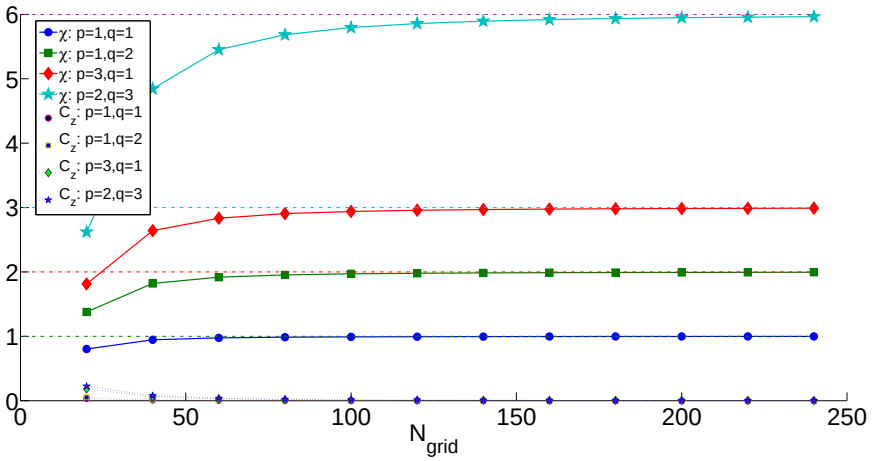

Figure 4.2.1: (Color online) Plot of the Hopf index and the Chern number in z-direction for different (p,q). The Hopf index and the Chern number converge rapidly as the number of grids increases in discretization. The parameters t and h are chosen as $(t,h) = (1, 1.5)$.

following equation

$$\begin{aligned} \eta_{\uparrow}(\mathbf{k}) &= \sin k_x + it \sin k_y, \\ \eta_{\downarrow}(\mathbf{k}) &= \sin k_z + i(\cos k_x + \cos k_y + \cos k_z + h), \end{aligned} \tag{4.2.3}$$

where t and h are constant parameters. The composite map $f \circ g$ from $\mathbb{T}^3 \to \mathbb{S}^2$ then defines the parameters $\mathbf{u}(\mathbf{k}) \propto (x(\mathbf{k}), y(\mathbf{k}), z(\mathbf{k}))$ in the Hamiltonian as a function of the momentum $\mathbf{k}$. From Eqs. (7.2.1) and (4.2.3), we have $\mathbf{u}(\mathbf{k}) = (\mathrm{Re}[2\eta_{\uparrow}^{p}\bar{\eta}_{\downarrow}^{q}], \mathrm{Im}[2\eta_{\uparrow}^{p}\bar{\eta}_{\downarrow}^{q}], [|\eta_{\uparrow}|^{2p} - |\eta_{\downarrow}|^{2q}])$, with $|\mathbf{u}(\mathbf{k})| = \frac{1}{\lambda(\mathbf{k})}$. The Hamiltonian $\mathscr{H}(\mathbf{k}) = \mathbf{u}(\mathbf{k}) \cdot \boldsymbol{\sigma}$ is $(p+q)$th order polynomials of $\sin(\mathbf{k})$ and $\cos(\mathbf{k})$, which corresponds to a tight-binding model when expressed in the real space. The Hamiltonian contains spin-orbital coupling with spin-dependent hopping terms. When we choose $p = q = 1$ and $(t,h) = (1, -3/2)$, the Hamiltonian (4.2.1) reduces to the special case studied in Ref. [41].

When the Hamiltonian is gapped with $|\mathbf{u}(\mathbf{k})| > 0$, one can define a direction on the unit sphere $\hat{\mathbf{u}}(\mathbf{k}) = (u_x(\mathbf{k}), u_y(\mathbf{k}), u_z(\mathbf{k}))/|\mathbf{u}(\mathbf{k})| = (x(\mathbf{k}), y(\mathbf{k}), z(\mathbf{k}))$. From $\hat{\mathbf{u}}(\mathbf{k})$, we define the Berry curva-

ture $F_\mu = \frac{1}{8\pi}\varepsilon_{\mu\nu\tau}\hat{\mathbf{u}}\cdot(\partial_\nu\hat{\mathbf{u}}\times\partial_\tau\hat{\mathbf{u}})$, where $\varepsilon_{\mu\nu\tau}$ is the Levi-Civita symbol and a summation over the same indices is implied. A 3D torus $\mathbb{T}^3$ has three orthogonal cross sections perpendicular to the axis x,y,z, respectively. For each cross section of space $\mathbb{T}^2$, one can introduce a Chern number $C_\mu = \int_{-\pi}^{\pi}\int_{-\pi}^{\pi} dk_\rho dk_\lambda F_\mu$, where $\mu = x,y,z$ and ρ,λ denote directions orthogonal to μ. To classify the maps from $\mathbb{T}^3 \to \mathbb{S}^2$ represented by $\hat{\mathbf{u}}(\mathbf{k})$, a topological index, the so-called Hopf index, was introduced by Pontryagin [84], who showed that the Hopf index takes values in the finite group $\mathbb{Z}_{2\cdot\mathrm{GCD}(C_x,C_y,C_z)}$ when the Chern numbers C_μ are nonzero [84], where GCD denotes the greatest common divisor. If the Chern numbers $C_\mu = 0$ in all three directions, the Hopf index takes all integer values $\mathbb{Z}$ and has a simple integral expression [81, 85]

$$\chi(\hat{\mathbf{u}}) = -\int_{\mathrm{BZ}} \mathbf{F}\cdot\mathbf{A}\, d\mathbf{k}, \tag{4.2.4}$$

where $\mathbf{A}$ is the Berry connection (or called the gauge field) which satisfies $\nabla\times\mathbf{A} = \mathbf{F}$. The Hopf index $\chi(\hat{\mathbf{u}})$ is gauge invariant although its expression depends on $\mathbf{A}$. As we will analytically prove in the Appendix B, the Chern numbers $C_\mu = 0$ for the map $\hat{\mathbf{u}}(\mathbf{k})$ defined above in this chapter in the gapped phase, so we can use the integral expression of Eq. (4) to calculate the Hopf index $\chi(\hat{\mathbf{u}})$. The index $\chi(\hat{\mathbf{u}})$ can be calculated numerically through discretization of the torus $\mathbb{T}^3$ [41]. Using this method, we have numerically computed the Hopf index $\chi(\hat{\mathbf{u}})$ for the Hamiltonian $\mathscr{H}(\mathbf{k})$ with various p and q, and the results are shown in Fig. 4.2.1. As the grid number increases in discretization, we see that the Chern numbers quickly drop to zero and the Hopf index approaches the integer values $\pm pq$ or $\pm 2pq$ depending on the parameters t,h. Based on the numerical results of $\chi(\hat{\mathbf{u}})$, we construct the phase diagrams of the Hamiltonian (1) for various p, q in Fig. 4.2.2. The phase boundaries are determined from the gapless condition. The phase diagrams exhibit regular patterns: they are mirror symmetric with respect to the axis $h = 0$ and anti-symmetric with respect

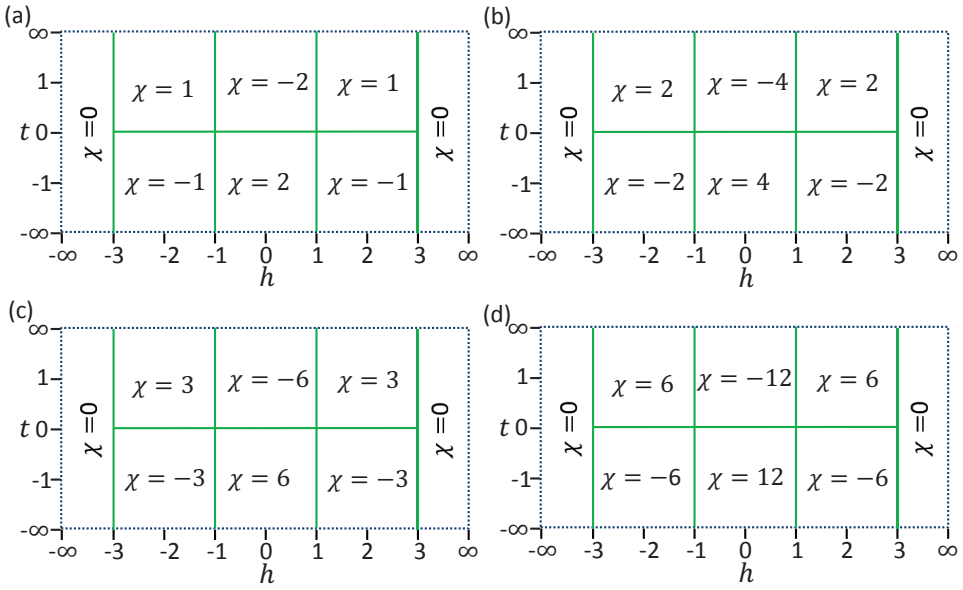

Figure 4.2.2: (Color online) Phase diagrams of the Hamiltonian for different (p,q). The values of (p,q) in (a), (b), (c), and (d) are chosen to be $(1,1)$, $(1,2)$, $(3,1)$, and $(2,3)$, respectively.

to the axis $t = 0$. When $|h| > 3$, we only have a topologically trivial phase with $\chi(\hat{\mathbf{u}}) = 0$. From the result, we see that $\chi(\hat{\mathbf{u}})$ has an analytic expression with $\chi(\hat{\mathbf{u}}) = \pm pq$ when $1 < |h| < 3$ and $\chi(\hat{\mathbf{u}}) = \pm 2pq$ when $|h| < 1$.

To understand this result, we note that $\hat{\mathbf{u}}(\mathbf{k})$ is a composition of two maps $\hat{\mathbf{u}}(\mathbf{k}) = f \circ g(\mathbf{k})$. The generalized Hopf maps f from $\mathbb{S}^3 \to \mathbb{S}^2$ has a known Hopf index $\pm pq$ [81]. The maps g from $\mathbb{T}^3 \to \mathbb{S}^3$ can be classified by the torus homotopy group $\tau_3(\mathbb{S}^3)$ and a topological invariant has been introduced to describe this classification [80], which has an integral expression

$$\Gamma(g) = \frac{1}{12\pi^2}\int_{\mathrm{BZ}} d\mathbf{k}\varepsilon_{\alpha\beta\gamma\rho}\varepsilon_{\mu\nu\tau}\frac{1}{|\boldsymbol{\eta}|^4}\eta_\alpha\partial_\mu\eta_\beta\partial_\nu\eta_\gamma\partial_\tau\eta_\rho,$$

where $\boldsymbol{\eta} = (\mathrm{Re}[\eta_\uparrow], \mathrm{Im}[\eta_\uparrow], \mathrm{Re}[\eta_\downarrow], \mathrm{Im}[\eta_\downarrow])$. Direct calculation of $\Gamma(g)$ leads to the following result:

$$\Gamma(g) = \begin{cases} 0, & |h| > 3 \\ 1, & 1 < |h| < 3 \text{ and } t > 0 \\ -2, & |h| < 1 \text{ and } t > 0. \end{cases}$$

Consequently, we have $\chi(\hat{\mathbf{u}}) = \Gamma(g)\chi(f) = \pm pq\Gamma(g)$, which is exactly the result shown in the phase diagrams in Fig. 4.2.2. A geometric interpretation is that $\Gamma(g)$ counts how many times $\mathbb{T}^3$ wraps around $\mathbb{S}^3$ under the map g, and $\chi(f)$ describes how many times $\mathbb{S}^3$ wraps around $\mathbb{S}^2$ under the generalized Hopf map f. Their composition gives the Hopf index $\chi(\hat{\mathbf{u}})$. A sign flip of t changes the orientation of the sphere $\mathbb{S}^3$, which induces a sign flip in $\chi(\hat{\mathbf{u}})$ and produces the anti-symmetric phase diagram with respect to the axis $t = 0$. As (p,q) are arbitrary coprime integers, $\chi(\hat{\mathbf{u}})$ apparently can take any integer value depending on the values of p,q and t,h. As a consequence, the Hamiltonian $\mathscr{H}(\mathbf{k})$ constructed in this chapter can realize arbitrary Hopf insulator phases.

Similar to the cases of quantum Hall states [86] and topological insulators, the nontrivial topological invariant of the Hopf insulators guarantees the existence of gapless surface states at the boundaries. To study this property, we numerically computed the midgap surface state energy and wave-function induced by abrupt boundaries in the (001) direction (see Appendix B). The results are summarized in Fig. 4.2.3. From the figure, surface states and localized zero-energy modes are prominent. These surface states are topologically protected and robust under arbitrary random perturbations that only respect the prerequisite $U(1)$ symmetry. This can be clearly seen from Fig. 4.2.3: while the wave functions of the bulk states change dramatically under random perturbations, the wave functions of the surface states remain stable and are always sharply peaked at the

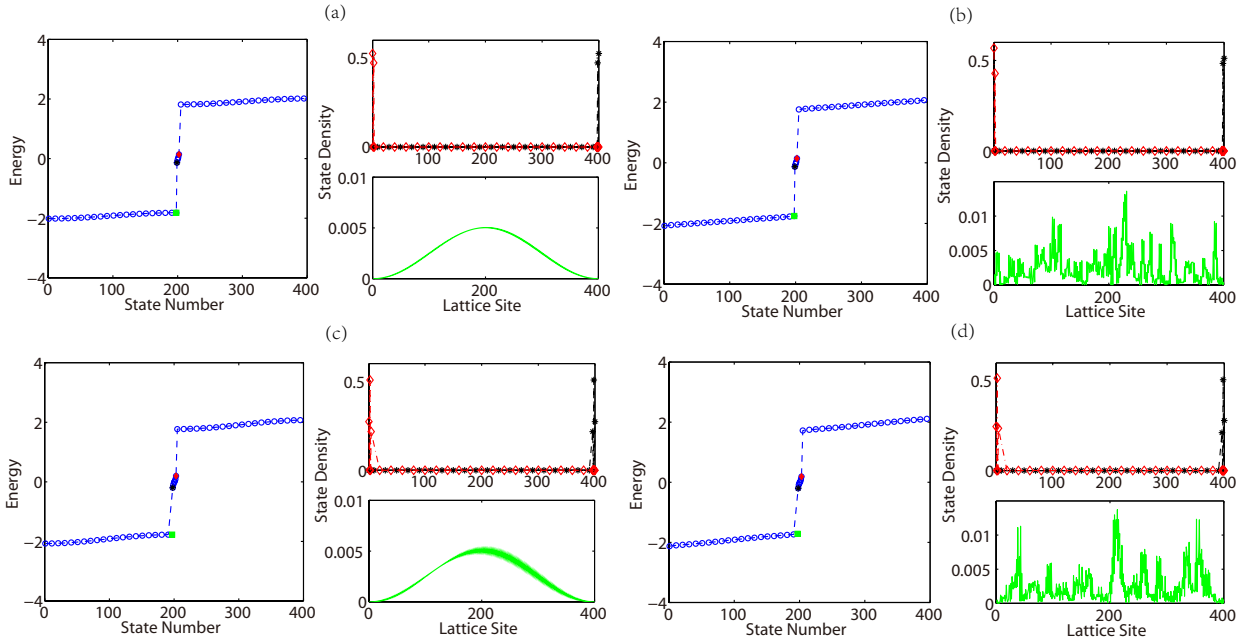

Figure 4.2.3: (Color online) Surface states and zero-energy modes in the (001) direction for a 200-site-thick slab. The parameters t and h are chosen as $(t,h)=(1,1.5)$ for all the figures. We have $(p,q)=(1,2)$ for (a,b) and $(p,q)=(1,3)$ for (c,d). In Fig. (b,d), we add random perturbations to the Hamiltonian, but otherwise keep the same parameters as (a,c). The left diagrams in (a,b,c,d) plot the energy spectrum of all 400 states at a fixed $(k_x,k_y)=(0.72,0.72)$ for easy visualization. The points inside the gap represent the energies of the surface states. There are four (six) surface states in (a,b) ((c,d)), respectively. The right diagrams in in (a,b,c,d) show the wave functions of a surface state (upper one) and a bulk state (lower one).

boundary. This verifies that the Hopf insulators are indeed 3D topological phases. Besides the results shown in Fig. 4.2.3, we have calculated the surface states for a number of different choices of parameters (p,q) and (t,h), and the results consistently demonstrate that the surface states and zero energy modes are always present and robust even to substantial perturbations unless the bulk gap closes. Moreover, we roughly have more surfaces states when the absolute value of the Hopf index becomes larger. However, this is not always true. A direct correspondence between the Hopf index and the total winding number of surface states may exist and should be investigated [87]. We left this topic for future works.

An important and intriguing question is how to realize these Hopf insulators in experiments. Laser assisted hopping of ultracold atoms in an optical lattice offers a powerful tool to engineer various kinds of spin-dependent tunneling terms [72, 88, 89], and thus provides a good candidate for their realizations although the details still need to be worked out. Dipole interaction between polar molecules in optical lattices also offers possibilities to realize effective spin-dependent hopping [90–92]. As argued in Ref. [41], frustrated magnetic compounds such as $X_2Mo_2O_7$ with X being a rare earth ion are other potential candidates. In addition, Hopf insulators may be realized in 3D quantum walks [93–96], where various hopping terms are implemented by varying the walking distance and direction in each spin-dependent translation and the robust surface states can be observed with split-step schemes [96].

In conclusion, we have introduced a class of tight-binding Hamiltonians that realize arbitrary Hopf insulators. The topologically protected surface states and zero-energy modes in these exotic phases are robust to random perturbations that only respect the $U(1)$ charge conservation symmetry. They are 3D topological phases and sit outside of the periodic table [19, 20] for topological insulators and superconductors.

4.3 $\mathbb{Z}_2$ insulators in four dimensions

For symmetry class A in 4D, we generally have a $\mathbb{Z}$ classification. In this section, we show, however, that there exists also an accidental $\mathbb{Z}_2$ classification when the Hamiltonian has only two effective bands. Mathematically, since $\pi_4(\mathbb{S}^2) = \mathbb{Z}_2$, there should exists a topologically nontrivial map F from $\mathbb{S}^4 \to \mathbb{S}^2$. To construct such a map, we use the suspension technique in algebraic topology [97] to first obtain a nontrivial map $\mathrm{S}[f] : \mathbb{S}^4 \to \mathbb{S}^3$ and then compose $\mathrm{S}[f]$ and h to obtain f. Graphically, we have

$$\mathbb{S}^4 \xrightarrow{\mathrm{s}[f]} \mathbb{S}^3 \xrightarrow{f} \mathbb{S}^2,$$

where $\mathrm{S}[f]$ is the suspension of the Hopf map f defined as

$$\mathrm{S}[f](x_1,x_2,x_3,x_4,x_5) = (f(x_1,x_2,x_3,x_4),x_5).$$

The composed map $F = f \circ \mathrm{S}[f]$ is a map from $\mathbb{S}^4 \to \mathbb{S}^2$ up to normalization and is nontrivial by its construction nature. With F in hand, we are now ready to construct a toy model Hamiltonian for a 4D topological insulaotr. Let $X(\mathbf{k}) = (x_1,x_2,x_3,x_4,x_5)(\mathbf{k}) = (\sin k_x, \sin k_y, \sin k_z, \sin k_w, m + \cos k_x + \cos k_y + \cos k_z + \cos k_w)$, the 4D Hamiltonian reads $H_{4D} = \sum_{\mathbf{k}} \Psi^\dagger_{\mathbf{k}} \mathscr{H}_{4D}(\mathbf{k}) \Psi_{\mathbf{k}}$ with $\Psi_{\mathbf{k}} = (a_\uparrow, a_\downarrow)^T$ and

$$\mathscr{H}_{4D}(\mathbf{k}) \quad = \quad F_1\sigma^x + F_2\sigma^y + F_3\sigma^z, \tag{4.3.1}$$

where F_i $(i = 1,2,3)$ is the i-th component of the map F and $(\sigma^x, \sigma^y, \sigma^z)$ are the three Pauli matrices. Writting down F_i explicitly, we have

$$
\begin{aligned}
F_1 &= 4[(m+\cos k_x+\cos k_y+\cos k_z+\cos k_w)(\sin k_x \sin k_w-\sin k_y \sin k_z) \\
&+ (\sin k_y \sin k_w+\sin k_x \sin k_z)(\sin^2 k_x+\sin^2 k_y-\sin^2 k_w-\sin^2 k_z)], \\
F_2 &= 4[(m+\cos k_x+\cos k_y+\cos k_z+\cos k_w)(\sin k_y \sin k_w+\sin k_x \sin k_z) \\
&- (\sin k_x \sin k_w-\sin k_y \sin k_z)(\sin^2 k_x+\sin^2 k_y-\sin^2 k_w-\sin^2 k_z)], \\
F_3 &= 4(\sin k_y \sin k_w+\sin k_x \sin k_z)^2+4(\sin k_x \sin k_w-\sin k_y \sin k_z)^2 \\
&- (m+\cos k_x+\cos k_y+\cos k_z+\cos k_w)^2-((\sin^2 k_x+\sin^2 k_y-\sin^2 k_w-\sin^2 k_z))^2.
\end{aligned}
$$

From Eq. (4.3.1), we obtain the energy spectrum $E_{\pm}(\mathbf{k}) = \pm\sqrt{F_1^2(\mathbf{k})+F_2^2(\mathbf{k})+F_3^2(\mathbf{k})}$, which indicates that the Hamiltonian is fully gapped when $m \neq 0, \pm 2, \pm 4$. In real space, this tight-binding Hamiltonian contains local (up to the fourth neighboring sites) spin-flipping terms determined by $F_1(\mathbf{k})+iF_2(\mathbf{k})$ and hopping terms determined by $F_3(\mathbf{k})$.

To study the topological properties of 4D $\mathbb{Z}_2$ TIs, we need to define a topological invariant. For a 4D time-reversal-invariant topological insulator classified by integer $\mathbb{Z}$ [45, 98], the natural topological invariant is the second Chern number defined as:

$$
\mathrm{Ch}_2 = \frac{1}{32\pi^2}\int_{\mathrm{BZ}} d^4\mathbf{k}\varepsilon^{ijkl}\mathrm{tr}[\mathscr{F}_{ij}\mathscr{F}_{kl}],
$$

where the Berry curvature $\mathscr{F}_{ij}^{\mu\nu} = \partial_i \mathscr{A}_j^{\mu\nu} - \partial_j \mathscr{A}_i^{\mu\nu} + i[\mathscr{A}_i, \mathscr{A}_j]^{\mu\nu}$, and $\mathscr{A}_i^{\mu\nu}(\mathbf{k}) = -i\langle \mu, \mathbf{k}|\partial_i|\nu, \mathbf{k}\rangle$. One might expect Ch_2 mod 2 to be a suitable topological invariant for our 4D TIs. However, it is not. By discretizing the integral over the Brillouin zone (BZ), we numerically calculated Ch_2 for m in different regions and found that it vanishes for all the cases. We may calculate another topological invariant, called Kervaire invarian, but the details should be filled in the future. For our

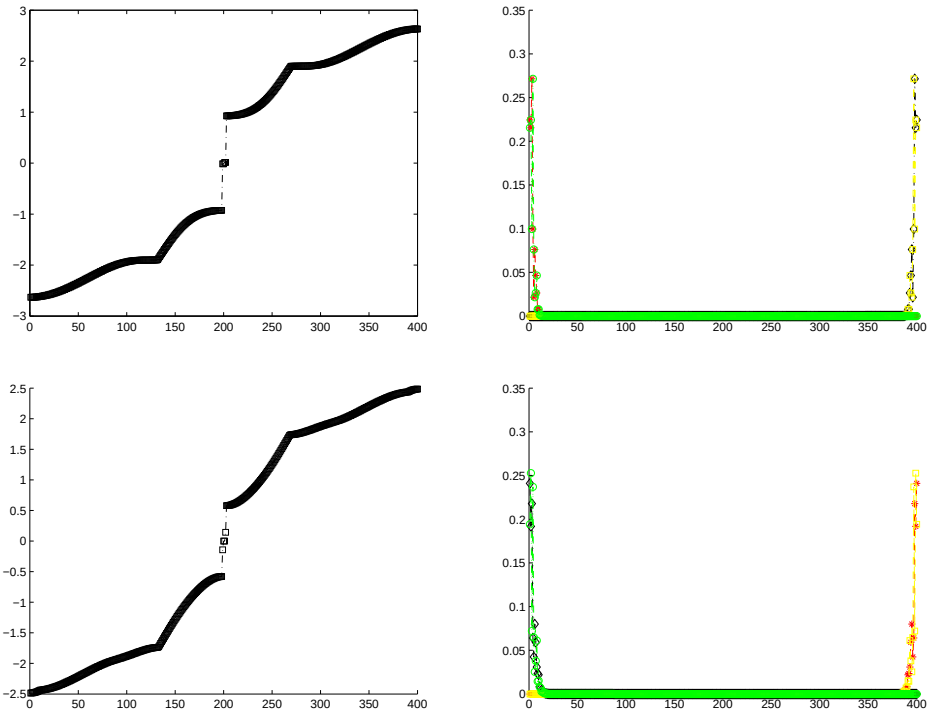

Figure 4.3.1: Energy spectrum and edge states for the four dimensional Hopf insulators in the (0001)-direction for a 40-site-thick slab. The parameter m is chosen as $m = 1$.

specific $\mathscr{H}(\mathbf{k})$, we know that it F is nontrivial, which follows from the property of suspension. Thus, we only need to check that the map $X(\mathbf{k})$ from $\mathbb{T}^4$ to $\mathbb{S}^4$ is nontrivial. Maps from $\mathbb{T}^4$ to $\mathbb{S}^4$ can be characterized by the winding number

$$\chi = \frac{1}{21\pi^3}\int_{\mathrm{BZ}} d^4\mathbf{k}\varepsilon^{ijklm}\varepsilon^{\mu\nu\tau\lambda}\frac{1}{|X|^5}X_i\partial_\mu X_j\partial_\nu X_k\partial_\tau X_l\partial_\lambda X_m.$$

For the specific map $X(\mathbf{k})$ defined above, we have

$$\chi[X(\mathbf{k})] = \begin{cases} 1 & m\in(-4,-2) \\ -3 & m\in(-2,-0) \\ 3 & m\in(0,2) \\ -1 & m\in(2,4) \\ 0 & \text{otherwise} \end{cases}$$

Thus, the Hamiltonian is in a topologically nontrivial phase unless $|m|>4$. In Fig. (4.3.1), we have plotted the edge states for 4D TIs. It is evident that these edge states are localized at the surfaces. We also added random perturbations into the Hamiltonian and find that these surface states are quite robust.

We can also do dimensional reduction to obtain 3D topological insulators. Let $k_w = 0$, we obtain a three dimensional Hamiltonian:

$$\mathscr{H}_{3D} = d_1\sigma^x + d_2\sigma^y + d_3\sigma^z,$$

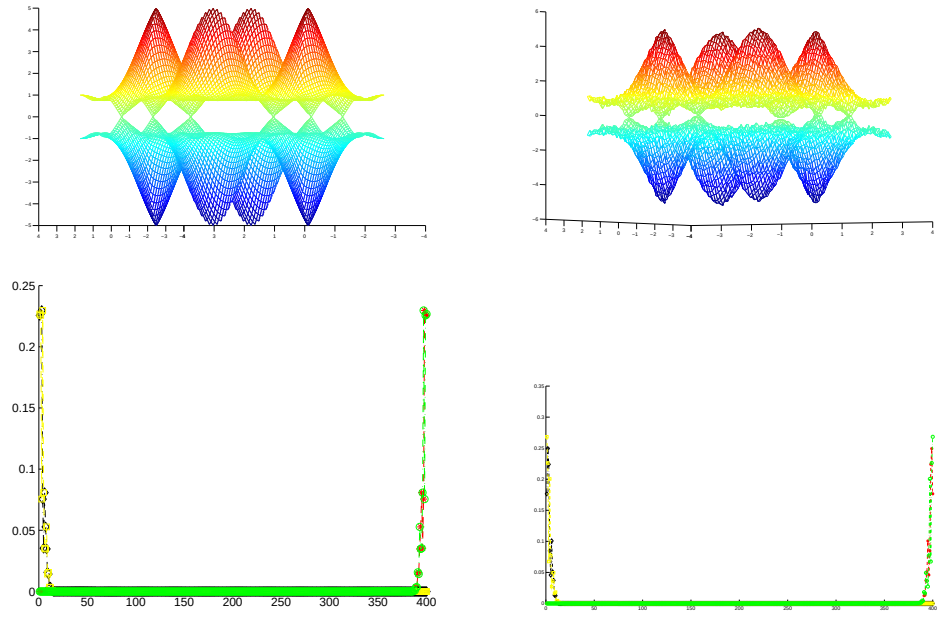

Figure 4.3.2: Surface states for reduced topological insulators in 3D. We use periodic boundary conditions in the x- and y- direction, but open boundary condition in the z-direction. The lattice size in z-direction is 200. The parameter m is chosen as $m = 1$

where $d = (d_1, d_2, d_3) = F(k_x, k_y, k_z, k_w = 0)$. More explicitly,

$$\begin{aligned} d_1 &= 4\sin k_z[\sin^3 k_x - (m_1 + \cos k_x + \cos k_y + \cos k_z)\sin k_y + \sin k_x(\sin^2 k_y - \sin^2 k_z)], \\ d_2 &= 4\sin k_z[(m_1 + \cos k_x + \cos k_y + \cos k_z)\sin k_x + \sin k_y(\sin^2 k_x + \sin^2 k_y - \sin^2 k_z)], \\ d_3 &= -(m_1 + \cos k_x + \cos k_y + \cos k_z)^2 + 4\sin^2 k_x \sin^2 k_z + 4\sin^2 k_y \sin^2 k_z \\ &- (\sin^2 k_x + \sin^2 k_y - \sin^2 k_z)^2. \end{aligned}$$

Numerically, we find that the Hopf index $\chi(\mathscr{H}_{3D}) = 0$ for all m. In fact, this can also be analytically proved. In Fig. (4.3.2), we also plot the edge states in the z-direction.

Using the same argument, for two-band Hamiltonians one may also obtain nontrivial classifications in higher dimensions that are outside the table and construct toy models for these interesting phases. For instance, in 5D and 6D, since $\pi_5(\mathbb{S}^2) = \mathbb{Z}_2$ and $\pi_6(\mathbb{S}^2) = \mathbb{Z}_{12}$, we have $\mathbb{Z}_2$ and $\mathbb{Z}_{12}$ classification, respectively. The classifications depend on the sphere homotopy group, which is an important open question in algebraic topology.

CHAPTER V

Simulations of topological phases with ultracold atoms

5.1 Introduction

The exploration of topological phases of matter has become a major theme at the frontiers of the condensed matter physics since the discovery of topological insulators [7–9]. The TIs are band insulators with peculiar topological properties that are protected by the time reversal symmetry. A recent remarkable theoretical advance is the finding that there are various other kinds of topological phases of free fermions apart from the conventional TIs, which can be classified by a periodic table according to the system symmetry and dimensionality [19, 20]. An important question then is whether the new topological phases predicted by the periodic table can be physically realized. Several model Hamiltonians have been proposed to have the predicted topological phases as their ground states [21,23,41,73,80]. However, these model Hamiltonians typically require complicated spin-orbital couplings that are hard to be realized in real materials. Implementations of these model Hamiltonians still remain very challenging for experiments.

In this chapter, we propose an experimental scheme to realize a three-dimensional (3D) chiral TI

with cold fermionic atoms in an optical lattice. The chiral TI is protected by the chiral symmetry, also known as the sub-lattice symmetry [21, 99, 100]. Unlike the conventional TIs protected by the time reversal symmetry, which is characterized by a $\mathbb{Z}_2$ topological invariant, the chiral TI is characterized by a topological invariant taking arbitrary integer values (thus belongs to the $\mathbb{Z}$ class) [19, 20]. By controlling the spin-orbital coupling of cold fermionic atoms in a tilted optical lattice based on the Raman assisted hopping [101–103], we realize a tight-binding model Hamiltonian first proposed in Ref. [80], which supports a chiral TI with a zero-energy flat band. This implementation provides the ideal experimental platform to study the effect of interactions for topological insulators. In a flat band, the kinetic energy is suppressed, and the atomic interaction, which can be tuned by the Feshbach resonance technique [104], will lead to novel non-perturbative effect. In cold atom experiment, flat bands have been studied in a 2D frustrated Kagome lattice [105]. Inspired by the discovery of the fractional quantum Hall effect in a topologically nontrivial flat-band Landau level, one expects that the atomic interaction in a flat-band TI may lead to exciting new physics [106–108]. To probe the properties of the chiral TI in our proposed realization, we show that topological phase transition and the characteristic surface states of the TIs, the Dirac cones, can both be detected by mapping out the Fermi surface structure through the time-of-flight imaging [109–111] or the Bragg spectroscopy of ultracold atoms [112]. Furthermore, we show that an important property of this model, the flat band, can be verified by measurement of the atomic density profile under a weak global harmonic trap that is always present in real experiments [113, 114].

5.2 Simulation of chiral topological insulators

5.2.1 Model Hamiltonian

We consider realization of the following tight-binding model Hamiltonian in the momentum space [80]

$$\mathscr{H}(\mathbf{k}) = \begin{pmatrix} 0 & 0 & q_1 - iq_2 \\ 0 & 0 & q_3 - iq_0 \\ q_1 + iq_2 & q_3 + iq_0 & 0 \end{pmatrix}, \tag{5.2.1}$$

with $q_0 = 2t\,(h + \cos k_x a + \cos k_y a + \cos k_z a)$, $q_1 = 2t \sin k_x a$, $q_2 = 2t \sin k_y a$, $q_3 = 2t \sin k_z a$, where $\mathbf{k} = (k_x, k_y, k_z)$ denotes the momentum, a is the lattice constant, t is the hopping energy, and h is a dimensionless parameter controlling the transition between different topological phases. This model Hamiltonian has a chiral symmetry represented by $S\mathscr{H}(\mathbf{k})S^{-1} = -\mathscr{H}(\mathbf{k})$ with the unitary matrix $S \equiv \mathrm{diag}(1,1,-1)$. The Hamiltonian has three bands, with a flat middle band exactly at zero energy protected by the chiral symmetry. The other two bands have energies $E_{\pm}(\mathbf{k}) = \pm 2t[\sin^2(k_x a) + \sin^2(k_y a) + \sin^2(k_z a) + (\cos k_x a + \cos k_y a + \cos k_z a + h)^2]^{1/2}$. The topological index for this model can be characterized by the integral [22, 80]

$$\Gamma = \frac{1}{12\pi^2} \int_{\mathrm{BZ}} d\mathbf{k}\, \varepsilon^{\alpha\beta\gamma\rho} \varepsilon^{\mu\nu\tau} \frac{1}{E_+^4} q_\alpha \partial_\mu q_\beta \partial_\nu q_\gamma \partial_\tau q_\rho, \tag{5.2.2}$$

where ε is the Levi-Civita symbol with $(\alpha, \beta, \gamma, \rho)$ and (μ, ν, τ) taking values respectively from $\{0,1,2,3\}$ and $\{k_x, k_y, k_z\}$. The integration is carried over the entire Brillouin zone in momentum space.

5.2.2 Simulation using Raman-assisted tunneling

To realize the model Hamiltonian (5.2.1), we consider interaction-free fermionic atoms in an optical lattice and choose three internal atomic states in the ground state manifold (Zeeman or hyperfine states) to carry three spin states $|1\rangle, |2\rangle, |3\rangle$. The other levels in the ground state manifold are irrelevant as they are initially depopulated by the optical pumping and the transitions to these levels are forbidden during the Raman assisted atomic hopping because of a large energy detuning. The model Hamiltonian (5.2.1), expressed in real space, has the following form

$$
\begin{aligned}
H &= t\sum_{\mathbf{r}}\left[\left(2ihc^{\dagger}_{3,\mathbf{r}}c_{2,\mathbf{r}} + \text{H.c.}\right) + H_{\mathbf{rx}} + H_{\mathbf{ry}} + H_{\mathbf{rz}}\right], \\
H_{\mathbf{rx}} &= ic^{\dagger}_{3,\mathbf{r}-\mathbf{x}}(c_{1,\mathbf{r}} + c_{2,\mathbf{r}}) - ic^{\dagger}_{3,\mathbf{r}+\mathbf{x}}(c_{1,\mathbf{r}} - c_{2,\mathbf{r}}) + \text{H.c.}, \\
H_{\mathbf{ry}} &= -c^{\dagger}_{3,\mathbf{r}-\mathbf{y}}(c_{1,\mathbf{r}} - ic_{2,\mathbf{r}}) + c^{\dagger}_{3,\mathbf{r}+\mathbf{y}}(c_{1,\mathbf{r}} + ic_{2,\mathbf{r}}) + \text{H.c.}, \\
H_{\mathbf{rz}} &= 2ic^{\dagger}_{3,\mathbf{r}-\mathbf{z}}c_{2,\mathbf{r}} + \text{H.c.},
\end{aligned}
\tag{5.2.3}
$$

where $\mathbf{r}$ denotes a lattice site, $(\mathbf{x},\mathbf{y},\mathbf{z})$ represents a unit vector along the (x,y,z)-direction of a cubic lattice, and $c_{j,\mathbf{r}}$ $(j=1,2,3)$ denotes the annihilation operator of the fermionic mode at the lattice site $\mathbf{r}$ with the spin state $|j\rangle$. To implement this Hamiltonian, the major difficulty is to realize the spin-transferring hopping terms $H_{\mathbf{rx}}, H_{\mathbf{ry}}, H_{\mathbf{rz}}$ along the (x,y,z)-direction (Appendix C). The hopping terms and the associated spin transformation can be visualized diagrammatically as

$$
\begin{aligned}
&x\text{-direction: } |3\rangle \overset{i\sqrt{2}}{\curvearrowleft} |1_x\rangle \overset{\times}{\curvearrowright} + \overset{\times}{\curvearrowleft} |2_x\rangle \overset{-i\sqrt{2}}{\curvearrowright} |3\rangle + \text{H.c.} \\
&y\text{-direction: } |3\rangle \overset{-\sqrt{2}}{\curvearrowleft} |1_y\rangle \overset{\times}{\curvearrowright} + \overset{\times}{\curvearrowleft} |2_y\rangle \overset{\sqrt{2}}{\curvearrowright} |3\rangle + \text{H.c.} \\
&z\text{-direction: } |3\rangle \overset{2i}{\curvearrowleft} |2\rangle \overset{\times}{\curvearrowright} + \text{H.c.}
\end{aligned}
\tag{5.2.4}
$$

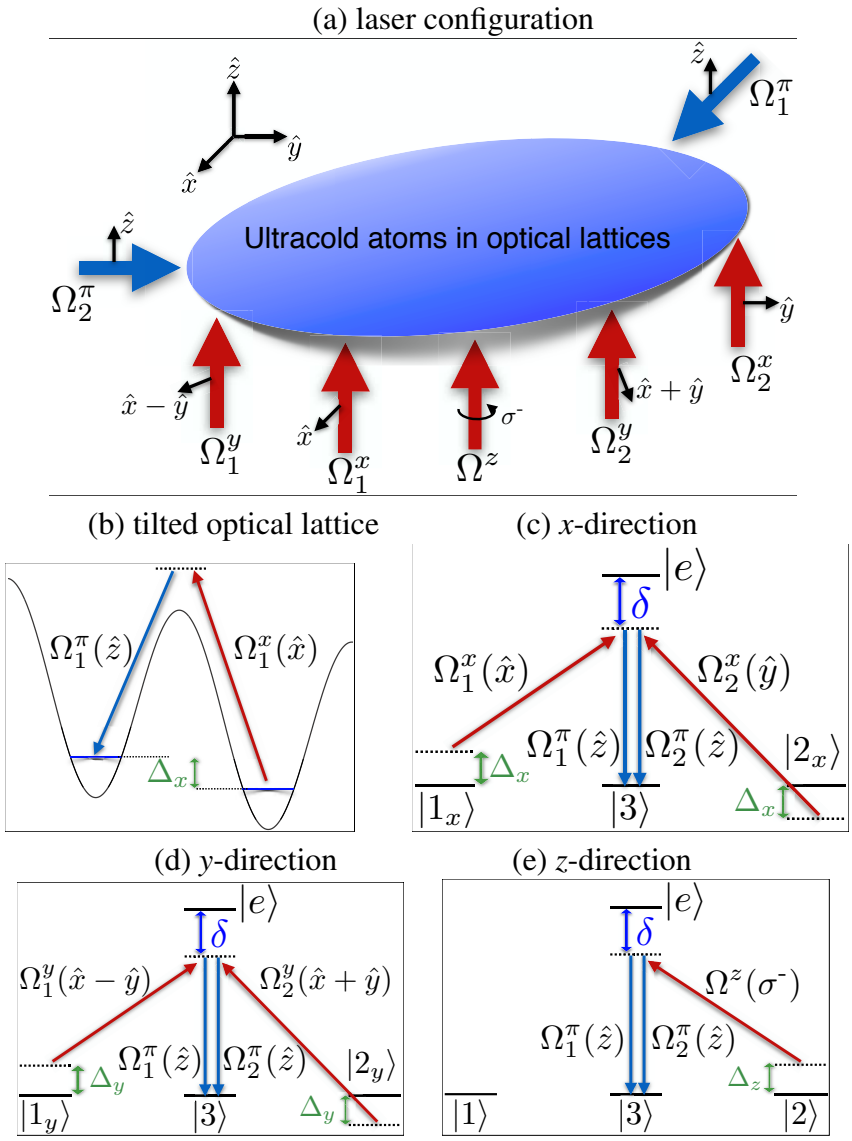

Figure 5.2.1: Schematics of the laser configuration to realize the Hamiltonian in Eq. (5.2.3). Panel (a) shows the propagation direction (big arrows) and the polarization (small arrows) of each laser beam. (b) A linear tilt $\Delta_{x,y,z}$ per site in the lattice along each direction. The detuning in each direction matches the frequency offset of the corresponding Raman beams, which are shown in panels (c), (d), and (e). The polarization of each beam (in brackets) matches the state that it couples to through the selection rule. To produce the required phase and amplitude relations of the hopping terms in Eq. (5.2.3), the Rabi frequencies for each beam are as follows: $\Omega_1^\pi = \Omega_0 e^{ikx}, \Omega_2^\pi = \Omega_0 e^{iky}, \Omega_1^x = i\sqrt{2}\Omega_0 e^{ikz}, \Omega_2^x = -i\sqrt{2}\Omega_0 e^{ikz}, \Omega_1^y = -\sqrt{2}\Omega_0 e^{ikz}, \Omega_2^y = \sqrt{2}\Omega_0 e^{ikz}, \Omega^z = 2i\Omega_0 e^{ikz}$. (see Appendix C)

where $\overset{\times}{\curvearrowright}$ indicates that hopping is forbidden along that direction, and $|1_x\rangle = (|1\rangle + |2\rangle)/\sqrt{2}$, $|2_x\rangle = (|1\rangle - |2\rangle)/\sqrt{2}$, $|1_y\rangle = (|1\rangle - i|2\rangle)/\sqrt{2}$, $|2_y\rangle = (|1\rangle + i|2\rangle)/\sqrt{2}$ are superpositions of the original spin-basis vectors $|1\rangle, |2\rangle, |3\rangle$.

We use Raman-assisted tunneling to achieve the spin-transferring hopping terms depicted in Eq. (5.2.4). Note that the parity (left-right) symmetry is explicitly broken by these hopping terms. To break the parity symmetry, we assume the optical lattice is tilted with a homogeneous energy gradient along the (x, y, z)-direction. This can be achieved, for instance, through the natural gravitational field, the magnetic field gradient, or the gradient of a dc- or ac-Stark shift [101–103]. Raman assisted hopping in a tilted optical lattice has been demonstrated in recent experiments [102, 103]. In our scheme, we require a different linear energy shift per site $\Delta_{x,y,z}$ along the (x, y, z)-direction. The ratio between $\Delta_x, \Delta_y, \Delta_z$ can be adjusted by setting the direction of the gradient field to be in a specific angle with respect to the three axes of the optical lattice. To be concrete, we take $\Delta_z \approx 1.5\Delta_y \approx 3\Delta_x$ with the energy difference lower bounded by Δ_x, and assume the natural tunneling rate $t_0 \ll \Delta_x$ so that the hopping probability $(t_0/\Delta_x)^2$ induced by the natural tunneling is negligible in this tilted lattice.

To realize the hopping terms in Eq. (5.2.4), we apply two-photon Raman transitions with the configuration (polarization and propagating direction) of the laser beams depicted in Fig. 5.2.1 (Appendix C). The internal states $|1\rangle, |3\rangle, |2\rangle$ differ in the magnetic quantum number m by one successively so that the atomic addressing can be achieved with the polarization selection rule. The π-polarized lights consist of two laser beams $\Omega_1^\pi = \Omega_0 e^{ikx}$ and $\Omega_2^\pi = \Omega_0 e^{iky}$, propagating along the x and y directions respectively, where k is the magnitude of the laser wave-vector. The other five beams $\Omega_{1,2}^{x,y,z}$ are all propagating along the z direction and the polarizations are shown in Fig. 5.2.1. The Rabi frequencies $\Omega_{1,2}^{x,y,z}$, expressed in terms of the unit Ω_0, are given in the caption of Fig. 5.2.1 to produce the required phase and amplitude relations of the hopping terms in Eq. (5.2.4). Between

the sites $\mathbf{r}$ and $\mathbf{r}+\mathbf{m}$, the Raman assisted hopping rate is given by

$$t_{\mathbf{r},\mathbf{m}} = \frac{\Omega^*_{\beta\mathbf{m}}\Omega_{\alpha\mathbf{m}}}{\delta}\int d^3\mathbf{r}' w^*(\mathbf{r}'-\mathbf{r})e^{i\delta\mathbf{k}\cdot\mathbf{r}'}w(\mathbf{r}'-\mathbf{r}-\mathbf{m}),$$

where δ is a large single-photon detuning to the excited state, $w(\mathbf{r}'-\mathbf{r})$ is the Wannier function at the site $\mathbf{r}$, and $\delta\mathbf{k} = \mathbf{k}_\alpha - \mathbf{k}_\beta$ is the momentum difference between the relevant Raman beams with the corresponding single-photon Rabi frequencies $\Omega_{\alpha\mathbf{m}}$ and $\Omega_{\beta\mathbf{m}}$. The large detuning δ guarantees that the population of the excited state, estimated by $|\Omega_0/\delta|^2$, is negligible. Because of the fast decay of the Wannier function, we consider only the nearest-neighbor Raman assisted hopping with $\mathbf{m} = \pm\mathbf{x}, \pm\mathbf{y}, \pm\mathbf{z}$. When $\delta\mathbf{k} = \mathbf{0}$, we have $t_{\mathbf{r},\mathbf{m}} = 0$ for any $\mathbf{m} \neq \mathbf{0}$ terms because of the orthogonality of Wannier functions. Let us take one of the tunneling terms along the x direction $|3\rangle \overset{i\sqrt{2}}{\curvearrowleft} |1_x\rangle$ as an example to explain the Raman assisted hopping rate. The relevant beams are given by the Raman pair $\Omega_{\alpha\mathbf{m}} = \Omega_1^x = i\sqrt{2}\Omega_0 e^{ikz}$ and $\Omega_{\beta\mathbf{m}} = \Omega_1^\pi = \Omega_0 e^{ikx}$ in Fig. 5.2.1. The laser beam Ω_1^x has two frequency components, generated, e.g., by an electric optical modulator (EOM), which are resonant with the levels $|1\rangle, |2\rangle$ respectively so that in the rotating frame the levels $|1\rangle$ and $|2\rangle$ are degenerate in energy. The beam Ω_1^x is polarized along the x direction, so, together with Ω_1^π, it couples the state $|1_x\rangle$ to the state $|3\rangle$ through the two-photon transition. The two-photon detuning Δ_x is in resonance with the potential gradient along the x direction so that the beams only induce the nearest-neighbor hopping from $\mathbf{r}$ to $\mathbf{r}-\mathbf{x}$. Using factorization of the Wannier function $w(\mathbf{r}') = w(x')w(y')w(z')$ in a cubic lattice, we find the hopping rate $t_{\mathbf{r},-\mathbf{x}} = i\sqrt{2}\beta\Omega_{\mathbf{R}}e^{i\delta\mathbf{k}\cdot\mathbf{r}}$, where $\Omega_{\mathbf{R}} \equiv |\Omega_0|^2/\delta$ and $\beta \equiv \int dx w^*(x)e^{-ikx}w(x-a)\int dy w^*(y)w(y)\int dz w^*(z)e^{ikz}w(z)$. For this hopping term, $\delta\mathbf{k} = (-k,0,k)$. Actually, for the beams shown in Fig. 5.2.1, any nonzero $\delta\mathbf{k}$ has the form $(\pm k,0,\mp k)$ or $(0,\pm k,\mp k)$, so the site dependent phase term can always be reduced to $e^{i\delta\mathbf{k}\cdot\mathbf{r}} = 1$ if we take the lattice constant a to satisfy the condition $ka = 2\pi$ by adjusting the interfering angle of

the lattice beams. Under this condition, all the hopping terms in Eq. (5.2.4) are obtained through the laser beams shown in Fig. 5.2.1 with the hopping rate $t = \beta\Omega_{\mathbf{R}}$. We assume that the Raman-assisted hopping rate t satisfies $t \ll \Delta_x$ so that any undesired couplings, such as the hopping along the z direction induced by Ω_1^x and Ω_1^π, have negligible effects because of the large detuning. The on-site spin transferring term $hc_{3,\mathbf{r}}^\dagger c_{2,\mathbf{r}}$ can be achieved through application of a simple radio-frequency (r.f.) field (or another co-propagating Raman beam). The Raman beams $\Omega_{1,2}^{x,y,z}$ and $\Omega_{1,2}^\pi$ may also induce some on-site spin transferring terms, which can be similarly compensated (canceled) with additional r.f. fields.

Although the laser configuration illustrated in Fig. 5.2.1 involves several beams, all of them can be drawn from the same laser, with the small relative frequency shift induced by an AOM (acoustic optical modulator) or EOM. The absolute frequencies of these beams and their fluctuations are not important as long as we can lock the relative frequency differences, which can be well controlled with the driving r.f. fields of the AOMs and EOMs. To show that the proposed scheme is feasible with current technology, we give a parameter estimation for typical experiments. For instance, with ^{40}K atoms of mass m in an optical lattice with the lattice constant $a = 2\pi/k = 764$ nm [115, 116], gravity induces a potential gradient (per site) $\Delta = mga/\hbar \approx 2\pi \times 0.75\,\mathrm{kHz}$. Gravity provides the gradients for free along three directions with an appropriate choice of the relative axes of the frame to satisfy $\Delta_x : \Delta_y : \Delta_z = 1 : 2 : 3$ and $\Delta = \sqrt{\Delta_x^2 + \Delta_y^2 + \Delta_z^2}$. We then have $\Delta_x \approx 2\pi \times 200$ Hz. For a lattice with depth $V_0 \approx 20E_r$, where $E_r = \hbar^2k^2/2m$ is the recoil energy, the overlap ratio $\beta \approx 10^{-2}$ and the natural tunneling rate $t_0/\hbar \sim 10^{-3}E_r/\hbar \approx 2\pi \times 8.5\,\mathrm{Hz}$ [117, 118]. For Raman beams with $\Omega_0/2\pi \approx 58\,\mathrm{MHz}$ and the single-photon detuning $\delta/2\pi \approx 1.7\,\mathrm{THz}$ [115], we have $\Omega_{\mathbf{R}} = |\Omega_0|^2/\delta \approx 2\pi \times 2\,\mathrm{kHz}$ and the Raman assisted hopping rate $t/\hbar \approx 2\pi \times 20\,\mathrm{Hz}$. Apparently, the undesired off-resonant hopping probabilities, estimated by t^2/Δ_x^2 or t_0^2/Δ_x^2, are about 1% and the effective spontaneous emission rate, estimated by $|\Omega_0/\delta|^2\Gamma_s$ ($\Gamma_s \approx 2\pi \times 6\,\mathrm{MHz}$ is the decay

rate of the excited state), is negligible during the experimental time of the order of $10/t$.

5.2.3 Detection

We now proceed to discuss detection methods to probe the exotic phases of the realized Hamiltonian. The topological index Γ defined in Eq. 5.2.2 is shown in Fig. 5.2.2(a) under different values of h. The system is topologically nontrivial for $|h| < 3$, and Γ changes at $|h| = 1, 3$, indicating a topological quantum phase transition. Hence, by varying h, one can explore various topological phase transitions, which can be probed through detection of the band structure. We calculate the band structure numerically for a homogeneous system by keeping x and y directions in momentum space and z direction in real space with open boundaries. Fig. 5.2.2(b) shows the result, revealing the macroscopic flat band as well as the surface states with Dirac cones. Experimentally, the band structure can be probed by mapping out the crystal momentum distribution $\rho_{\text{cry}}(\mathbf{k})$. By abruptly turning off the lattice potential, one could measure the momentum distribution $\rho(\mathbf{k})$, and the crystal momentum distribution can then be extracted as $\rho_{\text{cry}}(\mathbf{k}) = \rho(\mathbf{k})/|w(\mathbf{k})|^2$, where $w(\mathbf{k})$ is the Fourier transform of the Wannier function $w(\mathbf{r})$ [109, 110]. Here, we numerically calculate the crystal momentum distribution, which can be used to track the topological phase transition (Fig. 5.2.2(c)). At a fixed chemical potential, as one varies h from 0 to 2, the crystal momentum distribution reshapes accordingly when the bulk gap closes and reopens and the number of surface Dirac cones changes from 2 to 1, indicated by a change of topology of the Fermi surface (see Appendix C).

Bragg spectroscopy is a complementary detection method to reveal the Dirac cone structure [112, 113]. One could shine two laser beams at a certain angle to induce a Raman transition from an occupied spin state to another hyperfine level and focus them near the surface of the 3D atomic

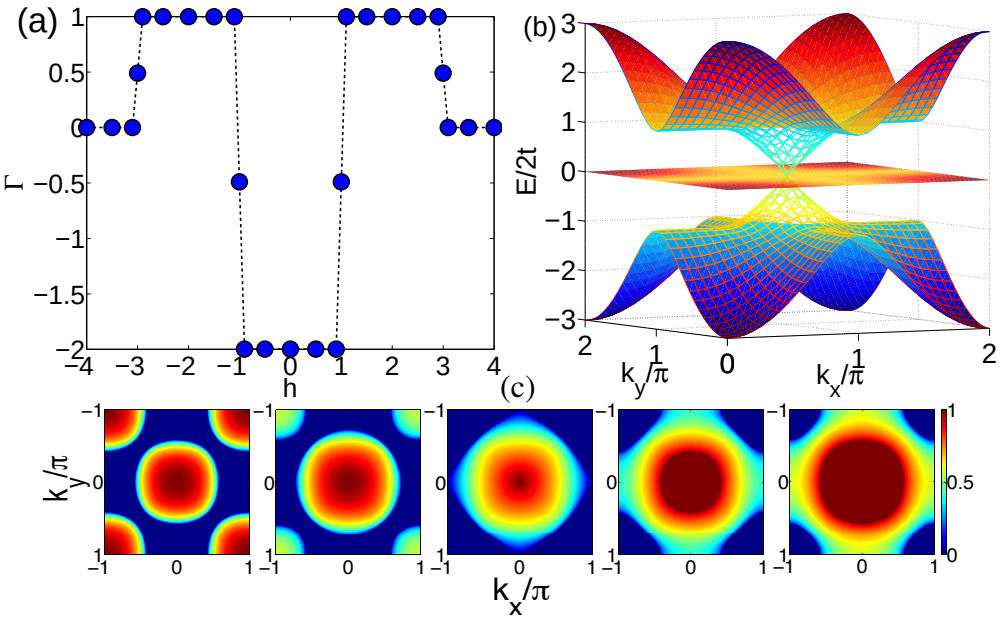

Figure 5.2.2: (Color online) (a) The topological index Γ as a function of the parameter h. (b) Energy dispersion for three bulk bands (surface plot) and surface states (mesh plot) at the boundary along z direction for $h = 2$. The minimum bulk band gap is $2t$. (c) Momentum distribution of atoms $\rho_{\text{cry}}(\mathbf{k})$ for various $h = 0, 0.5, 1, 1.5, 2$ at a fixed chemical potential $\mu/2t = -2$, which indicates a quantum phase transition that changes the topology of the Fermi surface (Appendix C). 100 layers are taken along z direction with open boundaries in (b) and (c).

gas. The atomic transition rate can be measured, which is peaked when the momentum and energy conservation conditions are satisfied. By scanning the Raman frequency difference, one can map out the surface energy-momentum dispersion relation [113]. The surface Dirac cones, with their characteristic linear dispersion, can therefore be probed through Bragg spectroscopy.

So far, we considered a homogeneous system under a box-type trap at zero temperature. In a realistic experiment, finite temperature and a weak confining harmonic trap may introduce noises. To include these effects, an important element to consider is the size of the bulk gap. In our parameter regime, the minimum band gap from the top or bottom bulk band to the middle flat band is $2t = 40\,\text{Hz}$ at $h = 2$ (Fig. 5.2.2(b)), which corresponds to a temperature around $2\,\text{nK}$.

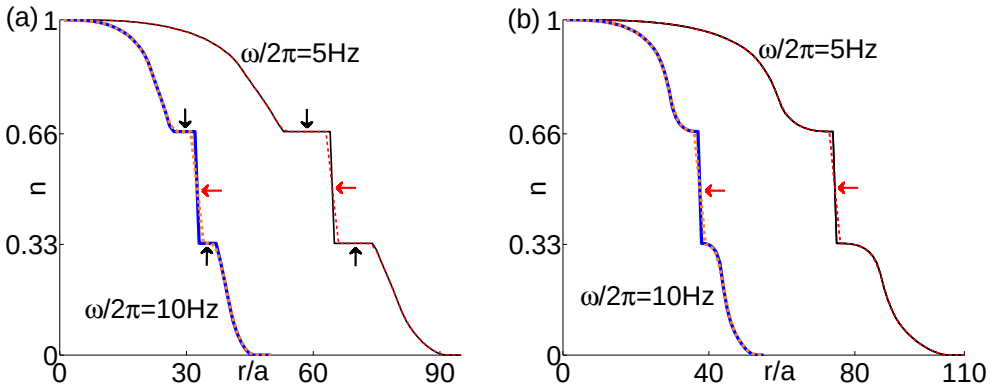

Figure 5.2.3: The atomic density profile n as a function of the radial distance r (in the unit of the lattice constant a) under the LDA. (a) $h = 0, \mu_0/2t = 3$. (b) $h = 1, \mu_0/2t = 4$. The dashed lines plot the local average density $\bar{n}$. The sharp drop in local density (marked by the horizontal arrows) indicates the presence of a flat band. The plateaus (marked by the vertical arrows) are signals of the corresponding band gap (the absence of a plateau in (b) is an indicator of the phase transition point). ^{40}K is used and $t/\hbar$ is taken to be $2\pi \times 20\,\text{Hz}$.

Sub-nanokelvin temperature is challenging but has been attained [119, 120]. It is also possible to increase the hopping rate t by a factor of 2 or 3, so that both the off-resonant hopping probability and finite temperature effects are minimized. With a considerable band gap, bulk contribution to the Bragg spectroscopy is negligible. In the following, we include the effect of a weak harmonic trap via the local density approximation (LDA) and consider the finite temperature effects to be minimal.

The band structure, in particular, the characteristic flat band, can be detected through measurement of the atomic density profile under the global harmonic trap [114, 121]. Under the LDA, the local chemical potential of the system is $\mu(r) = \mu_0 - m\omega^2 r^2/2$, where μ_0 denotes the chemical potential at the center of a spherically harmonic trap with the potential $V(r) = m\omega^2 r^2/2$. The local atomic density $n(r)$ is uniquely determined by $\mu(r)$, and μ_0 is specified by the total atom number N through $\int n(r) 4\pi r^2 dr = N$. The atomic density profile $n(r)$, which can be measured in situ in

experiments [114], is calculated and shown in Fig. 5.2.3. A steep fall/rise in $n(r)$ is a clear signature of a macroscopic flat band (Fig. 5.2.3). The plateaus at $1/3$ and $2/3$ fillings in Fig. 5.2.3(a) reveal the corresponding band gap. At $h = 1$, the plateaus vanish (Fig. 5.2.3(b)). The disappearance of the plateaus at this point indicates the phase transition where the band gap closes. In experiments, due to the finite spatial resolution, the detected signal may correspond to a locally averaged $n(r)$. The dashed lines show the local average density $\bar{n}_i = \sum_{j=-1}^{1} n_{i+j}/3$, averaged over a spherical shell of 3 lattice sites. One can see that major features associated with the band gap and the flat band remain clearly visible even when the signal is blurred by the local spatial averaging.

5.3 Summary and outlook

In summary, we have proposed an experimental scheme to realize a 3D chiral TI with a zero-energy flat band. We show that topological phase transitions and the characteristic Dirac cones can be probed through time-of-flight imaging or Bragg spectroscopy. The flat band can be revealed via detection of the atomic density profile. As interactions are added through Feshbach resonances, it will be exciting to see whether new phases emerge in this topological flat band as in the case of 2D fractional quantum Hall effect. The experimental realization of this model will mark an important advance in the ultracold atom simulation of topological phases. It will also add to the zoo of topological phases in 3D beyond the well-studied $\mathbb{Z}_2$ topological insulator protected by the time-reversal symmetry.

CHAPTER VI

Measuring topological invariants in cold atomic systems

6.1 Introduction

Cold-atom experiments in optical lattices offer a versatile platform to realize various topological quantum phases. A key challenge in those experiments is to unambiguously probe the topological order. Here, we propose two generic methods to accomplish this task, one for topological band insulators and the other for interacting insulators.

In the first section, We propose a method to directly measure the characteristic topological invariants (order) based on the time-of-flight imaging of cold atoms. The method is generally applicable to detection of topological band insulators in one, two, or three dimensions characterized by integer topological invariants. Using detection of the Chern number for the two-dimensional anomalous quantum Hall states and the Chern-Simons term for the three-dimensional chiral topological insulators as examples, we show that the proposed detection method is practical, and robust to typical experimental imperfections such as limited imaging resolution, inhomogeneous trapping potential, and disorder in the system.

In the second section, based on the momentum-resolved Raman or radio-frequency spectroscopy, we propose a general scheme to measure the characteristic topological invariants for strongly interacting cold-atomic systems. Our method relies on the Green's function formulation of the topological invariants and is applicable to any spatial dimensions, with or without symmetries. Using an interacting one-dimensional topological insulator as an example, we demonstrate that our scheme is robust against realistic experimental imperfections such as the inhomogeneous trapping potential and limited imaging resolution.

6.2 Band topology in free fermionic systems

The nontrivial topology of Bloch bands is at the heart of exotic topological phases of matters [7–9]. The band topology is often described by a topological invariant [19–21], which may be manifested in some transport properties, such as the quantized Hall conductivity in integer quantum Hall states [6,70,122]. Intensive and parallel efforts in the condensed matter and cold atom communities have been focused on the realization of these exotic phases and the identification of nontrivial band topology. Especially, recent experimental advances in spin-orbit coupling [88, 116, 123–126] have raised cold atomic systems to the forefront of these efforts, portraying it as a promising platform to realize various topological phases [72,102,103,127–130]. However, standard transport measurements [86,131] and edge state probes [14,30,34] are rather challenging for atomic systems [132]. Novel schemes have thus been proposed to develop detection methods suitable for cold atoms.

Current proposals to probe the nontrivial band topology divide broadly into two categories. The first is in the spirit of mimicking the transport measurement or angle-resolved photoemission spectroscopy in solid systems, such as through atomic density responses to an external field or

force [133, 134], charge pumping [135], or through Bragg scattering signals [136, 137]. The second differs from solid systems, which may involve retrieving the Berry phase or Berry curvature through dynamics [138–141] or directly mapping out a two-band Hamiltonian [142]. However, current methods mostly rely on quantum Hall like physics, and apply to the lowest band. They are not readily applicable to probe the nontrivial topology of other exotic phases, such as the Su-Schrieffer-Heeger (SSH) model [143, 144] in one dimension (1D), or the chiral topological insulators [24, 100] and Hopf insulators [23, 41] in 3D. A simple yet general detection method is in demand.

In this section, we introduce a novel scheme to directly measure the topological structures of Bloch bands in optical lattices. One may observe that topological invariants are typically expressed as an integral in the Brillouin zone involving the Bloch wavefunction and its derivatives. In principle, if we can measure the wavefunction, we can extract the topological invariant. Quantum mechanics immediately prohibits that since only the physically measurable atomic densities can be retrieved. Nevertheless, we show that time-of-flight (TOF) measurements in a rotated atomic basis, which can be implemented by a radio-frequency (r.f.) pulse (or a co-propagating Raman beam), provide the crucial information of relative phases among different components of the Bloch wavefunction. Hence, the wavefunction can be measured up to an overall phase at each momentum point. This nondeterministic overall phase is associated with a $U(1)$ gauge freedom, and hinders the calculation of derivatives in momentum space and in turn the topological invariant. In particular, the gauge obstruction associated with a nonzero Chern number forbids a global smooth Berry connection. This problem can be circumvented by defining a $U(1)$-link [145], and we show that the topological invariants can be extracted from experiments regardless of the overall phase arbitrariness.

6.2.1 General method

First, let us outline the general recipe. Consider a general real-space lattice Hamiltonian with N-quantum degrees of freedom in each unit cell. In momentum space, it has N bands and can be described by a N-by-N Hermitian matrix $H(\mathbf{k})$. In general, $H(\mathbf{k})$ may contain degenerate bands, but here we consider non-degenerate bands for simplicity. The energy spectrum can be obtained by solving the Schröinger equation for each $\mathbf{k}$ in the Brillouin zone (BZ):

$$H(\mathbf{k})|u_b(\mathbf{k})\rangle = E_b(\mathbf{k})|u_b(\mathbf{k})\rangle, \tag{6.2.1}$$

where $b = 1,2,\cdots,N$ denotes an index labeling different bands and $|u_b(\mathbf{k})\rangle$ is the Bloch wavefunction for the b-th band. A general Bloch wavefunction has the form

$$|u_b(\mathbf{k})\rangle = \sum_{m=1}^{N} c_{m,b}(\mathbf{k})|m\rangle, \tag{6.2.2}$$

where $|m\rangle$ $(m = 1,2,...,N)$ are basis vectors and $c_{m,b}(\mathbf{k})$ are complex numbers satisfying the normalization condition $\sum_m |c_{m,b}(\mathbf{k})|^2 = 1$. With ultra-cold atoms in optical lattices, the crystal momentum distribution $n_{m,b}(\mathbf{k})$ for the m-th pseudospin can be obtained through TOF measurements in the b-th BZ. This $n_{m,b}(\mathbf{k})$ reveals some partial information about $c_{m,b}(\mathbf{k})$:

$$|c_{m,b}(\mathbf{k})|^2 = n_{m,b}(\mathbf{k}) / \sum_{q=1}^{N} n_{q,b}(\mathbf{k}). \tag{6.2.3}$$

However, the relative phase factors among $c_{m,b}$s are also indispensable to the extraction of topological invariants. These relative phases can be determined from density measurements in a rotated basis, which can be accomplished by applying a r.f. pulse (or a copropagating Raman pulse). For instance, to obtain the relative phase factor between $c_{q,b}(\mathbf{k})$ and $c_{q',b}(\mathbf{k})$, one may

first apply a $\pi/2$-pulse coupling the pseudospin $|q\rangle$ and $|q'\rangle$ to measure the density $|c_{q,b}(\mathbf{k})+c_{q',b}(\mathbf{k})|^2/2 = n_{(|q\rangle+|q'\rangle)/\sqrt{2}}(\mathbf{k})/\sum_{q=1}^{N} n_{q,b}(\mathbf{k})$ and then apply another phase-shifted $\pi/2$-pulse to measure $|ic_{q,b}(\mathbf{k})+c_{q',b}(\mathbf{k})|^2$. The relative phase can be deduced from $|c_{q,b}(\mathbf{k})|$, $|c_{q',b}(\mathbf{k})|$, $|c_{q,b}(\mathbf{k})+c_{q',b}(\mathbf{k})|^2$ and $|ic_{q,b}(\mathbf{k})+c_{q',b}(\mathbf{k})|^2$. In a similar manner, all relative phases among $c_{m,b}$s can be specified and the Bloch wavefunction can be determined up to an overall phase.

In an experiment, one "pixelizes" the TOF image and measure the density distribution in each square of the pixelized Brillouin zone. The wavefunction is fixed up to an overall phase at each square with the above method. However, the arbitrary phase for different squares poses obstacle to the extraction of topological invariants. This difficulty can be avoided by defining a $U(1)$-link at each lattice point $\mathbf{k_J}$ on the discrete BZ [145]: $U_\nu^{(b)}(\mathbf{k_J}) \equiv \langle u_b(\mathbf{k_J})|u_b(\mathbf{k_{J+\hat{\nu}}})\rangle/|\langle u_b(\mathbf{k_J})|u_b(\mathbf{k_{J+\hat{\nu}}})\rangle|$, where $\hat{\nu} = \hat{x},\hat{y},\hat{z}$, a unit vector in the respective direction. Next, a gauge-independent lattice field strength can be defined as

$$\begin{aligned} \mathscr{F}_{\mu\nu}^{(b)}(\mathbf{k_J}) &\equiv \ln \frac{U_\mu^{(b)}(\mathbf{k_J})U_\nu^{(b)}(\mathbf{k_{J+\hat{\mu}}})}{U_\mu^{(b)}(\mathbf{k_{J+\hat{\nu}}})U_\nu^{(b)}(\mathbf{k_J})}, \\ -\pi &< -i\mathscr{F}_{\mu\nu}^{(b)}(\mathbf{k_J}) \leq \pi. \end{aligned} \tag{6.2.4}$$

$\mathscr{F}_{\mu\nu}^{(b)}(\mathbf{k_J})$ can be obtained from the TOF images of the whole pixelized BZ. In the large lattice size limit, the field strength reduces to the familiar Berry curvature (see the definition below Eq. (6.2.6)) for each Bloch band. In this sense, one may regard $\mathscr{F}_{\mu\nu}^{(b)}(\mathbf{k_J})$ as a discrete version of the Berry curvature. With this lattice field strength at hand, topological invariants for different classes of topological phases can be extracted.

The above recipe is general as it is applicable to different topological phases in any spatial dimension. To show how it works, in the following we apply this general approach to two concrete models, one for 2D quantum anomalous Hall (QAH) effect and the other for 3D chiral topological

insulators (CTIs).

6.2.2 Two examples

The above recipe is general as it is applicable to different topological phases in any spatial dimension. To show how it works, in the following we apply this general approach to two concrete models, one for 2D quantum anomalous Hall (QAH) effect and the other for 3D chiral topological insulators (CTIs).

2D quantum anomalous Hall effect— The QAH effect is a fundamental transport phenomenon in solid physics. It is a special kind of the quantum Hall effect, where spontaneous magnetization combined with spin-orbit coupling may give rise to a quantized Hall conductivity in the absence of an external magnetic field [146]. A solid-state experiment has recently observed this exotic phenomenon in thin films of a magnetically doped topological insulator [131]. A simple square-lattice Hamiltonian which captures the essential physics of the QAH effect has the following form in real space:

$$\begin{aligned} H_{\rm QAH} &= \lambda_{\rm SO}^{(\mu)} \sum_{\mathbf{r}\hat{\mu}} [(a_{\mathbf{r}\uparrow}^{\dagger} a_{\mathbf{r}+\hat{\mu}\downarrow} - a_{\mathbf{r}\uparrow}^{\dagger} a_{\mathbf{r}-\hat{\mu}\downarrow}) + \text{H.c.}] \\ &+ t \sum_{\langle \mathbf{r},\mathbf{s} \rangle} (a_{\mathbf{r}\uparrow}^{\dagger} a_{\mathbf{s}\uparrow} - a_{\mathbf{r}\downarrow}^{\dagger} a_{\mathbf{s}\downarrow}) + h \sum_{\mathbf{r}} (a_{\mathbf{r}\uparrow}^{\dagger} a_{\mathbf{r}\uparrow} - a_{\mathbf{r}\downarrow}^{\dagger} a_{\mathbf{r}\downarrow}), \end{aligned} \tag{6.2.5}$$

where $a_{\mathbf{r}\sigma}^{\dagger}(a_{\mathbf{r}\sigma})$ is the creation (annihilation) operator of the fermionic atom with pseudospin $\sigma = (\uparrow,\downarrow)$ at site $\mathbf{r}$, and $\hat{\mu} = \hat{x},\hat{y}$ is a unit lattice vector along the x,y direction. The first term in the Hamiltonian describes the spin-orbit coupling. The second and the third term denote the spin-conserved nearest-neighbor hoppings and Zeeman interactions respectively. It was shown that $H_{\rm QAH}$ may be realized with cold fermionic atoms trapped in a blue-detuned square optical lattice

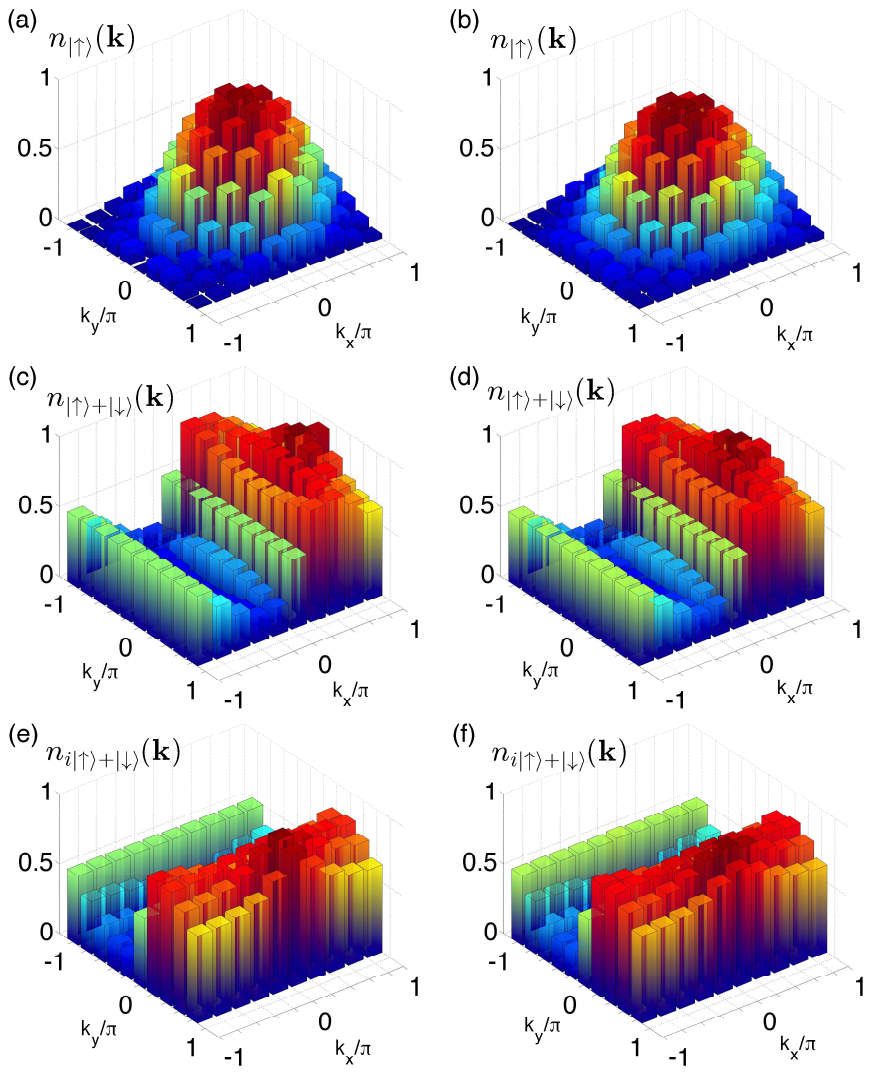

Figure 6.2.1: (color online). Density distributions in momentum space for the first band of H_{QAH} with lattice size 10×10. The total density at each $\mathbf{k}$ is normalized to unity (e.g. $n_{|\uparrow\rangle}(\mathbf{k}) + n_{|\downarrow\rangle}(\mathbf{k}) = 1$). (a), (c) and (e) refer to the case with periodic boundary conditions; (b), (d), and (f) correspond to open boundary conditions with a harmonic trap (γ_T) and random perturbations (γ_P). The parameters are chosen to be $\lambda_{\mathrm{SO}}^{(x)}/t = \lambda_{\mathrm{SO}}^{(y)}/t = 1$, $h/t = 1$, $\gamma_T/t = 0.01$, and $\gamma_P/t = 0.1$.

[115].

In momentum space, this Hamiltonian has two Bloch bands. The topological structure of this model is characterized by the Chern number, which is defined for the b-th band as

$$C_b = \frac{1}{2\pi i}\int_{\mathrm{BZ}} dk_x dk_y F_{xy}(\mathbf{k}), \tag{6.2.6}$$

where the Berry curvature $F_{xy}(\mathbf{k}) = \partial_{k_x}A_y(\mathbf{k}) - \partial_{k_y}A_x(\mathbf{k})$ and Berry connection $A_\mu(\mathbf{k}) = \langle u_b(\mathbf{k})|\partial_{k_\mu}|u_b(\mathbf{k})\rangle$ ($\mu = x, y$). By direct calculations, it is easy to show that $C_2 = -C_1 = \mathrm{sgn}(h)$ if $0 < |h| < 4t$ and $C_2 = -C_1 = 0$ otherwise. Experimentally, one can get the wavefunction $|u_b(\mathbf{k_J})\rangle$ at momentum points $\mathbf{k_J}$ from TOF images, and thus obtain the discretized Berry curvature $\mathscr{F}^{(b)}_{\mu\nu}(\mathbf{k_J})$. The Chern number can then be approximated as $C_b \approx \frac{1}{2\pi i}\sum_{\mathbf{J}} \mathscr{F}^{(b)}_{xy}(\mathbf{k_J})$.

In experiments, one loads fermionic atoms (^{40}K for instance) into an optical lattice with unit filling so that the lower band is fully occupied. The laser intensities may be tuned to reach the nontrivial topological phase [115]. Once the approximate ground state is attained, one ramps down the lattice potential adiabatically to map the conserved crystal momentum onto the free-space momentum. The crystal momentum distribution can then be observed via time-of-flight measurements. Note that the spin-resolved distribution $n_{|\uparrow\rangle}(\mathbf{k})$ and $n_{|\downarrow\rangle}(\mathbf{k})$ can be measured by transferring one pseudospin to another internal state before taking an absorption image of the expanded atom cloud. The experiment can be repeated with rotated basis to measure $n_{|\uparrow\rangle+|\downarrow\rangle}(\mathbf{k})$ and $n_{i|\uparrow\rangle+|\downarrow\rangle}(\mathbf{k})$, which can be achieved with a fast $\pi/2$-pulse coupling the two pseudospin states before TOF measurements. The simulated momentum distributions are shown in Fig. 6.2.1. This gives direct access to $|c_\uparrow(\mathbf{k})|, |c_\downarrow(\mathbf{k})|$ and the relative phase between $c_\uparrow(\mathbf{k})$ and $c_\downarrow(\mathbf{k})$. The Chern number can then be extracted with the above method, and is recorded in Table D.1, for both the nontrivial phase ($h/t = 1$) and the trivial phase ($h/t = 5$).

	h(m)	Size	Periodic	Open	Trap	Pert.+Trap
QAH	1	4^2	-1	-1	-1	-1
	1	10^2	-1	-1	-1	-1
	5	10^2	0	0	0	0
CTI	2	10^3	1.041	1.056	1.055	1.080
	2	12^3	1.031	1.009	0.981	1.014
	4	10^3	0	$-2*10^{-4}$	$1.1*10^{-3}$	$1.2*10^{-3}$

Table 6.4: Simulated experimental results of the topological invariants for different lattice sizes under various realistic conditions. For QAH, the invariant is the Chern number for the first band (C_1), whereas for CTI, it is the Chern-Simons term for the middle flat band (CS_2/π). Results for both the nontrivial phase ($h = 1$ for QAH and $m = 2$ for CTI) and the trivial phase ($h = 5$ for QAH and $m = 4$ for CTI) are presented. All these invariants are extracted directly from the momentum density distribution images. The parameters are the same as in Fig. 6.2.1 and Fig. 6.2.2.

To simulate a realistic experimental condition, we consider a finite-size lattice with open boundary conditions. In addition, we add a harmonic trap parametrized by γ_T and a random perturbation term parametrized by γ_P into H_{QAH} (for details, see Appendix D). We numerically diagonalize the real-space Hamiltonian on a finite lattice with different number of sites and calculate the corresponding momentum density distributions under different conditions. Fig. 6.2.1(b), (d), and (f) show the result for open boundary conditions with a harmonic trap and some random perturbations. The Chern numbers are guaranteed to be integers with our method [145] and are shown in the first part of Table D.1 under different conditions. Numerical results show that the quantized Chern number is very robust against perturbations and the harmonic trapping potential. It is also exceptionally robust to coarse discretizations, as a 4×4 BZ pixelization is adequate to produce the expected results. This is a remarkable advantage compared to some previous work [142], where a 20×20 discretization still deviates roughly 10% from the theoretical value.

3D chiral topological insulator— Chiral topological insulators have a chiral symmetry (also known as the sublattice symmetry) and belong to the AIII class in the periodic table for topological insu-

lators and superconductors [19–21]. A simple Hamiltonian for the 3D CTI is [80]:

$$\begin{aligned} H_{\mathrm{CTI}} &= \frac{t}{2}\sum_{\mathbf{r}}\sum_{j=1}^{3}[\psi_{\mathbf{r}}^{\dagger}(iG_{3+j}-G_7)\psi_{\mathbf{r}+\mathbf{e}_j}+\mathrm{H.c.}] \\ &\quad +m\sum_{\mathbf{r}}\psi_{\mathbf{r}}^{\dagger}G_7\psi_{\mathbf{r}}, \end{aligned} \tag{6.2.7}$$

where the operator $\psi_{\mathbf{r}}^{\dagger}=(a_{\mathbf{r},1}^{\dagger},a_{\mathbf{r},2}^{\dagger},a_{\mathbf{r},3}^{\dagger})$ with $a_{\mathbf{r},\alpha}^{\dagger}(\alpha=1,2,3)$ creating a fermion at site $\mathbf{r}$ in the state $|\alpha\rangle$, $\mathbf{e}_1,\mathbf{e}_2,\mathbf{e}_3$ are unit vectors along x,y,z directions, and G_ν ($\nu=4,5,6,7$) is the νth Gell-Mann matrix (Appendix D). This model is a minimal band model for 3D chiral topological insulators. In momentum space, it has three gapped bands, with an exact zero-energy flat band in the middle protected by the chiral symmetry. In Ref. [24], a realistic experimental scheme was proposed to realize this Hamiltonian with cold fermionic atoms in an optical lattice. It was shown that the topologically protected edge states—the Dirac cones—can be revealed through TOF imaging or Bragg spectroscopy and the flat band can be pinned down via measurement of the atomic density profile in a weak global trap. Here, as an application of our general method, we show that the topology of each band can be probed through TOF measurements. In 3D, the topological structure of b-th Bloch band can be characterized by the Chern-Simons term:

$$CS_b = -\frac{1}{4\pi}\int_{\mathrm{BZ}} d\mathbf{k}\varepsilon^{\mu\nu\tau}A_\mu(\mathbf{k})\partial_{k_\mu}A_\tau(\mathbf{k}), \tag{6.2.8}$$

where $A_\mu(\mathbf{k})=\langle u_b(\mathbf{k})|\partial_{k_\mu}|u_b(\mathbf{k})\rangle$ ($\mu=x,y,z$). Explicit calculations show that $CS_3=CS_1=CS_2/4=\pi\Gamma(m)/4$ with $\Gamma(m)=-2$ for $|m|<1$, $\Gamma(m)=1$ for $1<|m|<3$ and $\Gamma(m)=0$ otherwise. Similarly, this Chern-Simons term can be readily extracted from TOF images. Following the same procedure, one could obtain the Bloch wavefunction at discretized momentum points $\mathbf{k_J}$ and in turn the discretized Berry curvature $\mathscr{F}_{\mu\nu}^{(b)}(\mathbf{k_J})$. The Berry connection $A_\mu(\mathbf{k_J})$ can be obtained from

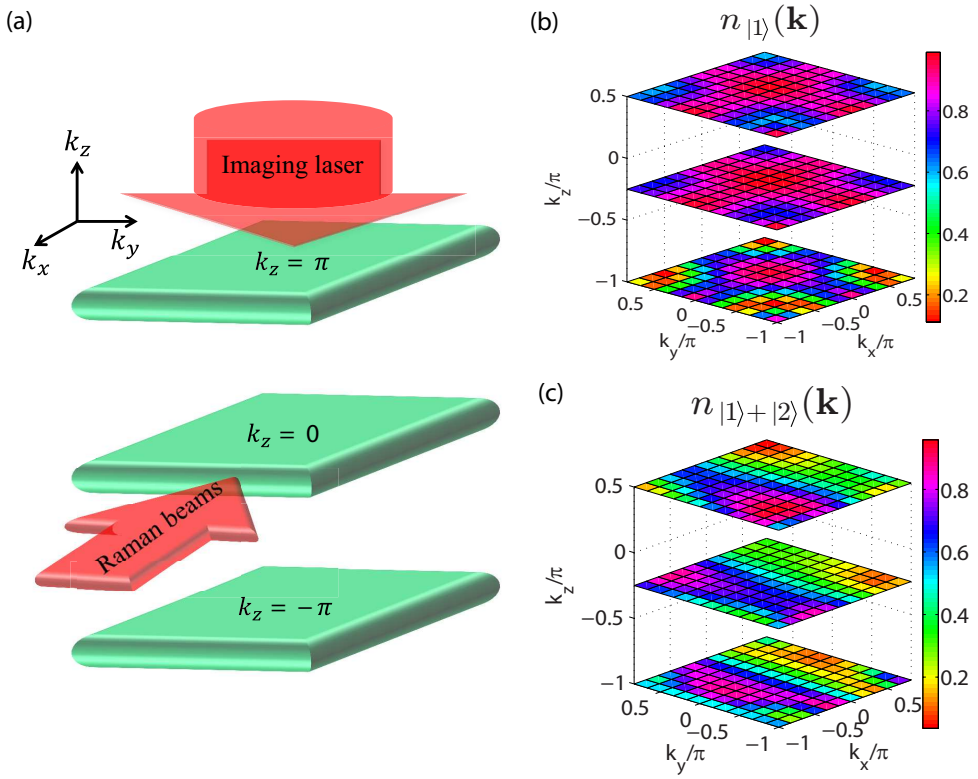

Figure 6.2.2: (color online). (a) A schematics to show how to observe 3D momentum density distributions in TOF measurement. (b) and (c): Density distributions for the middle flat band of H_{CTI} with open boundary conditions and lattice size $12 \times 12 \times 12$. Layers corresponding to $k_z = -\pi, -\pi/4, \pi/2$ are displayed. The parameters are $m/t = 2$, $\gamma_T/t = 0.001$ and $\gamma_P/t = 0.1$. The Chern-Simons term extracted from these density distributions is $CS_2 = 1.014\pi$.

$\mathscr{F}^{(b)}_{\mu\nu}(\mathbf{k_J})$ by solving the magnetostatic equation $\nabla \times \mathbf{A} = \mathbf{F}$ in momentum space with the Coulomb gauge $\nabla \cdot \mathbf{A} = 0$. Finally, the Chern-Simons term can be approximated by a discrete sum. It is worthwhile to note that the absence of a gauge obstruction here permits a globally well-defined Berry connection. Thus, an alternative method would be to define a globally fixed gauge for the Bloch wavefunction obtained from TOF images (for example by specifying one nonzero component of the wavefunction to be real) and compute the Berry connection directly.

In experiments, TOF images typically provide a 2D momentum density distribution, with the op-

tical density integrated along the third direction. In 3D, to obtain the full Bloch wavefunction, we need a 3D momentum density distribution in principle. However, our simulation in Table D.1 shows that around $10\,k_z$ layers are sufficient to yield the quantized Chern-Simons term (fewer layers are needed if we increase the resolution in x, y directions). Hence, we suggest to take TOF images for discrete layers of k_z as follows (schematics in Fig. 6.2.2a): (i) turn off the lattice and trapping potential to let the atomic cloud expand for a sufficient long time; (ii) use a pair of narrow-width co-propagating Raman beams in x-direction to transfer the desired layer of atoms to another internal state. (iii) shine an imaging laser beam with a proper frequency along z-direction to map out the density distribution of the transferred layer in x-y plane. Fig. 6.2.2(b) and (c) show some density distributions for the middle flat band. Three layers are displayed in each panel. The Chern-Simons term is recorded in Table D.1 for different conditions. As the number of pixels increases, the Chern-Simons term converges to the expected theoretical values rapidly. In fact, a $12 \times 12 \times 12$ pixelization deviates only 3% from the desired value. This remarkable efficiency will greatly simplify the measurement process.

6.3 Topological phases with strong interactions

Electron-electron interaction plays a vital role in many remarkable physical phenomena, such as high-T_c superconductivity and fractional quantum Hall effect. The more recent discovery and exploration of topological phases of matter has also deepened our understanding of many-body physics [7,8]. Connecting both, topological phases with strong interactions are currently becoming an active area of research [17, 67, 87, 147–154]. Unlike topological phases for free fermionic systems, which are well understood with topological band theory and classified by a periodic table according to the system symmetry and dimensionality [19,20], those with strong interactions

are far less understood: many other exotic phenomena may emerge, such as the fractional Chern insulators [106–108] or chiral spin liquids [52].

However, many-particle interacting systems are notoriously hard to solve and understand. The difficulty of classically solving large quantum problems has led Feynman to introduce his visionary idea of quantum simulation in the 1980s [155], i.e., to use a more controllable system to simulate another. Three decades later, cold atomic systems are pushed to the forefront of this endeavor [72]. It possesses a high degree of controllability, such as addressing and detection at the single-atom level [156–159] or the detuning of interatomic interactions over several orders of magnitude via Feshbach resonances [104]. Recent atomic realizations of superfluid to Mott-insulator transition [160], BCS-BEC crossover [161], and synthetic gauge field [89, 102, 103, 123, 162] have offered a promising outlook to understand many-body physics with cold atoms. For the simulation of topological phases, a central question arises for atomic systems, i.e., how to unambiguously and directly probe the characteristic topological invariant. Numerous notable schemes are proposed for noninteracting systems recently [25, 118, 133–142, 163, 163–167], but a generic method to probe the topological invariants for strongly interacting systems has been lacking.

In this section, we fill the gap. We propose a versatile scheme to measure various topological invariants for strongly interacting topological phases realized with cold atoms. For noninteracting systems, topological invariants are generally obtained from the single-particle Hamiltonian or Bloch wavefunctions. Generalizing to interacting systems, these invariants can typically be expressed as integrals of the Green's functions in frequency and momentum space. We show that the standard Raman or radio-frequency (rf) spectroscopy, combined with spin-resolved time-of-flight imaging, can provide sufficient information to the tomography of the desired Green's functions and hence to the direct extraction of the corresponding topological invariants. The proposed scheme is generic, applicable to topological phases in one, two, or three dimensions (3D) with or without

symmetries. Its robustness against realistic experimental imperfections is explicitly demonstrated with numerical simulations of a simple 1D topological insulator (TI) model with strong interactions.

6.3.1 Basic idea

To begin with, let us briefly review how the topological invariants are defined for general interacting systems. It is well known that in the noninteracting limit, the topological properties of a fermionic system are described by Bloch band topological invariants, such as the Thouless-Kohmoto-Nightingale-den Nijs (TKNN) invariant (also called the first Chern number) [122] and the Z_2 invariants [11, 12, 40]. However, these invariants cannot be applied to interacting systems due to the lack of 'occupied band', an essential concept in defining band topological invariants. One elegant generalization to interacting systems is to use twisted boundary conditions [168], but it requires the entire information of the ground state wavefunctions, which is hard to obtain experimentally. In addition, this method cannot be readily generalized to Z_2 insulators [169]. An alternative approach is to formulate topological invariants as integrals of Green's functions [169–175]. These invariants then acquire a clear physical meaning as the quantized coefficients of topological field theory [45] and as an indication of bulk-boundary correspondence [175]. They are applicable to integer as well as Z_2 insulators, but may take different expressions for each symmetry class in different spatial dimensions [169, 173, 174, 176–178]. Our proposed detection scheme works for each type of those topological insulators. Here, let us use the TKNN invariant as an example to explain further. The generalized TKNN invariant for interacting 2D insulators in symmetry class A can be expressed in terms of the Green's function as [170, 171, 173]:

$$C_1 = \frac{1}{24\pi^2}\int dk_0 d\mathbf{k}\mathrm{Tr}[\varepsilon^{\alpha\beta\gamma}G\partial_\alpha G^{-1}G\partial_\beta G^{-1}G\partial_\gamma G^{-1}], \tag{6.3.1}$$

where $G \equiv G(i\omega, \mathbf{k})$ is the Matsubara Green's function [179] in frequency-momentum space and α, β, γ run through k_0, k_1, k_2, with $k_0 = i\omega$ denoting the Matsubara frequency (imaginary frequency). It is usually difficult to acquire information of the Green's function at all frequencies, as required in Eq. (6.3.1). Recently, it was shown that zero-frequency Green's function is in fact sufficient to construct the topological invariants provided that $G(i\omega, \mathbf{k})$ is nonsingular [169, 176]. Let us define the so-called effective '*topological Hamiltonian*' as $H_{\text{eff}} \equiv -G^{-1}(0, \mathbf{k})$, which in the noninteracting limit reduces to the free single-particle Hamiltonian. Eq. (6.3.1) then has a simplified expression:

$$C_1 = \frac{1}{2\pi} \int d\mathbf{k} \mathscr{F}_{xy}, \tag{6.3.2}$$

where $\mathscr{F}_{ij} = \partial_i \mathscr{A}_j - \partial_j \mathscr{A}_i$, and $\mathscr{A}_i = -i \sum_\alpha \langle \mathbf{k}\alpha | \partial_i | \mathbf{k}\alpha \rangle$. Here, $|\mathbf{k}\alpha\rangle$ denotes the eigenvectors of H_{eff} with negative eigenvalues. With this effective Hamiltonian picture, the calculation of the generalized TKNN invariant is analogous to that of free systems without interactions.

In experiment, if one can measure the Green's function, the topological invariant for the interacting system can be directly extracted as discussed above. However, the Green's function is not a physical observable and hence cannot be measured directly. A possible detour is to measure the spectral function $A(\omega, \mathbf{k})$ and subsequently construct the Green's function as [179]

$$G(i\omega, \mathbf{k}) = \int d\omega' \frac{A(\omega', \mathbf{k})}{i\omega - \omega'}. \tag{6.3.3}$$

In a solid experiment, $A(\omega, \mathbf{k})$ with $\omega < 0$ ($\omega > 0$) can be measured using direct (inverse) angle-resolved photoemission spectroscopy (ARPES) [180]. In a cold atom system, an analogue of ARPES and inverse ARPES measurements can be accomplished through Raman [181, 182] or rf [183] spectroscopy. Here, we focus on the detection scheme for atomic experiments. Let us consider for instance an interacting topological phase realized with cold atoms with two internal

states (spins) $|\alpha\rangle$ and $|\alpha'\rangle$. There may be strong interactions between these states. Now consider another internal state $|\beta\rangle$ that is initially unoccupied and does not interact with the states $|\alpha\rangle$ and $|\alpha'\rangle$. This $|\beta\rangle$-state has known energy dispersion $\varepsilon_{\beta\mathbf{k}}$ at momentum $\mathbf{k}$. A stimulated Raman spectroscopy can be applied to transfer atoms from the state $|\alpha\rangle$ to $|\beta\rangle$ via an intermediate excited state $|\gamma\rangle$, by using two laser beams with frequency difference $\Omega = \omega_1 - \omega_2$ and wave vector difference $\mathbf{q} = \mathbf{k}_1 - \mathbf{k}_2$. The beams are far from resonance with the excited state $|\gamma\rangle$ so that spontaneous emission can be neglected. For a uniform system, the transfer rate to state $|\beta\rangle$ at some momentum $\mathbf{k}$ can be computed using Fermi's golden rule and is proportional to the spectral function of atoms in state $|\alpha\rangle$ [181, 182],

$$\Gamma_{\mathbf{k}}(\Omega, \mathbf{q}) \propto n_F(\varepsilon_{\beta\mathbf{k}} - \hbar\Omega - \mu) A_\alpha(\varepsilon_{\beta\mathbf{k}} - \hbar\Omega - \mu, \mathbf{k} - \mathbf{q}), \tag{6.3.4}$$

where μ is the chemical potential of the interacting system and n_F is the Fermi distribution factor with $n_F(\hbar\omega) = 0$ for $\omega > 0$ at zero temperature. Therefore, time-of-flight absorption image of $|\beta\rangle$-state atoms reveals the transfer rate $\Gamma_{\mathbf{k}}$ as a function of the final momentum $\mathbf{k}$ of the scattered atoms. In turn, this yields the $\mathbf{k}$ dependence of the spectral function. Its frequency dependence can be obtained by repeating the experiment with different frequencies Ω. As a result, $A(\omega, \mathbf{k})$ with $\omega < 0$ can be measured. This applies when the state $|\beta\rangle$ is initially empty. If instead a large incoherent population of atoms is initially present in the state $|\beta\rangle$, the same analysis leads to a reversed Raman process. Measuring the decrease of the $|\beta\rangle$-state population will produce $A(\omega, \mathbf{k})$ with $\omega > 0$ [181]. The above photoemission and photoabsorption Raman processes are similar to the direct and inverse ARPES measurements in solid systems, except that some well-known problems in ARPES, such as the non-conservation of total momentum and the surface effect, are absent in atomic experiments. An alternative and simpler setup is to use rf spectroscopy [161, 183],

which directly couples the $|\alpha\rangle$-state and the $|\beta\rangle$-state. It is equivalent to the Raman spectroscopy above with fixed momentum $\mathbf{q} = \mathbf{0}$ [181].

After a series of measurements produces $A_\alpha(\omega, \mathbf{k})$, one component of the Green's function $G_{\alpha\alpha}(i\omega, \mathbf{k})$ can be computed straightforwardly with Eq. (6.3.3). A similar procedure gives $A_{\alpha'}(\omega, \mathbf{k})$ and $G_{\alpha'\alpha'}(i\omega, \mathbf{k})$. However, these only generate the diagonal terms of the Green's function, which is a matrix for multi-component systems. The off-diagonal terms such as $G_{\alpha\alpha'}(i\omega, \mathbf{k})$ is also indispensable to finding the topological invariant. To get those terms, one may apply an impulsive pulse right before the photoemission/photoabsorption process to induce a basis rotation between different spin components [25, 184]. The rotation should preserve the atomic momentum but mix their spins. For instance, one may apply a $\pi/2$-pulse coupling the spin $|\alpha\rangle$ and $|\alpha'\rangle$ to measure the spectral function $A_+(\omega, \mathbf{k})$ associated with the state $|+\rangle = (|\alpha\rangle + |\alpha'\rangle)/\sqrt{2}$ and a phase-shifted $\pi/2$-pulse to measure $A_I(\omega, \mathbf{k})$ associated with the state $|I\rangle = (|\alpha\rangle - i|\alpha'\rangle)/\sqrt{2}$. After measuring A_α, $A_{\alpha'}$, A_+ and A_I, the non-diagonal term $G_{\alpha\alpha'}$ can be found as (see Appendix D)

$$G_{\alpha\alpha'} = \frac{1}{2}[2G_{++} - G_{\alpha\alpha} - G_{\alpha'\alpha'} + i(2G_{\mathrm{II}} - G_{\alpha\alpha} - G_{\alpha'\alpha'})], \tag{6.3.5}$$

where $G_{\tau\tau}$ is obtained from $A_\tau(\omega, \mathbf{k})$ ($\tau = \alpha,\ \alpha',\ +$, or I) with Eq. (6.3.3).

6.3.2 A 1D example

The above scheme represents a general recipe to measure the topological invariant of strongly interacting cold-atomic systems. It is applicable to topological phases in one, two, or three dimensions, with or without symmetries. In 3D, measurement of the spectral function is somewhat trickier. In order to obtain $A(\omega, \mathbf{k})$ in 3D momentum space, one may map out 2D time-of-flight images measuring $A(\omega, k_x, k_y, k_{z_i})$ with different k_{z_i} layers, similar to the 3D atomic density measurement

introduced in Ref. [25]. Although we focused on interacting systems, this method naturally works for noninteracting systems as well. In the noninteracting limit, the zero-frequency Green's function gives a complete tomography of the free Hamiltonian in the momentum space, as explicitly manifested in the definition of *topological Hamiltonian*.

For actual measurement, one needs to discretize the frequency and the momentum. Hence, only a 'pixelized' version of $A(\omega,\mathbf{k})$ can be observed. In a typical setup, there also exists a harmonic confining potential to trap the atomic gas. To show that the scheme is feasible and robust to these experimental imperfections, in the following we apply it to a 1D interacting TI model and simulate the experiment numerically.

A 1D example.—Let us consider a 1D interacting TI model described by the Hamiltonian

$$\begin{aligned} H = &-t\sum_i \left(c^\dagger_{i,\uparrow}c_{i+1,\downarrow}+h.c.\right) \\ &+U\sum_i \left(\hat{n}_{i,\uparrow}-\frac{1}{2}\right)\left(\hat{n}_{i,\downarrow}-\frac{1}{2}\right), \end{aligned} \tag{6.3.6}$$

where t is the hopping strength and U characterizes the on-site interaction; $c^\dagger_{i,\sigma}$ ($c_{i,\sigma}$) is the creation (annihilation) operator of the fermionic atom with spin $\sigma=\{\uparrow,\downarrow\}$ at site i; $\hat{n}_{i,\sigma}=c^\dagger_{i,\sigma}c_{i,\sigma}$ is the number operator. With the generator $\hat{\Sigma}=\Pi_j[c^\dagger_{i,\uparrow}+(-1)^j c_{j,\uparrow}][c^\dagger_{i,\downarrow}+(-1)^j c_{j,\downarrow}]$, it can be explicitly checked that $\hat{\Sigma}H^*\hat{\Sigma}^\dagger=H$, indicating the Hamiltonian H is chirally symmetric [174]. For a Hamiltonian with chiral symmetry, the corresponding Green's function $G(i\omega,\mathbf{k})$ satisfies the condition $\mathscr{U}G(i\omega,\mathbf{k})\mathscr{U}=-G(-i\omega,\mathbf{k})$, where $\mathscr{U}$ is a unitary matrix whose square is the identity matrix [174, 177]. In our case, $\mathscr{U}$ can be chosen as $\mathscr{U}=\begin{pmatrix}1 & 0\\ 0 & -1\end{pmatrix}$ in a basis where $G(i\omega,\mathbf{k})$ has a off-diagonal structure [177]. In the noninteracting limit $U=0$, the model is equivalent to the well-known Su-Schrieffer-Heeger model [143], which belongs to the BDI symmetry class with a

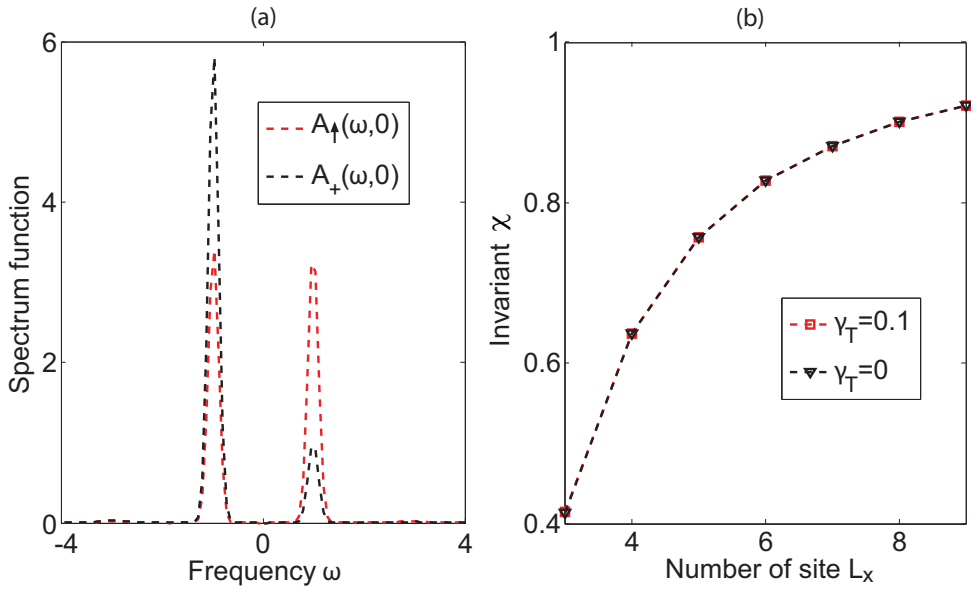

Figure 6.3.1: Numerically simulated results. (a) spectral functions at zero momentum with a trapping potential $\gamma_T = 0.1t$. The number of lattice sites is $L_x = 8$, and interaction strength $U = 0.8t$. (b) The topological invariant χ for different lattice sizes with and without the trapping potential. Here, $U = 0.8t$ and $t = 1$ is set to be the energy unit (Appendix D).

Z topological classification [19, 20]. For a 1D interacting system with chiral symmetry, the characteristic topological invariant can be expressed as [174, 177]

$$\chi = \frac{1}{4\pi i}\int dk\, \mathrm{Tr}[\mathscr{U} G^{-1}(0,k)\partial_k G(0,k)], \tag{6.3.7}$$

where the trace is taken over the matrix index of G.

The Hamiltonian in Eq. (6.3.6) may possibly be realized with cold fermionic atoms in a 1D optical lattice. The spin-flipping hopping terms can be implemented by Raman-assisted tunneling [24] and the interaction strength can be tuned by Feshbach resonances [104]. Here, we focus on the detection of the topological invariant, assuming the Hamiltonian is realized and the system is prepared in its ground state. We consider a finite-size lattice with periodic boundary conditions and apply

the proposed scheme to measure the spectral functions and extract the invariant χ. To simulate the experiment, we add to H a harmonic trapping potential $V_{\text{trap}} = \frac{1}{2}m\kappa^2 \sum_{i,\sigma} d_i^2 c_{i,\sigma}^\dagger c_{i,\sigma}$, where κ is the trapping frequency, m is the mass of the atom and d_i is the distance from the center of the trap to the lattice site i. We use $\gamma_T = m\kappa^2 a^2/2$ to parametrize the relative strength of the trap with a denoting the lattice constant. Exact diagonalization method is used to numerically diagonalize the Hamiltonian and find the spectral functions. Fig. 6.3.1(a) shows the spectral functions $A_\uparrow$ and A_+, which correspond to states $|\uparrow\rangle$ and $|+\rangle = (|\uparrow\rangle + |\downarrow\rangle)/\sqrt{2}$ respectively, at zero momentum. The extracted topological invariant χ is shown in Fig. 6.3.1(b) for different lattice sizes with and without the trapping potential. We observe that the trapping potential has only a minimal effect and the topological invariant converges quickly to the expected value $\chi = 1$ as the lattice size increases. Moreover, χ is also very robust to the coarse discretization of frequency and momentum. In our simulation, a 20×9 pixelization of (ω, k) yields $\chi = 0.92$, which deviates only about 8% from the expected value. In a typical experiment with a few hundred or thousand lattice sites, we expect the extracted topological invariant to be very much quantized with reasonably coarse resolution. Finally, the finite-temperature effect should be negligible due to a large gap (roughly about $2t$) in the Hamiltonian.

6.4 Discussion and summary

To sum up, we have introduced two general methods to measure the topological invariants in optical lattices. For topological band insulators, we have introduced a general experimental method to directly measure the band topology with ultracold atoms in an optical lattice. Our method is robust to realistic experimental imperfections, and is remarkably efficient in the sense that a small number of BZ pixelization is needed to produce accurate topological invariants. This scheme is applicable

not only to the examples discussed above, but also to other exotic phases such as the Hopf insulators or the SSH model. It can also be used to probe the nontrivial topology for each single band. This work thus provides a novel and simple detection method, and we hope it can be used to simplify existing schemes, and be applied to probe many interesting topological phases of matter.

For strongly interacting topological insulators, we have proposed a very general and robust scheme to detect topological phases for cold atomic systems with strong interactions. Our method requires only standard cold-atomic technologies and can be readily implemented in current experiments.

It is important to point out here that although the proposed scheme is very general, it is not universal. For interacting systems with nontrivial ground state degeneracies, such as fractional quantum hall liquids, the Green's function expressions of the topological invariants are not directly applicable [169, 185]. Recently, certain topological invariants, which generalize the twisted-boundary approach [168] and applicable to the degenerate cases, have been proposed [185]. However, they are apparently very hard to be experimentally extracted. We leave this important question for future studies.

CHAPTER VII

Knots and links in Hopf insulators

7.1 Introduction

Knots and links are fascinating and intricate topological objects that have played a prominent role in physical and life sciences. Their influence spans from DNA and molecular chemistry to vortices in superfluid helium, defects in liquid crystals and cosmic strings in the early universe. Here, we show that knotted structures also exist in a peculiar class of three dimensional topological insulators—the Hopf insulators. In particular, we demonstrate that the spin textures of Hopf insulators in momentum space are twisted in a nontrivial way, which implies various knot and link structures. We further illustrate that the knots and nontrivial spin textures can be probed via standard time-of-flight images in cold atoms as preimage contours of spin orientations in stereographic coordinates. The extracted Hopf invariants, knots, and links are validated to be robust to typical experimental imperfections. Our work establishes the existence of knotted structures in cold atoms and may have potential applications in spintronics and quantum information processings.

More than a century ago, Lord Kelvin propounded his celebrated "vortex atom" theory, which

proposed that atoms are made of vortex knots in the aether [186]. Knot theory has since become a central subject in topology and began to undertake important roles in diverse fields of sciences. Biologists discovered that molecular knots and links in DNA are crucial in vital processes of replication, transcription and recombination [187, 188]. In supramolecular chemistry, complex knotted structures have been demonstrated in the laboratory [189–191] and were shown to be essential for the crystallization and rheological properties of polymers [192]. In physics, knot has become a ubiquitous concept, making inroads into many subfields, such as classical field theory [193], helium superfluid [194], fluid mechanics and plasma [195], spinor Bose-Einstein condensates [196], chiral nematic colloids [197–199], quantum chromodynamics [200] and string theory [201]. More recently, exciting progresses are made in laboratories. Experimental creation of knotted configurations has been demonstrated in liquid crystal [202–205], laser light [206] and fluid flows [207,208], driving a new wave of intense interest in the study of knots.

Meanwhile, topology also came into play in physics through another route in recent years. A special class of materials, dubbed as topological insulators and superconductors, is theoretically predicted and experimentally observed [7–9]. In general, they are topological phases that are protected by system symmetries, which cannot be smoothly connected to the trivial phase if the respective symmetries are preserved [17]. For these materials, the nontriviality originates from the interplay between symmetry and topology. Many interesting and exotic physical phenomena are predicted, including, but not limited to, quantized Hall conductance [122], robust chiral edge states [7], image magnetic monopole [209], wormhole [210] and Witten [211] effects. It would be natural to ask whether knots play a role in these topologically nontrivial materials. Here, we explore this idea and demonstrate that intriguing knot and link structures hide in a class of topological insulators.

More specifically, we show that a kaleidoscope of knot and link structures is encoded in the spin

texture of Hopf insulators, which are a class of topological insulators in three dimensions (3D) [23,41]. In momentum space, these spin textures represent a special realization of the long-sought-after Hopfions [193,212], which are 3D topological solitons evading any experimental observation so far. Although a solid-state realization of Hopf insulators seems extremely challenging, it is not quixotic to foresee a cold-atomic implementation in optical lattices in the near future, amid rapid development of synthetic gauge fields in cold atoms [72,88,89,126,213]. Driving by this promising vista, we further propose here a scheme to measure the Hopf topology and visualize different knots and links based on current cold-atom technologies. We demonstrate how to extract the Hopf invariant and the knotted spin textures from the state-of-the-art time-of-flight imaging data. The corresponding knots and links are explicitly revealed as preimage contours of the observed spin orientations via a stereographic coordinate system. The extracted information—Hopf invariants, knots, and links—are robust against typical experimental imperfections. This work opens a new avenue not only for the studies of topological insulators, but also for the integration of perplexing knot theory into experimental science.

7.2 Knots and links in Hopf insulators

Hopf insulators are 3D topological insulators characterized by an integer Hopf index and have topologically protected metallic surface states [23, 41]. Unlike the recently predicted [11, 36, 40] and experimentally observed 3D $\mathbb{Z}_2$ topological insulators [16, 33], Hopf insulators do not require any symmetries (other than charge conservation). They are peculiar exceptions that sit outside of the periodic table for topological insulators and superconductors [19,20]. One may regard them as 3D generalization of the 2D quantum anomalous Hall effect [131]. A model Hamiltonian for the Hopf insulator with Hopf invariant $\chi = \pm 1$ was first introduced by Moore, Ran and Wen [41]. In

our previous works [22, 23], we generalized their results and constructed Hamiltonians for Hopf insulators with arbitrary Hopf index, using two different approaches, one based on the quaternion algebra [22] and the other based on the generalized Hopf map [23] $f:\ \mathbb{S}^3 \to \mathbb{S}^2$ (up to irrelevant overall normalizations)

$$S_x + iS_y = 2\eta_\uparrow^p \bar{\eta}_\downarrow^q,\ S_z = (|\eta_\uparrow|^{2p} - |\eta_\downarrow|^{2q}), \tag{7.2.1}$$

where the coordinates $\boldsymbol{\eta} = (\mathrm{Re}[\eta_\uparrow], \mathrm{Im}[\eta_\uparrow], \mathrm{Re}[\eta_\downarrow], \mathrm{Im}[\eta_\downarrow])$ are mapped to (S_x, S_y, S_z), and p, q are integers prime to each other. The Hopf invariant for the map is known to be $\chi(f) = \pm pq$ with the sign determined by the orientation of the three-sphere [81]. To relate to the Hamiltonian, $\boldsymbol{\eta}$ can in turn be considered as another map from the first Brillouin zone (BZ) to three-sphere, $g:\ \mathbb{T}^3 \to \mathbb{S}^3$

$$\begin{aligned} \eta_\uparrow(\mathbf{k}) &= \sin k_x + i \sin k_y \\ \eta_\downarrow(\mathbf{k}) &= \sin k_z + i(\cos k_x + \cos k_y + \cos k_z + h). \end{aligned} \tag{7.2.2}$$

Thus, the map $\mathbf{S}(\mathbf{k}) = (S_x(\mathbf{k}), S_y(\mathbf{k}), S_z(\mathbf{k}))$ can be regarded as a composition of two maps, $\mathbf{S} = f \circ g$. The Hamiltonian can be subsequently constructed in momentum space as $H = \sum_{\mathbf{k}} \psi_{\mathbf{k}}^\dagger \mathscr{H}(\mathbf{k}) \psi_{\mathbf{k}}$ with $\psi_{\mathbf{k}}^\dagger = (c_{\mathbf{k}\uparrow}^\dagger, c_{\mathbf{k}\downarrow}^\dagger)$ and

$$\mathscr{H}(\mathbf{k}) = \mathbf{S}(\mathbf{k}) \cdot \boldsymbol{\sigma}, \tag{7.2.3}$$

where $c_{\mathbf{k}\uparrow}^\dagger, c_{\mathbf{k}\downarrow}^\dagger$ are fermionic creation operators and $\boldsymbol{\sigma} = (\sigma^x, \sigma^y, \sigma^z)$ are three Pauli matrices. The Hamiltonian $\mathscr{H}(\mathbf{k})$ contains $(p+q)$th order polynomials of $\sin(\mathbf{k})$ and $\cos(\mathbf{k})$, which correspond to $(p+q)$th neighbor hoppings in real space.

To study the topological properties of the Hamiltonian in Eq. (7.2.3), we define a normalized (pseudo-) spin field $\hat{\mathbf{S}}(\mathbf{k}) = \mathbf{S}(\mathbf{k})/|\mathbf{S}(\mathbf{k})|$ (the normalization does not affect the topological prop-

erties). Hopf invariant, also known as Hopf charge or Hopf index, can be computed as an integral [23, 41]:

$$\chi(\hat{\mathbf{S}}) = -\int_{\mathrm{BZ}} \mathbf{F}\cdot\mathbf{A}\, d^3\mathbf{k}, \tag{7.2.4}$$

where $\mathbf{F}$ is the Berry curvature defined as $F_\mu = \frac{1}{8\pi}\varepsilon_{\mu\nu\tau}\hat{\mathbf{S}}\cdot(\partial_\nu\hat{\mathbf{S}}\times\partial_\tau\hat{\mathbf{S}})$ and $\mathbf{A}$ is the associated Berry connection satisfying $\nabla\times\mathbf{A}=\mathbf{F}$. Direct calculations give $\chi(\hat{\mathbf{S}}) = \pm pq$ if $1<|h|<3$, $\chi(\hat{\mathbf{S}}) = \pm 2pq$ if $|h|<1$, and $\chi(\hat{\mathbf{S}}) = 0$ otherwise [23]. This can be understood intuitively by decomposing the composition map, $\chi(\hat{\mathbf{S}}) = \chi(f)\Lambda(g) = \pm pq\Lambda(g)$, where the map g is classified by another topological invariant

$$\Lambda(g) = \frac{1}{12\pi^2}\int_{\mathrm{BZ}} d\mathbf{k}\varepsilon_{\mu\nu\rho\tau}\frac{\varepsilon_{\alpha\beta\gamma}}{|\boldsymbol{\eta}|^4}\eta_\mu\partial_\alpha\eta_\nu\partial_\beta\eta_\rho\partial_\gamma\eta_\tau. \tag{7.2.5}$$

With g given by Eq. (7.2.2), one obtains $\Lambda(g)=1$ if $1<|h|<3$, $\Lambda(g)=-2$ if $|h|<1$, and $\Lambda(g)=0$ otherwise. Geometrically, $\Lambda(g)$ counts how many times $\mathbb{T}^3$ wraps around $\mathbb{S}^3$ under the map g, and $\chi(f)$ describes how many times $\mathbb{S}^3$ wraps around $\mathbb{S}^2$ under f. Their composition gives the Hopf invariant $\chi(\hat{\mathbf{S}})$ [23].

The spin field $\hat{\mathbf{S}}$ can be viewed as a map from $\mathbb{T}^3$ to $\mathbb{S}^2$. While the domain $\mathbb{T}^3$ is three-dimensional, the target space $\mathbb{S}^2$ is two-dimensional. As a consequence, the preimage of a point in $\mathbb{S}^2$ should be a closed loop in $\mathbb{T}^3$, and the linking number of two such loops corresponds to the Hopf invariant $\chi(\hat{\mathbf{S}})$. Similarly, the linking number of two preimage loops in $\mathbb{S}^3$ under the map f gives the Hopf invariant $\chi(f)$, which is part of $\chi(\hat{\mathbf{S}})$. For easy visualization of knots and links, we work with $\mathbb{S}^3$ rather than $\mathbb{T}^3$ and probe the Hopf index $\chi(f)$. Fig. 7.1.1 shows several links and knots corresponding to certain spin orientations by using stereographic coordinates to represent $\mathbb{S}^3$ (See Appendix E). It is clear from the figure that the linking number of two preimage contours of distinct spin orientations is equal to the Hopf invariant $\chi(f)$. More interestingly, we note that even a single

preimage contour may form a highly nontrivial knot when p and q become large. For instance, the trefoil knot and the Solomon seal knot plotted in Fig. 7.1.1**e** and Fig. 7.1.1**f** are two well-known nontrivial knots with nonunit knot polynomials [214]. More complex knots and links emerge for larger p and q.

A nonvanishing value of $\chi(\hat{\mathbf{S}})$ also indicates that the spin field $\hat{\mathbf{S}}$ has a nontrivial texture that cannot be continuously deformed into a trivial one. Mathematically, the Hopf invariant in Eq. (7.2.4) is a characteristic topological invariant of a sphere fiber bundle and a nonvanishing χ generally precludes the existence of a global section due to the obstruction theory, just like nonzero Chern numbers forbid the tangent bundle of a two-sphere to have a global section [97]. A physical interpretation is that one can never untwist $\hat{\mathbf{S}}$ smoothly unless a topological phase transition is crossed. In Fig. 7.2.1, the simplest nontrivial spin texture corresponding to $\chi(f) = 1$ is sketched. One may regard $\hat{\mathbf{S}}$ as a unit continuous vector field. In the stereographic coordinates, $\hat{\mathbf{S}}$ resembles a nontrivial solution to the Faddeev-Skyrme model [212] with Hopf charge one. In this sense, $\hat{\mathbf{S}}$ is a special realization of Hopfions, which are 3D topological solitons with broad applications but has hitherto escaped experimental observations [215]. In the next section, we will show that all these nontrivial knots, links, and spin textures can be measured in cold atom experiments with standard time-of-flight images.

7.3 Probe knots, links and Hopf invariants

Hopf insulators are special topological insulators that have not been seen in solid systems. Although some magnetic compounds such as $R_2Mo_2O_7$, with R being a rare earth ion, are proposed to be possible candidates [41], actual realization of the Hopf insulator phase in solid remains very

h	Size	Periodic	Open	Trap	Pert.+Trap
0	10^3	-2.058	-1.956	-1.985	-1.986
0	20^3	-2.019	-2.019	-2.025	-2.025
2	10^3	1.041	0.982	0.986	0.986
2	20^3	1.012	1.008	1.009	1.009
4	20^3	-9.6×10^{-5}	2.9×10^{-5}	6.6×10^{-5}	6.7×10^{-5}

Table 7.5: **Hopf index extracted from time-of-flight images.** Simulated experimental results for Hopf invariants with different lattice sizes and varying h. Four different situations, one with periodic and three with open boundary conditions, are considered. The Hopf index can be found from the momentum density distributions obtained directly through time-of-flight images. The parameters used are $p = q = 1$ and $\gamma_t = \gamma_r = 0.1$.

challenging due to the complicated spin-orbit couplings. The rapid experimental advancements in synthetic spin-orbit couplings with cold atoms [72, 88, 89, 126, 213] provide a new promising platform to simulate various topological phases. Actually, some model Hamiltonians, which are initially proposed mainly for theoretical studies and thought to be out of reach for experimentalists due to their unusual and complex couplings, have indeed been realized in cold atom labs. For instance, an experimental observation of the topological Haldane model with ultracold atoms has been achieved recently [162]. It is probable that Hopf insulators will also attain a cold atom experimental realization in the near future. With this in mind, we illustrate below how to detect the Hopf invariant and probe the knot structure with ultracold atoms in optical lattices. In ref [25], we introduced a generic method to directly measure various topological invariants based on time-of-flight imaging of cold atoms. This method is applicable to detection of topological band insulators in any spatial dimensions. Here we apply it to the detection of Hopf insulators in cold-atom systems.

From Eq. (7.2.4), to extract the Hopf invariant, it is essential to obtain the spin texture $\hat{\mathbf{S}}(\mathbf{k})$ in momentum space. In experiment, one discretizes the BZ and a pixelized version of $\hat{\mathbf{S}}(\mathbf{k})$ can be obtained through time-of-flight imaging. Refs [25, 142] describe in detail how to measure $\hat{\mathbf{S}}(\mathbf{k})$ in experiment. One astute observation [142] was that the spin component is related to the density

distributions as $\hat{S}_z(\mathbf{k}) = [n_\uparrow(\mathbf{k}) - n_\downarrow(\mathbf{k})]/[n_\uparrow(\mathbf{k}) + n_\downarrow(\mathbf{k})]$. A fast Raman or radio frequency pulse during time-of-flight rotates the atomic states and maps $\hat{S}_x$ and $\hat{S}_y$ to $\hat{S}_z$, enabling one to reconstruct the whole pixelized $\hat{\mathbf{S}}(\mathbf{k})$. To obtain the 3D momentum distributions, one may map out the 2D densities $n(k_x, k_y, k_{z_i})$ with various k_{z_i} layers [25]. It is encouraging to see in Table D.1 that ten or twenty layers are sufficient to produce very good results.

With the measured $\hat{\mathbf{S}}(\mathbf{k})$ in hand, we can extract the Hopf index directly. As $F_\mu = \frac{1}{8\pi}\varepsilon_{\mu\nu\tau}\hat{\mathbf{S}} \cdot (\partial_\nu \hat{\mathbf{S}} \times \partial_\tau \hat{\mathbf{S}})$, we obtain the Berry curvature $\mathbf{F}$ at each pixel of the BZ. We then find the Berry connection by solving a discrete version of the equation $\nabla \times \mathbf{A} = \mathbf{F}$ in the Coulomb gauge $\nabla \cdot \mathbf{A} = 0$. Hopf index can thus be extracted from Eq. (7.2.4), replacing the integral by a discrete summation. To simulate real experiments, we write down the Hamiltonian H in real space and consider a finite-size lattice with open boundaries. In addition, we add two terms into the Hamiltonian to account for typical experimental imperfections. The first one is a global harmonic trap parametrized by γ_t, and the second one is a random noise characterized by γ_r (see Appendix E). For the simplest case of $p = q = 1$, we numerically diagonalize the realistic real-space Hamiltonian and compute the corresponding Hopf index for different h based on the method introduced in ref [25]. Our results are summarized in Table D.1. We can see that the Hopf index converges rapidly to the expected value as the lattice size increases and the detection method remains robust against typical experimental imperfections.

As discussed in the previous section, a nonvanishing $\chi(\hat{\mathbf{S}})$ implies a nontrivial spin texture. With cold atoms, one can actually visualize this nontrivial spin texture in the momentum space. In Fig. 7.3.1**a**, we plot a slice of the observed $\hat{\mathbf{S}}(\mathbf{k})$ with $k_z = 0$. Although this 2D plot cannot display full information of the 3D spin texture, its twisted spin orientations do offer a glimpse of the whole nontrivial structure. It is worthwhile to note that this texture is distinct from typical 2D skyrmion [216] configurations, where swirling structure is a prominent feature [217, 218]. More

slices can be mapped out from the experiment to look for traits of a Hopfion. With $\hat{\mathbf{S}}(\mathbf{k})$, one may also explicitly see knots and links in experiment. In the ideal case and continuum limit, the preimages of two different orientations of $\hat{\mathbf{S}}(\mathbf{k})$ should be linked with a linking number equal to the Hopf index. Hence, if we map out these preimages, we would obtain a link. However, a real experiment always involves various kinds of noises. As a result, the measured $\hat{\mathbf{S}}(\mathbf{k})$ cannot be perfectly accurate. Moreover, due to finite size, the observed $\hat{\mathbf{S}}(\mathbf{k})$ is discrete and only has finite resolution. To circumvent these difficulties, we keep track of the preimages of a small neigborhood of the chosen orientations (see Appendix E). We plotted a Hopf link in Fig. 7.3.1**b** based on the numerically simulated experimental results. From this figure and many other numerical simulations (not shown here for conciseness), we find, as expected, that this link is stable against experimental imperfections. Varying h and other parameters characterizing the strength of noise changes the shape of each circle, but the linked structure persists with linking number one.

7.4 Realization of Hopf insulators with cold atoms

In the previous section, we discussed how to measure the Hopf invariant and probe knots and links. Let us now focus on a possible experimental scheme to realize Hopf insulators with ultracold atoms. The method used here is similar to that in Ref [24], where a cold-atom implementation of 3D chiral topological insulators was proposed. We consider cold fermionic atoms (^{6}Li for example) in a 3D cubic optical lattice and choose two internal atomic levels as our spin states $|\uparrow\rangle$ and $|\downarrow\rangle$. Other levels are initially depopulated by the optical pumping and transitions to those levels are forbidden due to a large energy detuning or carefully selected laser polarizations. In real space, the Hamiltonian (7.2.3) with $p = q = 1$ and $h = 0$ has spin-orbit coupled hoppings along nine

possible directions. Here, we explicitly demonstrate how to realize the specific hoppings along the $\mathbf{v} = \hat{x} + \hat{y}$ direction. For other directions, the realization scheme will be similar and thus omitted for conciseness. The hopping terms in the $\mathbf{v}$ direction can be written as

$$H_{\mathbf{v}} = \frac{1}{2}\sum_{\mathbf{r}}[-(1+i)c^{\dagger}_{\mathbf{r},\downarrow} - c^{\dagger}_{\mathbf{r},\uparrow}]c_{\mathbf{r}+\mathbf{v},\uparrow} + [(1-i)c^{\dagger}_{\mathbf{r},\uparrow} + c^{\dagger}_{\mathbf{r},\downarrow}]c_{\mathbf{r}+\mathbf{v},\downarrow} + \text{h.c.} \tag{7.4.1}$$

Apparently, $H_{\mathbf{v}}$ consists of various hopping terms coupled with spin rotations. Basically, both spin $|\uparrow\rangle$ and $|\downarrow\rangle$ hop along the $-\mathbf{v}$ direction to become a superposition of both spin states. We can decompose the four different hopping terms and each of them can be achieved via Raman-assisted tunneling [101–103]. For instance, the first two hoppings can be activated by two Raman pairs, $\Omega_{\uparrow}$, $\widetilde{\Omega}_{1\mathbf{v}}$, and $\Omega_{\uparrow}$, $\Omega_{1\mathbf{v}}$, where $\Omega_{\uparrow}$ is in common; $\widetilde{\Omega}_{1\mathbf{v}}$ and $\Omega_{1\mathbf{v}}$ can be drawn from the same beam split by an electric or acoustic optical modulator. The phase and strength of the hopping can be controlled by the laser phase and intensity (see caption of Fig. 7.4.1). Similarly, the other two hopping terms can be triggered by the Raman triplet $\widetilde{\Omega}_{2\mathbf{v}}$, $\Omega_{2\mathbf{v}}$ and $\Omega_{\downarrow}$ as shown in Fig. 7.4.1.

One may notice that the parity (left-right) symmetry is explicitly broken here and natural hoppings are suppressed. Both of these can be achieved by a homogeneous energy gradient along the $\mathbf{v}$ direction, which can be accomplished, for instance, by the magnetic field gradient, dc- or ac-Stark shift gradient, or the natural gravitational field [24, 102, 103]. We denote the linear energy shift per site in the $\mathbf{v}$ direction by $\Delta_{\mathbf{v}}$ and impose that natural tunneling rate $t_0 \ll \Delta_{\mathbf{v}}$. As a consequence, the natural tunneling probability $(t_0/\Delta_{\mathbf{v}})^2$ is negligible in this tilted lattice. The large energy offset also forbids Raman-assisted tunnelings in the opposite direction other than the ones prescribed above. One subtle point we need to be careful with is that the large detuning δ_1 and δ_2 for the two Raman triplets should be different, so that no unintended interference between these two triplets happens.

7.5 Discussion and summary

Hopf insulators are a special class of topological insulators beyond the periodic table for topological insulators and superconductors [19, 20]. Their physical realization is of great importance but undoubtedly challenging. With ultracold atoms in optical lattice, Hopf insulators can be realized using the Raman-assisted hopping technique [101, 102, 219]. The basic idea is the same as in Ref. [24], where an cold atom implementation of 3D chiral topological insulators are proposed. Here we want to focus on how to measure the Hopf invariant and probe various intriguing knots and links, and leave the detailed implementation protocols for future works. Other simpler experimental scenario for realizing Hopf insulators with cold atoms might also exist. A promising alternative is to consider periodically driven quantum systems, where modulation schemes can be tailored to implement diverse gauge fields [220] and experimental realization of the Haldane model has been reported recently [162].

There are many other interesting topics that deserve further investigations. For instance, in the above discussions, we showed that many different kinds of knots and links are hidden in Hopf insulators. However, a complete list of such knots and links is still lacking. Moreover, a deeper understanding of the interplay between knot theory and topological insulators is in demand as well. From Fig. 7.1.1, it seems that partial information of certain spin orientations is already sufficient to characterize the topology of the Hopf insulators. This observation may help simplify the experimental detections. Take the case in Fig. 7.1.1**e** as an example, to determine whether the system has a nontrivial topology or not, we only have to do the time-of-flight in the $\hat{S}_y$ (or equivalently $\hat{S}_z$) basis. Thus, no rotation induced by fast Raman or radio frequency pulses is

needed. In the future, it will also be important to explore potential applications of the knotted spin texture in designing topological-state-based spin devices, which may advance future spintronic technologies and quantum information processings [221].

In summary, we have shown that many interesting knot and link structures are hidden in Hopf insulators. We also demonstrated, via numerical simulation, that these exotic knots and nontrivial spin textures can be probed through time-of-flight images in cold atoms. In addition, we validated the robustness of the observed Hopf invariants, knots and links against typical experimental imperfections. Our results shed fresh light on the studies of topological insulators and put forward a new platform to experimentally probe fascinating knots and links, protected by topology.

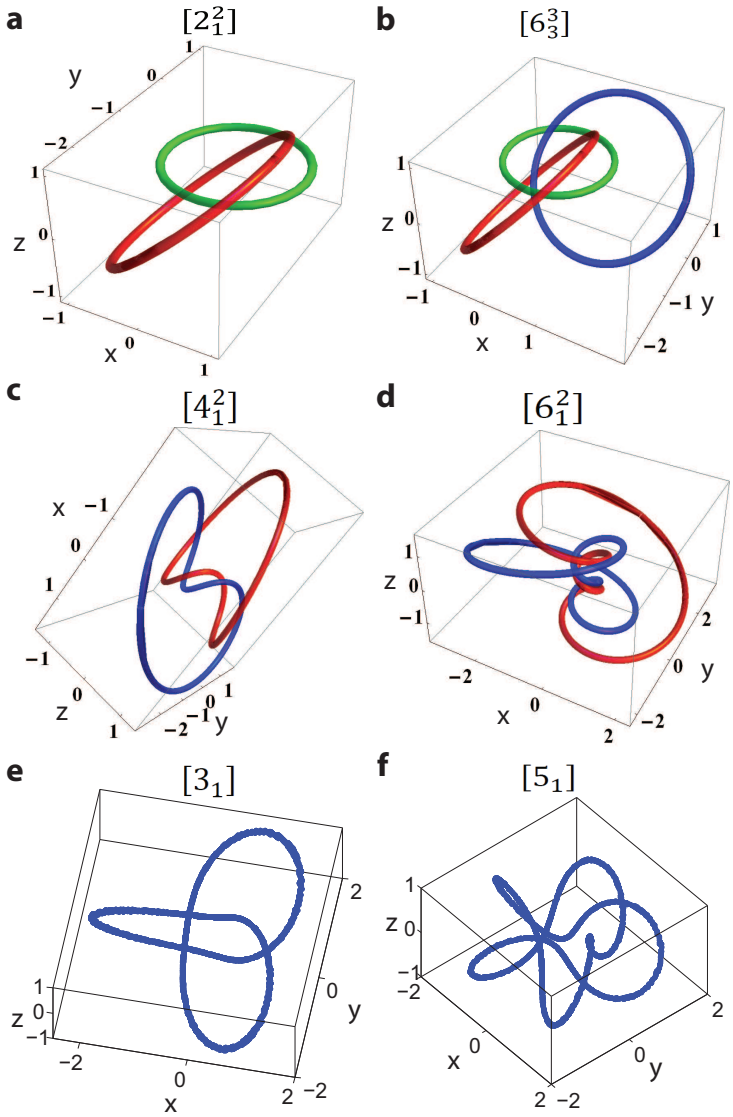

Figure 7.1.1: **Knots and links hidden in Hopf insulators.** These knots and links correspond to preimages of three different spin orientations $\hat{\mathbf{S}}_1 = (1,0,0)$, $\hat{\mathbf{S}}_2 = (0,1,0)$ and $\hat{\mathbf{S}}_3 = (0,0,1)$ living on $\mathbb{S}^2$. The loops in red (blue, green) are preimages of $\hat{\mathbf{S}}_1$ ($\hat{\mathbf{S}}_2$, $\hat{\mathbf{S}}_3$) obtained from the contour plot $f^{-1}(\hat{\mathbf{S}}_1)$ $\left(f^{-1}(\hat{\mathbf{S}}_2), f^{-1}(\hat{\mathbf{S}}_3)\right)$ in a stereographic coordinate system (see Appendix E). The symbols inside each square bracket denote the standard Alexander–Briggs notation for the corresponding knot (link). The four links are: (**a**) the Hopf link, (**b**) the 6_3^3 link, (**c**) the Solomon's link, and (**d**) the 6_1^2 link. The two knots are: (**e**) the trefoil knot and (**f**) the Solomon seal knot. The parameters are chosen as: $p = q = 1$ in (**a**) and (**b**); $p = 1$, $q = 2$ in (**c**); $p = 1$, $q = 3$ in (**d**); $p = 3$, $q = 2$ in (**e**) and $p = 5$, $q = 2$ in (**f**). $h = 2$ for (**a**-**f**). From (**a**-**d**), it is evident that the linking number of two different preimage contours is equal to the Hopf invariant $\chi(f)$.

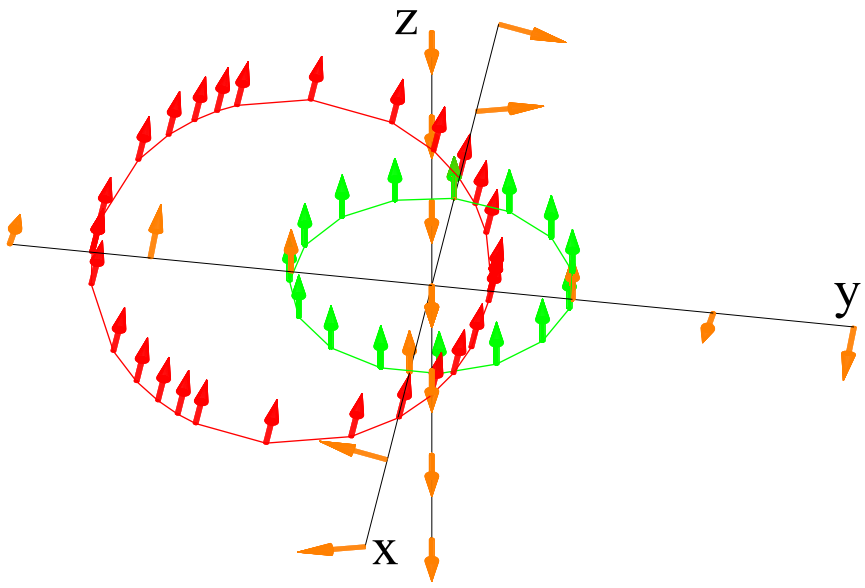

Figure 7.2.1: **Knotted spin texture in stereographic coordinates.** We sketch out the spin orientations along each axis and on two circles. The parameters are chosen as $p = q = 1$ and $h = 2$. Spins reside on the red (green) circle point to the x (z) direction and those on the z axis all point to the south. Also, all spins faraway from the origin asymptotically point to the south. This spin texture is nontrivial (twisted with $\chi(f) = 1$) and cannot be untwined continuously unless a topological phase transition is crossed.

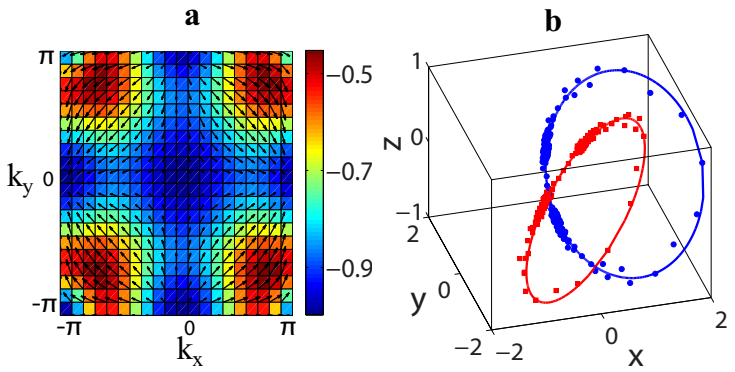

Figure 7.3.1: **Spin texture and Hopf link.** (**a**) Simulated spin texture in the k_x-k_y plane with $k_z = 0$. The background color scale shows the magnitude of out-of-plane component $\hat{S}_z$, and the arrows show the magnitude and direction of spins in the k_x-k_y plane. (**b**) Simulated Hopf link with linking number one. The red (blue) circle represents the theoretical preimage of $\hat{\mathbf{S}}_1$ ($\hat{\mathbf{S}}_2$) and the scattered red squares (blue dots) are numerically simulated preimage of the ε-neighborhood of $\hat{\mathbf{S}}_1$ ($\hat{\mathbf{S}}_2$) (see Appendix E), which can be observed from time-of-flight images. The spin texture and preimages are computed by exactly diagonalizing the real space Hamiltonian with lattice size $40 \times 40 \times 40$ under an open boundary condition. The parameters are chosen as $p = q = 1$, $h = 2$, $\gamma_t = 0.01$, $\gamma_r = 0$ and $\varepsilon = 0.15$.

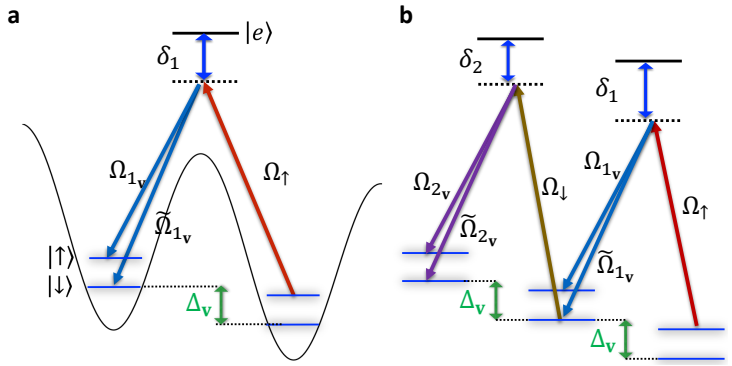

Figure 7.4.1: **Laser configurations.** Schematics of the laser configuration to realize the Hamiltonian $H_{\mathbf{v}}$. (**a**) A linear tilt $\Delta_{\mathbf{v}}$ per site along the $\mathbf{v}$ direction is imposed. A Raman triplet with detunings matching the frequency offset can induce spin-flip hoppings in a desired direction. (**b**) Two Raman triplets that realize all hoppings in $H_{\mathbf{v}}$. δ_1 and δ_2 are two different large detunings from the excited states. The Rabi frequencies for each beam in terms of the unit Ω_0 are: $\widetilde{\Omega}_{1\mathbf{v}} = -\sqrt{2}\Omega_0 e^{i\pi/4} e^{-ikx}$, $\Omega_{1\mathbf{v}} = -\Omega_0 e^{-ikx}$, $\Omega_\uparrow = \Omega_0 e^{iky}$, $\widetilde{\Omega}_{2\mathbf{v}} = \sqrt{2}\Omega_0 e^{-i\pi/4} e^{-ikx}$, $\Omega_{2\mathbf{v}} = \Omega_0 e^{-ikx}$, and $\Omega_\downarrow = \Omega_0 e^{iky}$, where k is the magnitude of the laser wave vector. All these Raman beams can be draw from a single laser through an electric or acoustic optical modulator.

CHAPTER VIII

Majorana fermions

8.1 Introduction

Besides the conventional bosons and fermions, in synthetic two-dimensional (2D) materials there could exist more exotic quasi-particles with non-abelian statistics, meaning that the quantum states in the system will be transformed by non-commuting unitary operators when we adiabatically braid the particles one around another. The search for such non-abelian particles is of critical significance in the current investigation on quantum physics. Despite the recent great progress, it remains technically elusive to braid the quasi-particles in materials to verify their conjectured non-abelian statistics. Here, we propose an experimental scheme to observe non-abelian statistics with cold atoms in a 2D optical lattice. We show that the Majorana-Schockley modes associated with line defects can be braided with non-abelian statistics through adiabatic shift of the local potentials. Observation of the non-abelian statistics is of both fundamental interest and practical importance, in particular for topological quantum computation.

Majorana fermions are exotic particles which, unlike electrons and positrons, constitute their own

antiparticles [222] and exhibit non-abelian statistics [223]. They are important not only because of their fundamental role in condensed matter [7, 8, 223] and high energy physics [222, 224], but also because of their promising practical applications in topological quantum information processing tasks, such as the synthesis of a fault-tolerant quantum computer [57, 69] or a certifiable random number generator [27]. However, in spite of extensive exciting progresses [43, 225–230], the unambiguous detection of Majorana fermions and the probe of their non-abelian statistical properties remain one of the foremost ongoing goals in current physics.

Laser controlled cold atoms provide a powerful experimental platform to realize exotic states of matter [72, 88, 231]. Several proposals have been made to observe non-abelian statistics based on control of vortex states in a $p+ip$ superfluid [129, 232, 233]. A vortex in a $p+ip$ superfluid of odd vorticity traps a zero energy mode corresponding to a Majorana fermion. The Majorana fermions in different vortices are found to obey non-abelian statistics [71, 234, 235]. An intriguing proposal has been made to braid the vortex Majorana fermions in a cold atomic gas by a focused laser beam [129, 233]. An experimental implementation of this proposal, however, is still challenging for several reasons: first, besides the Majorana mode a vortex also traps a number of other in-gap states [233]. The small energy difference between these states and the zero energy Majorana mode sets a tough requirement for the relevant energy and time scales. Second, moving the vortex by a focused laser beam may change its trapped modes, and a quantitative understanding of this process is still lacking. Finally, a natural way to realize the $p+ip$ superfluid is based on the p-wave Feshbach resonance [236], but the latter is difficult to stabilize in free space [237, 238]. Very recently, another nice idea has been suggested to braid Majorana modes associated with dislocations in an optical lattice [239]. Insertion of dislocations requires a change of structure of the optical lattice, which is experimentally challenging and yet to be demonstrated.

In this chapter, we propose an experimental scheme to observe non-abelian statistics with cold

atoms in an optical lattice in a vortex-free configuration. A p-wave superfluid based on the Feshbach resonance could be stabilized in an optical lattice due to the quantum Zeno effect [238, 240]. The recent remarkable experimental advance has allowed single-site addressing in a two-dimensional (2D) optical lattice [156–159, 241]. With this capability, we can create a line defect in a 2D lattice simply by shifting the chemical potential along the line. Different from dislocations, this line defect requires no structure change of the underlying optical lattice and is ready to be implemented in current experiments [156–159, 241]. Recently, it was found that a pair of zero-energy modes shall emerge at the edges of this line defect [242] by the Shockley mechanism [243]. The exchange statistics of these modes, however, remains unresolved [242]. Motivated by recent works on braiding of nanowires [244], here we utilize exact numerical methods to demonstrate that the Majorana-Shockley modes associated with these line defects in a 2D superfluid obey non-abelian statistics and their braiding can be achieved by tuning of only the local chemical potential. This tuning is significantly simpler compared with the braiding of nanowires [244] or dislocations [239], which requires site-by-site tuning of the pairing interaction and the tunneling rates [244, 245]. We also demonstrate robustness of the braiding operation against practical noise and propose a scheme to measure the topological qubits using local measurement of the atom number. The proposed scheme fits well with the state-of-the-art of the experimental technology in a 2D optical lattice [156–159, 241].

8.2 Majorana fermions in optical lattices

8.2.1 System and Hamiltonian

We consider cold atoms in a 2D optical lattice, which are prepared into the $p+ip$ superfluid phase. This superfluid phase can be achieved, for instance, through the p-wave Feshbach resonance [236]. The instability associated with the p-wave Feshbach resonance in free space [237] could be overcome in an optical lattice through the quantum Zeno effect [238]. Alternatively, an effective $p+ip$ superfluid phase for cold atoms can also be achieved by a combination of the s-wave Feshbach resonance and the light induced spin-orbital coupling [37, 129, 246].

In the momentum $\mathbf{k}$ space, the Bogoliubov-de Gennes (BdG) Hamiltonian describing the $p+ip$ superfluid phase on a square optical lattice has the form $H=\sum_{\mathbf{k}}\psi_{\mathbf{k}}^{\dagger}\mathscr{H}(\mathbf{k})\psi_{\mathbf{k}}$, with $\psi_{\mathbf{k}}^{\dagger}=(c_{\mathbf{k}}^{\dagger},c_{-\mathbf{k}})$ and

$$\mathscr{H}(\mathbf{k})=d_x(\mathbf{k})\sigma^x+d_y(\mathbf{k})\sigma^y+d_z(\mathbf{k})\sigma^z, \tag{8.2.1}$$

where $d_x(\mathbf{k})=\Delta\sin k_x a$, $d_y(\mathbf{k})=\Delta\sin k_y a$, $d_z(\mathbf{k})=\mu-J(\cos k_x a+\cos k_y a)$, $\sigma^{x,y,z}$ denote the Pauli matrices, a is the lattice constant, μ is the chemical potential, J is the neighboring hopping rate, and Δ is the pairing strength. The topological property of this Hamiltonian is characterized by the first Chern number $C_1=-\frac{1}{2\pi}\int_{\mathrm{BZ}}dk_xdk_yF_{xy}(\mathbf{k})$ with the Berry curvature $F_{xy}(\mathbf{k})=\partial_{k_x}A_y(\mathbf{k})-\partial_{k_y}A_x(\mathbf{k})$ and the Berry connection $A_\nu(\mathbf{k})=\langle u_-(\mathbf{k})|i\partial_{k_\nu}|u_-(\mathbf{k})\rangle$ ($\nu=x,y$), where $|u_-(\mathbf{k})\rangle$ denotes the lower band Bloch eigenstate of $\mathscr{H}(\mathbf{k})$ and the integration in C_1 is over the first Brillouin zone (BZ). The phase of the Hamiltonian H is topologically nontrivial with $C_1=\mathrm{sign}(\mu)$ in the parameter regime $0<|\mu|<2J$ (taking Δ as the energy unit) and topologically trivial with $C_1=0$ when $|\mu|>2J$. A topological phase transition occurs at $|\mu|=2J$.

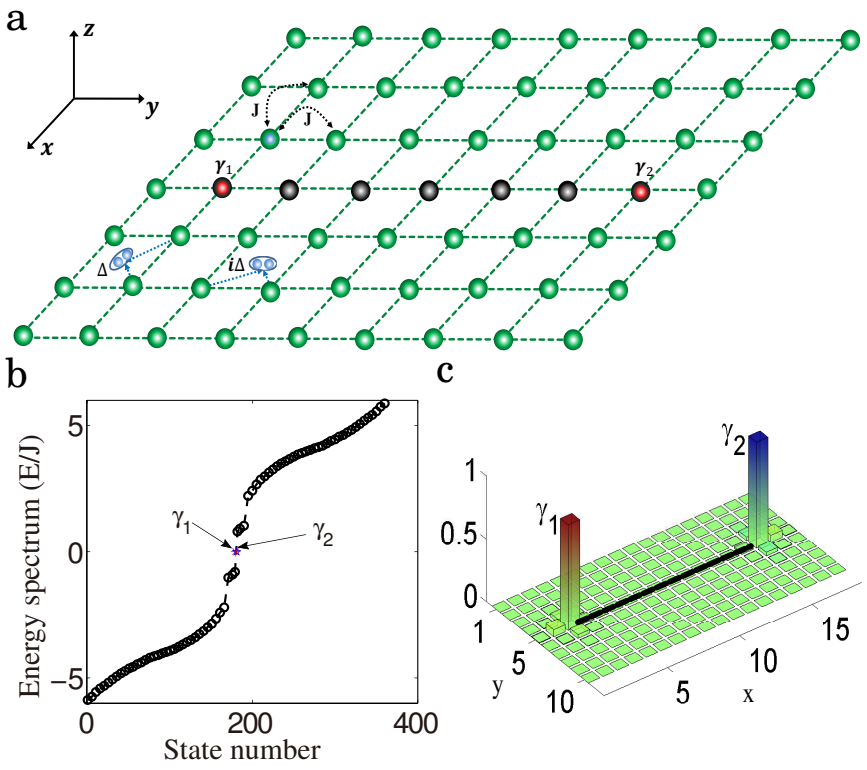

Figure 8.2.1: **Creation and manipulation of the MSFs in an optical lattice.** (**a**) Cold fermionic atoms are loaded into a 2D optical lattice. J and Δ denote the nearest neighbor hopping rate and pairing strength. A line defect with different local chemical potential binds two zero-energy MSFs γ_1 and γ_2 (red circles) at its edges. (**b**) Energy spectrum of the Hamiltonian H on a square lattice of size $18a \times 10a$ with open boundaries. The length of the line defect is $14a$. The zero-energy MSFs have tiny energy splitting due to the small size of the line defect, which is numerically found to be $< 10^{-10}J$ for our parameters. (**c**) The amplitude of the mode function for γ_1 and γ_2. The black line indicates the line defect with chemical potential μ_d. The parameters are chosen as $\Delta = J$, $\mu_0 = 10J$, and $\mu_d = 0.1J$.

8.2.2 Creation and braiding of MSFs

With single-site addressing, the potential shift of each lattice site can be individually adjusted in experiments [156–159, 241]. We create a line defect in a 2D optical lattice by tuning the chemical potential μ_d along a chain of atoms to make it different from that of the background lattice (denoted by μ_0) so that they reside in topologically distinct phases (illustrated in Fig. 1a). For a certain range of μ_d that depends on μ_0, a pair of zero energy Majorana-Shockley fermion (MSF) modes appear at the two edges of the line defect [242]. We choose μ_0 in the topologically trivial phase with $\mu_0 > 2J$ so that there are no other zero-energy modes on the boundary of the finite 2D lattice.

Under a typical size of the 2D optical lattice with a line defect, we solve exactly the eigenmodes of the Hamiltonian (1) under open boundary conditions, and the eigen-spectrum is shown in Fig. 8.2.1b (see Appendix F). Clearly, there are a pair of zero-energy MSF modes that are separated from other defect modes and bulk states by a minimum gap about J. The MSFs are described by anti-commuting real fermion operators γ_j with $\gamma_j = \gamma_j^\dagger$ and $\gamma_j\gamma_k + \gamma_k\gamma_j = 2\delta_{jk}$. A pair of MSF modes γ_1 and γ_2 together represents a conventional fermion mode $c_m = (\gamma_1 + i\gamma_2)/2$, with the eigenstates of $c_m^\dagger c_m = \frac{1}{2}(i\gamma_1\gamma_2 + 1)$ encoding a topological qubit. The eigen-functions of the MSF modes γ_1 and γ_2 are shown in Fig. 1c, which are well localized at the edges of the line defect.

8.2.3 Proof of non-Abelian statistics

To examine the exchange statistic of the MSF modes, we adiabatically deform the line defect with steps shown in Fig. 2(a-f). Each step is achieved through site-by-site tuning of the chemical potential from μ_d to μ_0 (to shorten the line defect) or from μ_0 to μ_d (to extend the line defect). We simulate the time evolution of the MSF modes in the Heisenberg picture. Under the adiabatic evolution, the Hamiltonian always remains gapped at any time as shown in Fig. 2g, which protects the MSF

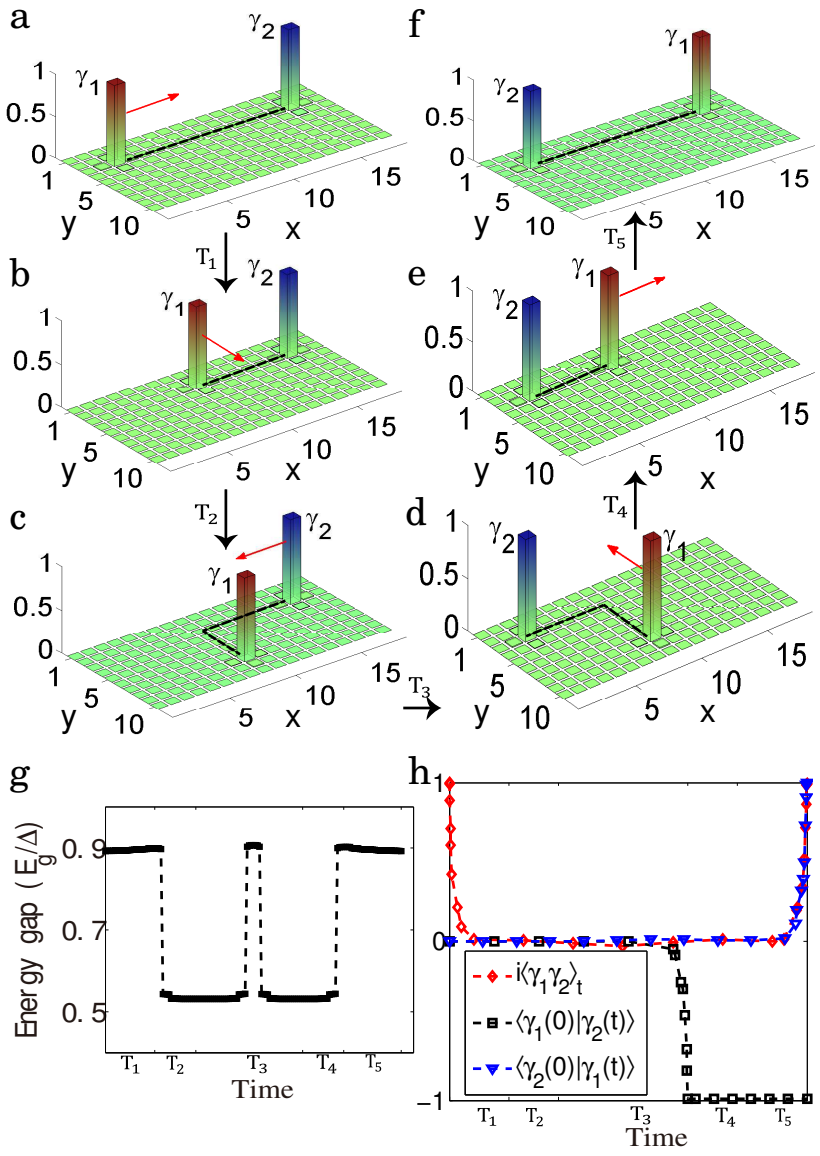

Figure 8.2.2: **Braiding of two MSFs bound to the same line defect.** (**a**) The black line indicates the line defect with chemical potential μ_d. Sequentially tuning the local chemical potentials at one end from μ_d to μ_0 shortens the line defect and transports γ_1 along the x direction. The red arrow shows the moving direction of the MSF. Similar operations along a T-junction path realize adiabatic exchange of γ_1 and γ_2, with steps illustrated in (**a**)-(**f**). (**g**) The evolution of the energy gap E_g throughout the braiding process. The system is always gapped with the minimum gap $E_g > 0.5J$. (**h**) Time evolution of the MSF modes γ_1, γ_2 and their correlations. All the parameters are the same as in Fig. 8.2.1.

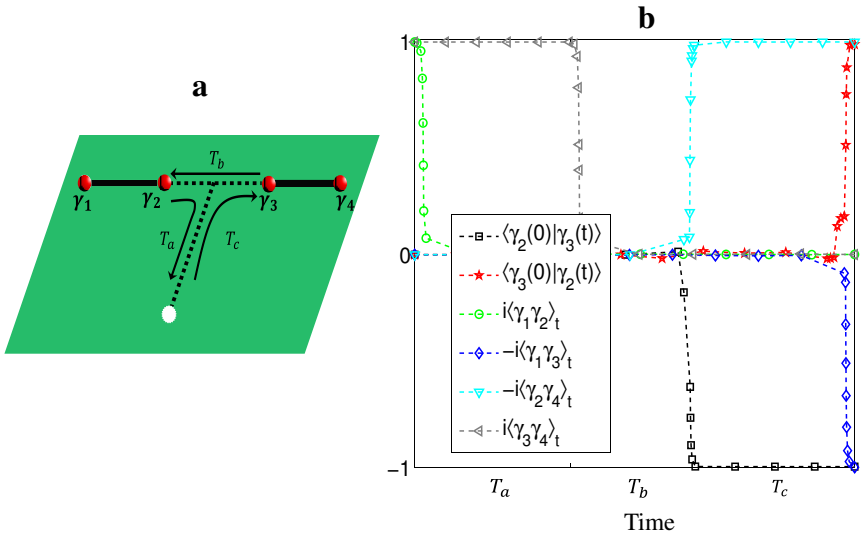

Figure 8.2.3: **Braiding of two MSFs bound to different line defects.** (**a**) Illustration of braiding two MSFs from different line defects along the T-junction path. (**b**) Time evolution of the MSF modes $\gamma_1, \gamma_2, \gamma_3, \gamma_4$ and their correlations. The MSFs γ_2 and γ_3 are braided. The parameters are taken as: the lattice size $12a \times 28a$, two horizontal line defects each of length $8a$ and distance $9a$, $\Delta = 0.91J$, $\mu_0 = 10\Delta$ and $\mu_d = 0.1\Delta$.

modes from mixing with other modes. The evolution of the MSF modes γ_1 and γ_2 and their correlation are shown in Fig. 2h. After the whole evolution with time T, apparently we have $\gamma_1(T) = \gamma_2(0)$ and $\gamma_2(T) = -\gamma_1(0)$. The correlation $\langle\gamma_1(T)\gamma_2(T)\rangle = -\langle\gamma_2(0)\gamma_1(0)\rangle = \langle\gamma_1(0)\gamma_2(0)\rangle$.

This transformation of the MSF modes occurs in a similar way when we adiabatically braid the edges associated with different line defects. In Fig. 3a, we illustrate the adiabatic braiding of two edge modes γ_2 and γ_3 of different line defects along a T-junction path. This braiding involves joining and cutting of two line defects and we need to choose parameters appropriately to avoid appearance of accidental near-zero-energy modes. In general, the four zero-energy MSF modes are still well protected by a significant energy gap. Their evolution and the associated correlations are shown in Fig. 3b. The results indicate that $\gamma_2(T) = \gamma_3(0)$ and $\gamma_3(T) = -\gamma_2(0)$ for the two braided modes. The other modes remain unchanged with $\gamma_1(T) = \gamma_1(0)$ and $\gamma_4(T) = \gamma_4(0)$.

The above transformation rule generalizes straightforwardly to the case of $2N$ MSF modes. The rule is exactly the same as the case of Majorana fermions bound to vortices [234]. For $2N$ modes γ_j ($j = 1, 2, \cdots, 2N$), when we braid γ_j and γ_{j+1}, the transformation is described by a unitary operator $U_j = e^{\pi\gamma_{j+1}\gamma_j/4}$ which transforms $\gamma_j \to \gamma_{j+1}, \gamma_{j+1} \to -\gamma_j$. As U_j and U_{j+1} do not commute, the exchange statistics of the MSF modes is non-abelian and belongs to the so-called Ising anyon class according to the classification of non-abelian anyons [247].

8.2.4 Robustness to realistic imperfections

The unitary operation U_j from topological braiding of the MSF modes is robust against noise and experimental imperfections. To verify that, we examine several sources of noise typical for atomic experiments: First, with imperfect single-site addressing, when we tune the chemical potential of one site, we may change the potentials of the neighboring sites as well, modeled by a spreading ratio of $1-\alpha$. Second, there is a global weak harmonic trap for cold atom experiments, with an additional trapping potential $V_{\text{trap}} = \frac{V_{\text{T}}}{2(L_x^2+L_y^2)} \sum_{\mathbf{r}} d_{\mathbf{r}}^2 c_{\mathbf{r}}^\dagger c_{\mathbf{r}}$, where L_x (L_y) is the lattice dimension along the x (y) direction, and $d_{\mathbf{r}}$ is the distance from the trap center. Typically, V_{T} ranges from $0.1J$ to J. Finally, there is unavoidable small disorder potential in experiments which adds random fluctuations to the chemical potential with magnitude denoted by λ_R. We recalculate the evolution of the MSF modes and their correlations, incorporating contribution of all these sources of noise. The results are shown in Fig. 4, which are almost indistinguishable from the corresponding results shown in Fig. 2h under the ideal case. This demonstrates the robustness of the braiding operations of the MSFs.

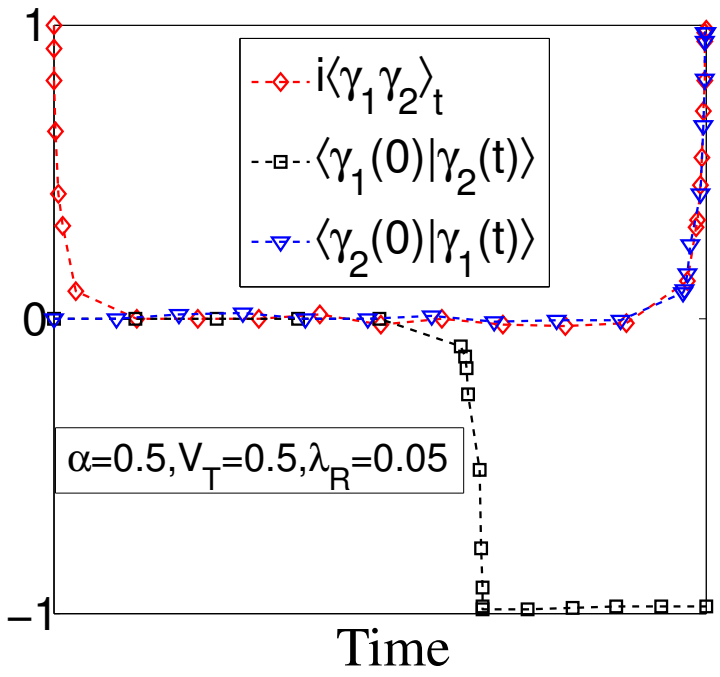

Figure 8.2.4: **Robustness to experimental noise and imperfections.** The lattice size is $20a \times 12a$ and other parameters are the same as in Fig. 8.2.1. α, V_T, λ_R denote the parameters characterizing respectively the laser beam crosstalk, the strength of the global harmonic trap, and the magnitude of random fluctuation of the chemical potential (see the main text).

8.2.5 Detection

To verify the non-abelian braiding operations, we need to detect the topological qubit encoded by two nonlocal MSF modes γ_1 and γ_2. For the 1D nanowire, the parity of the total particle number is a conserved property, which is different for the two eigenstates of $i\gamma_1\gamma_2$ and thus can be used to detect the topological qubit [244, 245]. For our case, the line defect interacts with the background lattice with tunneling and pairing terms which in general do not conserve the parity of the total atom number along the line, therefore the parity detection does not work. We propose a different method to detect the topological qubit. The line defect is adiabatically shortened until it finally reduces to a single lattice site $\mathbf{r}_0$ (illustrated in Fig. 5a) and we examine evolution of the MSF modes γ_1 and γ_2 during this process. As shown in Fig. 5b, with a high fidelity (about 99%), the mode γ_1 (γ_2) is mapped to $\gamma_{\mathbf{r}_0,A} = c^\dagger_{\mathbf{r}_0} + c_{\mathbf{r}_0}$ ($\gamma_{\mathbf{r}_0,B} = i(c^\dagger_{\mathbf{r}_0} - c_{\mathbf{r}_0})$), respectively. By a measurement of the local atom number $c^\dagger_{\mathbf{r}_0}c_{\mathbf{r}_0}$ after the adiabatic merging, we thus measure the topological operator $i\gamma_1\gamma_2$ with a high fidelity (about 98%). This local measurement is actually more robust compared with the nonlocal parity detection. Note that the detection fidelity of the topological qubit in principle can be improved to an arbitrary accuracy by using the quantum non-demolition (QND) technique: to measure the topological qubit $i\gamma_1\gamma_2$, we create an ancillary topological qubit (with MSF modes γ_3 and γ_4), perform an effective Controlled-NOT gate between the topological qubits $i\gamma_1\gamma_2$ and $i\gamma_3\gamma_4$ through the noise-resilient braiding operations [27], and then measure the ancilla $i\gamma_3\gamma_4$ by the above method. As the qubit $i\gamma_1\gamma_2$ is not destroyed by the measurement, it can be repeatedly measured through this QND technique and the detection error is exponentially suppressed with increase of the detection rounds.

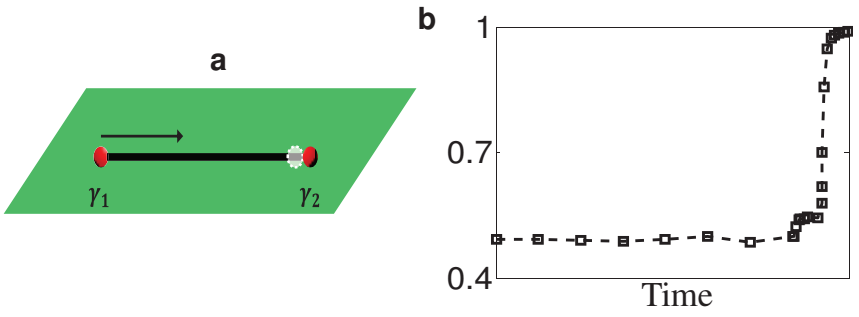

Figure 8.2.5: **Detection of the topological qubit.** (**a**) Two MSFs γ_1 and γ_2 are fused through adiabatic shortening of the line defect to a single lattice site $\mathbf{r}_0$. (**b**) Transformation of the MSF modes γ_1 and γ_2 under adiabatic merging. For simplicity, we plot evolution of the magnitude of the mode overlap between $c_{\mathbf{r}_0}$ and $[\gamma_1(t)+i\gamma_2(t)]/2$. At the end of merging, γ_1 and γ_2 are mapped dominantly to the local modes $c^\dagger_{\mathbf{r}_0}+c_{\mathbf{r}_0}$ and $i(c^\dagger_{\mathbf{r}_0}-c_{\mathbf{r}_0})$, respectively, which enables detection of the initial nonlocal topological qubit by a simple measurement of the atom number $c^\dagger_{\mathbf{r}_0}c_{\mathbf{r}_0}$ on a single lattice site after the adiabatic merging. All the parameters are the same as in Fig. 8.2.1.

8.3 Discussion and summary

Our analysis is based on a concrete BdG Hamiltonian describing 2D $p+ip$ superconductors in the symmetry class D of the periodic table of topological insulators and superconductors, which lacks time-reversal symmetry. Ultracold atoms in optical lattices are capable of implementing more exotic topological phases that might harbor Majorana fermions. In the future, it might be interesting to explore whether MSFs exist as well in other symmetry classes and study their experimental realizations with cold atoms. In particular, one possible direction is to study MSFs in the DIII class, which has time-reversal symmetry and a Z_2 topological classification. As a consequence, Majoranas in this class should come in pairs at each end of the line defect due to Kramers's theorem and the braiding operations should always exchange two pairs of Majoranas. Whereas the non-abelian statistics of Majorana Kramers's doublets in 1D DIII-class superconductor was theoretically demonstrated recently [248], the 2D case remains unexplored. Another important direction is to study the Shockley mechanism in 3D topological superconductors in symmetry class

DIII and CI. In 3D, both DIII and CI class superconductors have time-reversal symmetry and a Z classification. This study might lead to a promising experimental realization of 3D non-abelian statistics as introduced by Teo and Kane [249].

In summary, we have proposed a complete scheme to observe non-abelian statistics of the MSFs associated with line defects in a 2D optical lattice. The MSFs are created, braided, and fused all through adiabatic tuning of the chemical potential for certain lattice sites. The detection of the topological qubit is transformed to local measurement of the atom number on a single lattice site. The required technology fits well with the current status of the optical lattice experiments [156–159, 241]. Through numerical simulation, we have demonstrated robustness of the non-abelian braiding operations under a typical experimental configuration with imperfections. The scheme provides a viable approach for observation of the exotic non-abelian braiding statistics, which is a goal of intense interest and a critical step for realization of robust topological quantum information processing [27, 57, 69].

CHAPTER IX

Majorana random number generators

9.1 Introduction

Majorana fermions are exotic particles which, unlike electrons and positrons, constitute their own antiparticles [222, 250]. Their theoretical discovery by Ettore Majorana in 1937 has tremendously impacted various subfields of physics, ranging from fractional quantum Hall effect [223], and topological insulators and superconductors [7, 8] in condensed matter physics to neutrino and dark matter problems in high energy physics [222]. Here we propose a new promising application of Majorana fermions in constructing a cryptographically secure quantum random number generator. Unlike their possible application in topological quantum computation [57, 69, 251], where a noisy $\pi/8$-phase gate or certain dynamical topology-changing operations are indispensable [57], we show that braiding operations combined with quantum demolition measurements are more than enough for our purpose. Thus, our scheme works in a fully fault-tolerant way and is more experimentally feasible. Our results not only open a door to new applications of topologically ordered phase of matter, but also shed fresh light on the design of a new type of random number generator

that may have high research and commercial values.

The complex-valued solutions to the celebrated Dirac equation predicted that every elementary particle should have a complex conjugate counterpart, namely an antiparticle. For example, an electron has a positron as its antiparticle. However, in 1937 Ettore Majorana [250] showed that the complex Dirac equation can be modified to permit real wavefunctions, leading to the possible existence of the so called "*Majorana fermions*" (MF) which are their own antiparticles. In condensed matter physics, Majorana fermions might appear as elementary qusiparticle excitations. To witness Majorana fermions unambiguously, numerous proposals have been made in recent years, these including $\nu = 5/2$ fractional quantum Hall systems [57, 223], hybrid topological insulator (TI)—superconductor (SC) systems [37], interacting quantum spins [251], chiral p-wave superconductors [71], strong spin-orbit coupled semiconductor thin film [246] or quantum nanowire [252, 253] in the proximity of an external s-wave superconductor. Based on these promising proposals, experimentalists also have made great progress recently. For instance, in Ref. [254], Wang *et al* reported an experimental observation of the coexistence of the superconducting gap and topological surface states in the surface of Bi_2Se_3 thin films. This laid the groundwork for experimental realization of Majorana fermions as the zero-energy core states in the TI/SC heterostructure [37]. More recently, signatures of Majorana fermions in hybrid superconductor-semiconductor nanowire devices have been reported as well [43].

As more and more experimental signatures of Majorana fermions are reported, a natural question arises and becomes increasingly pressing: *what can we do with Majorana fermions?* One remarkable application might be found in topological quantum computation, where the non-Abelian statistical property of Majorana fermions is ingeniously explored to process quantum information in a fault-tolerant way [57, 251]. Nevertheless, Majorana fermions are not capable of universal quantum computation, i.e., the transformations generated by braiding operations are not sufficient

to implement all possible unitary transformations [57]. To obtain a universal gate set, a single-qubit $\pi/8$ phase gate is needed. Although there are several proposals to implement the $\pi/8$ gate either by some noise nontopological operations or by certain dynamical topology-changing operations [57, 255], the required complicated physical manipulations of the systems are far beyond current technologies. Here, we introduce another distinct application of Majorana fermions in designing a new type of random number generator.

Random numbers have been used for thousands of years and have tremendous applications today [256–258]. Examples include numerical simulations of physical and biological systems, cryptography, and quantum key distribution [259], etc. Yet, the generation of true random numbers is still a challenging task [260]. In principle, true random numbers can never be generated by a classical device because any classical system admits a deterministic description. Quantum theory is, on the other hand, intrinsically random. Hence, it is natural to think about quantum random number generators [261–264] (QRNGs), which explore the intrinsic random property of quantum mechanics to generate random numbers. However, the random numbers generated by these QRNGs still cannot be unequivocally certified or quantified since in any real experiment the intrinsic randomness of these QRNGs would inevitably be mixed-up with an apparent randomness due to noise or lack of control of the experiment [260]. This will greatly jeopardize the applications of randomness, especially cryptographic applications. A breakthrough made recently is to generate certified private randomness by using the nonlocal correlations of certain entangled quantum states [260, 265]. In Ref. [260], Pironio *et al* explored this idea in detail [260] and reported an experimental realization based on the Clauser-Horn- Shimony-Holt (CHSH) inequality [266].

Nevertheless, for typical quantum systems, entanglement is difficult to obtain and is very fragile due to decoherence. Take the trapped ion system in Ref. [260] for example; the heralded entanglement of two ions is established through interference and coincidence detection of two emitted

photons, whose polarization is entangled with each ion. This scheme of generating entanglement is not very efficient (about 1 entanglement event every 8 minutes) and the fidelity of the entangled state is low (about 81%) due to spontaneous decay of the ions and many other factors [267]. As a result, a QRNG based on this system may be degraded because of these drawbacks. Another consideration might be the photonic system. Yet, for this system, current experiments also suffer greatly from the so called “detection-efficiency loophole". To get out of this dilemma, we show here that Majorana fermion system is an ideal system to build a cryptographically secure QRNG. It is ideal in the sense that it would be decoherence and loophole free in principle. The logical qubits are encoded in Majorana fermions and the unitary gate operations are implemented by braidings and quantum demolition measurements. Furthermore, our protocol only involves three logical qubits. Thus the stringent scalability requirement in topological quantum computation is released.

9.2 Self-test random number generators

9.2.1 Certified randomness via MABK inequality

The implementation of certification of a quantum random number generator with Majorana fermions is tricky. First of all, one can not use the Bell-CHSH inequality anymore as proposed in Ref. [260], since it is impossible to violate this inequality through topological manipulation of Majorana fermions alone [268]. In fact, to observe violations of the CHSH inequality, measurements in the non-Clifford bases are required. However, topological operations on Majorana fermions can only give gates in the Clifford group, and thus not able to achieve the measurements required for the CHSH inequality violation for randomness certification. Consequently, we have to consider certification of randomness based on extension of the Bell inequalities in the multi-qubit case. For

simplicity, here we use the MABK inequality for three logical qubits [269–271]. We show that first, this inequality can be used to certify randomness, and second, the inequality can be tested with topological manipulation of Majorana fermions alone. For the MABK inequality, we consider three qubits, each with two measurement settings. We denote the measurement settings for each qubit by the binary variables x, y, z, and the corresponding measurement outcomes by a, b, c, where $x,y,z,a,b,c = 0,1$. The MABK inequality can be rewritten as [269–271]

$$L \equiv \sum_{(x,y,z)\in\mathscr{S}} \tau(x,y,z)[P(\texttt{even}|xyz) - P(\texttt{odd}|xyz)] \leq 2, \tag{9.2.1}$$

where $\mathscr{S} = \{(0,0,0),(0,1,1),(1,0,1),(1,1,0)\}$ and $\tau(x,y,z)$ is a sign function defined by $\tau(x,y,z) = (-1)^{(x+y+z)/2}$; $P(\texttt{even}|xyz)$ ($P(\texttt{even}|xyz)$) is the probability that $a+b+c$ is an even (odd) number when settings (x,y,z) are chosen. The inequality (9.2.1) is satisfied by all local hidden variable models. However, in quantum mechanics certain measurements performed on entangled states can violate this inequality. Experimentally, we can repeat the experiment k times in succession to estimate the violation. For each trial, the measurement choices (x,y,z) are generated by an independent identical probability distribution $P(xyz)$. Denote the input string as $\mathscr{I} = (x_1,y_1,z_1;\cdots;x_k,y_k,z_k)$ and the corresponding output string as $\mathscr{O} = (a_1,b_1,c_1;\cdots;a_k,b_k,c_k)$. The estimated violation of the MABK inequality can be obtained from the observed data as

$$\hat{L} = \frac{1}{k} \sum_{(x,y,z)\in\mathscr{S}} \frac{\tau(x,y,z)}{P(xyz)} [N(\texttt{even}|xyz) - N(\texttt{odd}|xyz)], \tag{9.2.2}$$

where $N(\texttt{even}|xyz)$ ($N(\texttt{odd}|xyz)$) denotes the number of trials that we get an even (odd) outcome $a+b+c$ after k times of measurements with the measurement setting (x,y,z).

We need to show that the output string $\mathscr{O}$ from the measurement outcomes contains genuine

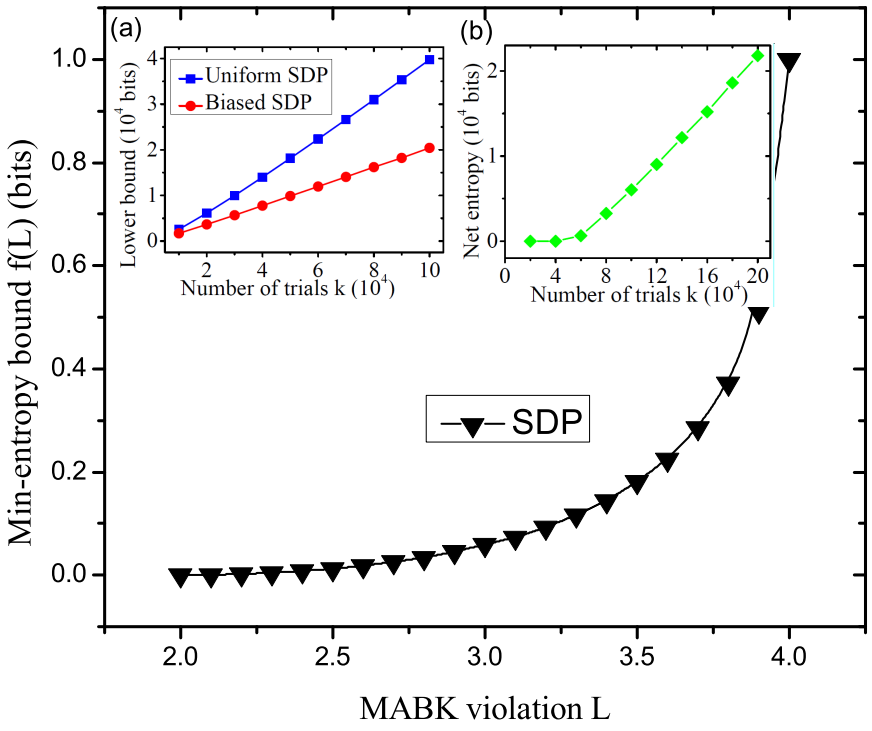

Figure 9.2.1: (Color online) Plot of the function $f(\hat{L})$ versus violation $\hat{L}$ of the MABK inequality. The function is calculated through optimization based on the semi-definite programming with the details shown in the Supplemental Material of Ref. [27]. The inset (a) shows the lower bound of the min-entropy $kf(\mathscr{L}_m - \varepsilon) - \log_2 \frac{1}{\delta}$ versus the number of trials k. Here we assume an observed MABK violation lies within the interval $3.9 = \mathscr{L}_m \leq \hat{L} < \mathscr{L}_{max} = 4$ with probability δ. The parameters are chosen as $\delta = 0.001$ and $\varepsilon' = 0.01$. The bound $kf(\mathscr{L}_m - \varepsilon)$ depends on the input probability distribution $P(xyz)$ through the parameter $r = \min_{xyz} P(xyz)$. The blue-square line represents the bound under a uniform distribution ($P(xyz) = 1/4$ for all $(x,y,z) \in \mathscr{S}$), while the red-dotted line shows the bound under a biased probability distribution with $P(011) = P(101) = P(110) = \alpha k^{-1/2}$ and $P(000) = 1 - 3\alpha k^{-1/2}$ with $\alpha = 10$. It consumes less randomness to generate a biased distribution for the input bits, so the net amount of randomness, defined as the number of output random bits minus that of the input, becomes positive when k is large (typically k needs to be of the order 10^5). The inset (b) plots the net amount of randomness generated after k trails under a biased distribution of the inputs. The parameters are the same as those in the inset (a).

randomness by proving that it has a nonzero entropy. Let $\{\mathscr{L}_m : 0 \leq m \leq m_{max}\}$ be a series of violation thresholds with $\mathscr{L}_0 = 2$ and $\mathscr{L}_{m_{max}} = 4$, corresponding respectively to the classical and quantum bound. Denote by $\mathscr{D}(m)$ the probability that the observed violation $\hat{L}$ lies in the interval $[\mathscr{L}_m, \mathscr{L}_{m+1})$. We can use the min-entropy to quantify randomness of the output string $\mathscr{O}$ [260, 272, 273]:

$$E_\infty(\mathscr{O}|\mathscr{I},\mathscr{E},m)_{\mathscr{D}} \equiv -\log_2 \sum_{\mathscr{I},\mathscr{E}} [\max_{\mathscr{O}} \mathscr{D}(\mathscr{O},\mathscr{I},\mathscr{E}|m)], \tag{9.2.3}$$

where $\mathscr{E}$ represents the knowledge that a possible adversary has on the state of the device and the maximum is taken over all possible values of the output string $\mathscr{O}$. The probability distribution $\mathscr{D}(\mathscr{O},\mathscr{I},\mathscr{E}|m)$ is defined in Ref. [27]. Based on a similar procedure as in Ref. [260], we can prove that if $\mathscr{D}(m) > \delta$, the min-entropy of the output string conditional on the input string and the adversary's information has a lower bound [27], given by

$$E_\infty(\mathscr{O}|\mathscr{I},\mathscr{E},m)_{\mathscr{D}} \geq kf(\mathscr{L}_m - \varepsilon) - \log_2(1/\delta), \tag{9.2.4}$$

where the parameter $\varepsilon \equiv \sqrt{-2(1+4r)^2(\ln \varepsilon'^2)}$ with $r = \min P(xyz)$, the smallest probability of the input pairs, and ε' is a given parameter that characterizes the closeness between the target distribution $\mathscr{D}(\mathscr{O},\mathscr{I},\mathscr{E})$ and the real distribution after k successive measurements (see the supplement for an explicit definition). The function $f(\hat{L})$ can be obtained through numerical calculation based on semi-definite programming (SDP) [274] and is shown in Fig. 9.2.1. The minimum-entropy bound $kf(\mathscr{L}_m - \varepsilon) - \log_2 \frac{1}{\delta}$ and the net entropy versus the number of trials k are plotted in the insets (a) and (b) of Fig. 9.2.1. Any observed quantum violation with $\hat{L} > 2$ leads to a positive lower bound of the min-entropy, and a positive mini-entropy guarantees that genuine random numbers can be extracted from the string $\mathscr{O}$ of the measurement outcomes through the standard protocol

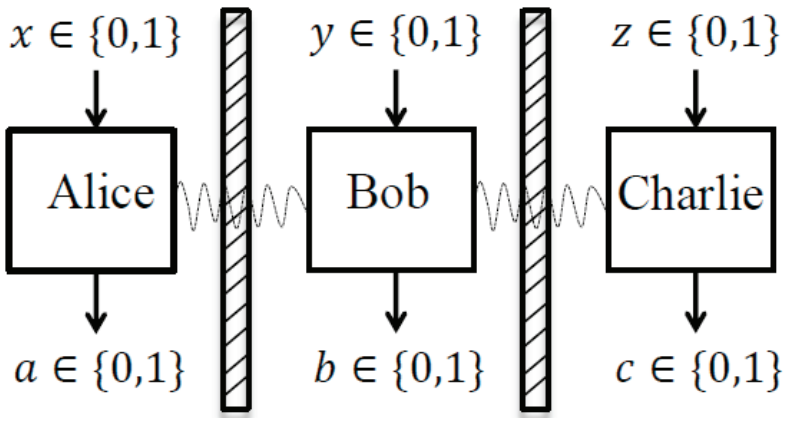

Figure 9.2.2: The GHZ game. Alice, Bob and Charlie are three collaborating but non-communicating parties. Each of them receives a single bit and outputs a single bit. The input (x,y,z) is chosen uniformly from $\{(0,0,0),(0,1,1),(1,0,1),(1,1,0)\}$. After receiving their bits, they produce output bits $a,b,c \in \{0,1\}$, respectively. No communication between them is allowed. If $a \oplus b \oplus c = x \vee y \vee z$, they win the game.

of random number extractors [275]. As some amount of randomness needs to be consumed to prepare the input string according to the probability distribution $P(xyz)$, the scheme here actually realizes a randomness expansion device [265, 272]. Similar to Ref. [272], we can show that under a biased distribution $P(xyz)$ as shown in Fig. 9.2.1 we generate a much longer random output string of length $O(k)$ from a relatively small amount of random seeds of length $O(\sqrt{k}\log_2\sqrt{k})$ when k is large.

9.2.2 Certifiable randomness with unconditional security

The above described random generation scheme is only secure to classical adversary. Recently, Miller and Shi have introduced a theoretical protocol to generate randomness secure even against quantum adversary [276, 277]. Based on their protocol, a random number generator can be constructed based on the GHZ game, as shown in Fig. 9.2.2. The complete protocol includes the

following steps:

Step 1: Let N be a positive integer (the length of the output string), $\eta \in (0,1]$ (the abort threshold) and $q \in (0,1/2]$ (the test frequency) be two reals.

Step 2: A bit $r \in \{0,1\}$ is chosen according to a biased $(1-q,q)$ distribution.

Step 3: If $r = 1$ ("game round"), an input string $xyz \in \{000,011,101,110\}$ is chosen randomly with an uniform probability distribution (each triplet of inputs has probability $1/4$). x (y,z) is then given to Alice (Bob,Charlie). Alice, Bob and Charlie do their measurements accordingly as specified in the GHZ game in Fig. 9.2.2. A "P" (pass) or a "F" (fail) is recorded according to whether they win or loss the game.

Step 4:If $r = 0$ ("generation round"), input $xyz = 00$ is given to Alice Bob and Charlie. Alice, Bob and Charlie do the measurement A_0, B_0 and C_0, respectively. A "H" (heads) or a "T" is recorded according to whether Alice's output is 0 or 1.

Step 5: Repeat $N-1$ more times of the steps 2-4.

Step 6: If the "failure" rate (out of all the game rounds) exceeds $1 - W_{\text{CHSH}} + \eta$ or more than $2qN$ game rounds have occurred, the protocol aborts. Otherwise, the protocol succeeds and $\{\text{P, F, H, T}\}^N$ represent our desired random output string.

9.2.3 Majorana fermion implementation

We now show how to generate and certify random numbers using Majorana fermions. The key step is to generate a three-qubit entangled state and find suitable measurements that lead to violation of the MABK inequality. Majorana fermions are non-Abelian anyons, and their braiding gives nontrivial quantum operations. However, this set of operations are very restricted. First, all the

gates generated by topological manipulation of Majorana fermions belong to the Clifford group, and it is impossible to use such operations alone to violate the CHSH inequality [268]. We have to consider instead the multi-qubit MABK inequality. Second, it is not obvious that one can violate the MABK inequality as well using only topological operations. There are two ways to encode a qubit using Majorana fermions, using either two quasiparticles (Majorana fermions) or four quasiparticles (see the details in the supplement of Ref. [27]). In the two-quasiparticle encoding scheme, although the braiding gates exhaust the entire two-qubit Clifford group, they cannot span the whole Clifford group for more than two qubits [278]. Furthermore, braiding Majorana fermions within each qubit cannot change the topological charge of this qubit which fixes the measurement basis. Thus, no violation of the MABK inequality can be achieved using the topological operations alone in the two-quasiparticle encoding scheme. In the four-qusiparticle encoding scheme, it is not straightforward either as braidings in this scheme only allows certain single-qubit rotations and no entanglement can be obtained due to the no-entanglement rule proved already for this encoding scheme [279].

Fortunately, we can overcome this difficulty by taking advantage of the non-destructive measurement of the anyon fusion, which can induce qubit entanglement [280]. In a real physical device, the anyon fusion can be read out non-destructively through the anyon interferometry [281]. In the four-qusiparticle encoding scheme: each qubit is encoded by four Majorana fermions, with the total topological charge 0. The qubit basis-states are represented by $|0\rangle \equiv |((\bullet,\bullet)_{\mathbf{I}},(\bullet,\bullet)_{\mathbf{I}})_{\mathbf{I}}\rangle$ and $|1\rangle \equiv |((\bullet,\bullet)_{\psi},(\bullet,\bullet)_{\psi})_{\mathbf{I}}\rangle$. Here, each $\bullet$ represents a Majorana fermion; $\mathbf{I}$ and ψ represent the two possible fusion channels of a pair of Majorana fermions, with $\mathbf{I}$ standing for the vacuum state and ψ denoting a normal fermion. As explained in the Supplemental Material of Ref. [27], a topologically protected two-qubit CNOT gate can be implemented using braidings together with non-destructive measurements of the anyon fusion [280]. To certify randomness through the MABK inequality, we

need to prepare a three-qubit entangled state. For this purpose, we need in total fourteen Majorana fermions, where twelve of them are used to encode three qubits and another ancillary pair is required for implementation of the effective CNOT gates through measurement of the anyon fusion. Initially, the logical state is $|\Phi\rangle_i = |000\rangle$. We apply first a Hadamard gate on the qubit 1, which can be implemented through a series of anyon braiding as shown in Fig. 9.2.3b, and then two effective CNOT gates on the logical qubits 1, 2, and 2, 3. The final state is the standard three-qubit maximally entangled state $|\Psi\rangle_f = (|000\rangle + |111\rangle)/\sqrt{2}$. After $|\Psi\rangle_f$ is generated, the three qubits can be separated and we need only local braiding and fusion of anyons within each qubit to perform the measurements in the appropriate bases to generate random numbers and certify them through test of the MABK inequality.

To perform the measurements, we read out each qubit according to the input string $\mathscr{I}$ through nondestructive detection of the anyon fusion. If the input is 0, we first braid the Majorana fermions to implement a Hadamard gate H on this qubit (as shown in Fig. 9.2.3b), and then measure the fusion of the first two Majorana fermions within each qubit. The measurement outcome is 0 (1) if the fusion result is $\mathbf{I}$ (ψ). If the input is 1, we first braid the Majorana fermions to implement a B_{23} gate (see Fig. 9.2.3a) on this qubit before the same readout measurement. For instance, with the the input $(x,y,z) = (0,1,1)$, we apply a Hadamard gate to the first qubit and B_{23} gates to the second and the third qubits, followed by the nondestructive measurement of fusion of the first two Majorana fermions in each qubit. Under the state $|\Psi\rangle_f$, the conditional probability of the measurement outcomes (a,b,c) under the measurement setting (x,y,z) for these three qubits is give by

$$P(abc|xyz) = \left|\langle abc|(\mathtt{U}_x\mathtt{U}_y\mathtt{U}_z)|\Psi\rangle_f\right|^2, \tag{9.2.5}$$

where $\mathtt{U}_0 = H$ and $\mathtt{U}_1 = B_{23}$. With this conditional probability, we find the expected value of $\hat{L}$

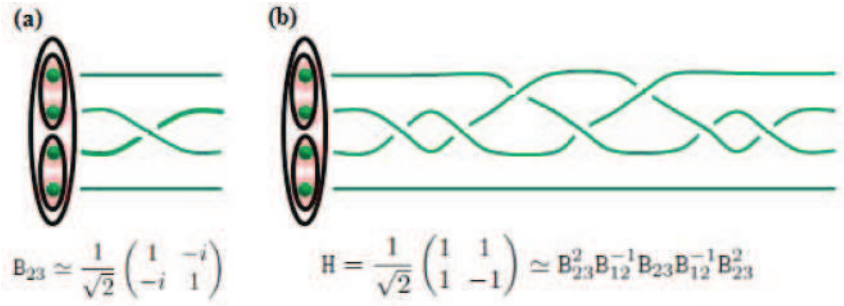

Figure 9.2.3: (Color online) Illustration of the encoding scheme for a logic qubit using Majorana fermions and two single-qubit operations that can be implemented through anyon braiding. Each qubit is encoded by four Majorana fermions. (a)A counterclockwise braiding of Majorana fermions 2 and 3 implements a unitary gate B_{23} on the corresponding qubit. (b) Implementation of the Hadamard gate through composition of anyon braiding. In both (a) and (b), time flows from left to right and $\simeq$ means equal up to an irrelevant overall phase.

defined in Eqs. (1,2) is $\hat{L} = 4$, achieving the maximum quantum violation of the MABK inequality. All the steps for measurements and state preparation are based on the topologically protected operations such as anyon braiding or nondestructive detection of the anyon fusion, so the scheme here is intrinsically fault-tolerant and we should get the ideal value of $\hat{L} = 4$ if the Majorana fermions can be manipulated at will in experiments. Such a large violation perfectly certifies genuine randomness of the measurement outcomes.

9.3 Discussion and summary

In summary, we have shown that genuine number numbers can be generated and certified through topologically manipulation of Majorana fermions, a kind of anyonic excitations in engineered materials. Such a protocol is intrinsically fault-tolerant. Given the rapid experimental progress on realization of Majorana fermions in real materials [43, 254], this protocol offers a promising prospective for application of these topological particles in an important direction of cryptography

with broad implications in science and engineering.

CHAPTER X

Conclusion and outlook

In this thesis, we have discussed and studied three important aspects of topological phases of matter, i.e., their classification, realization and application. In particular, we briefly reviewed the group cohomology classification of interacting bosons and homotopy group classification of free fermions. We introduced a systematic method to construct model Hamiltonians for all the nontrivial topological phases in the periodic table. In order to illustrate how these phases can be realized, we proposed a detailed experiment to realize 3D chiral topological insulators with cold atoms in optical lattices. Moreover, we introduced simple and generic methods to direct measure topological invariants in cold atomic systems and demonstrated that Hopf insulators with large Hopf indexes are kaleidoscopes of various knots and links. Remarkably, these knots and links were simulated to be visible in real experiments. For the application of topological materials, we first demonstrated how to create, braid, and detect Majorana fermions with cold atoms and then proposed to use Majoranas to construct a self-test quantum random number generator.

There are, of course, many other interesting aspects of topological phases that have not been covered. For instance, the topological properties for periodically driven [93, 282–286] or non-

Hermitian systems [287–289] are also important and interesting topics. Furthermore, despite extensive works, there are still many future directions related to the classification, realization and application of topological phases of matter. In the following, we will mention a few of them, topic by topic.

The classification of topological phases

The two methods of classification of topological phases are "only the tip of the iceberg". There are a number of other classification theories, such as: the space group classification [290] of topological crystalline insulators [39], the tensor category [291–293] or simple current algebra [294, 295] approach, and the cobordism [65, 66, 296] approach to SPT phases, etc. All these theories have their own advantages and disadvantages, and a complete and systematic classification theory is still lacking. In the future, it is of great interest and importance to establish such a theory.

The realization of topological phases

Thanks to the advanced technologies, many exotic topological phases are discovered in solid systems, including the $\mathbb{Z}_2$ topological insulators with time reversal symmetry [7, 8], quantum anomalous Hall effect [131], and topological crystalline insulators [297, 298], etc. Some other topological phases are implemented with cold atom [102, 103, 162] or photonic [299, 300] systems or with quantum walks [93, 96]. Nevertheless, many other exotic topological phases have not been realized in the lab yet. Particularly, various bosonic or fermionic symmetry protected/enriched topological phases with strong interactions are theoretically predicted but have not been discovered experimentally hitherto. From the quantum simulation perspective, one important first step might be to

find out microscopic models for these phases [301].

The application of topological phases

As we have discussed in this thesis, non-Abelian anyons might be used to build a quantum computer [57, 69, 251] or a random number generator [27]. For the synthesis of a quantum computer, Majorana fermions are not capable of doing universal computation. Quite recently, several systems have been speculated to harbor Fibonacci anyons [302, 303], which can achieve universal quantum gates through braidings. However, despite all these significant progresses, the experimental realization of Fibonacci anyons seems still far away and there is plenty of room left for further exploration. It might also be interesting to think about other possible applications of topological materials.

APPENDICES

APPENDIX A

Symmetry check

In this Appendix, we explicitly check the symmetries for our constructed Hamiltonians in Chapter III. We also give some details for the description of these Hamiltonians and the calculation of their corresponding topological indices.

A.1 Spin-singlet topological superconductor

We first prove that the Hamiltonian $H_{\rm CI}$ for the spin-singlet topological superconductors (TSCs) constructed in Eq. (4) of the main text has the CI-class symmetry with $T^2 = 1$ and $C^2 = -1$. Let us denote the parity of a function $f(\mathbf{k})$ by $P[f(\mathbf{k})]$, with $P = 1$ (-1) for an even (odd) parity under the exchange $\mathbf{k} \to -\mathbf{k}$. From the product table of the quaternion algebra, it is easy to check that with $P[(q)_1] = P[(\sin k_x + \sin k_y + \sin k_z)] = -1$ and $P[(q)_0] = P[(q)_2] = P[(q)_3] = 1$, we have $P[(q^n)_0] = P[(q^n)_2] = P[(q^n)_3] = 1$ and $P[(q^n)_1] = -1$ for any integer power n. The explicit expression of the

Hamiltonian in Eq. (3.3.2) of the main text is

$$\mathscr{H}_{\rm CI}(\mathbf{k}) = \begin{pmatrix} (q^n)_2 & (q^n)_0 - i(q^n)_1 & (q^n)_3 & 0 \\ (q^n)_0 + i(q^n)_1 & -(q^n)_2 & 0 & (q^n)_3 \\ (q^n)_3 & 0 & -(q^n)_2 & -(q^n)_0 + i(q^n)_1 \\ 0 & (q^n)_3 & -(q^n)_0 - i(q^n)_1 & (q^n)_2 \end{pmatrix}.$$

From the parity of q^n, the time reversal symmetry can be readily seen as

$$[\mathscr{H}_{\rm CI}(\mathbf{k})]^* = \mathscr{H}_{\rm CI}(-\mathbf{k}),$$

so $T_m = \mathbf{I}_4$, the 4×4 identity matrix. The particle-hole symmetry can be seen as

$$C_m[\mathscr{H}_{\rm CI}(\mathbf{k})]^* C_m^{-1} = -\mathscr{H}_{\rm CI}(-\mathbf{k}),$$

with $C_m = \mathbf{I}_2 \otimes \sigma^y$, where $\boldsymbol{\sigma} = (\sigma^x, \sigma^y, \sigma^z)$ denote the Pauli matrices. Apparently, $T^2 = 1$ and $C^2 = -1$ (as $C_m C_m^* = -\mathbf{I}_4$), as it is the case for the CI-class symmetry.

To calculate the topological invariant, we note that the system also has the chiral symmetry $S = TC$ and the $Q(\mathbf{k})$ matrix (defined in the main text) can thus be brought into the block off-diagonal form by a unitary transformation [20, 21]. At the half filling (therefore inside the energy gap) and with a convenient gauge, direct calculation leads to

$$Q(\mathbf{k}) = \begin{pmatrix} 0 & b(\mathbf{k}) \\ b^\dagger(\mathbf{k}) & 0 \end{pmatrix}, \qquad b(\mathbf{k}) = -\begin{pmatrix} (q^n)_3 - i(q^n)_2 & -i(q^n)_0 - (q^n)_1 \\ -i(q^n)_0 + (q^n)_1 & (q^n)_3 + i(q^n)_2 \end{pmatrix} / E_+(\mathbf{k})$$

with $E_+(\mathbf{k}) = |q(\mathbf{k})|^n$, as mentioned in the main text.

A.2 Spin-triplet topological superconductor

The Dirac matrices (also known as the gamma matrices) $\{\gamma^0,\gamma^1,\gamma^2,\gamma^3\}$ are a set of 4×4 matrices, defined as

$$\gamma^0=\begin{pmatrix}\mathbf{I}_2 & \mathbf{0}\\ \mathbf{0} & -\mathbf{I}_2\end{pmatrix},\quad \gamma^1=\begin{pmatrix}\mathbf{0} & \sigma^x\\ -\sigma^x & \mathbf{0}\end{pmatrix},\quad \gamma^2=\begin{pmatrix}\mathbf{0} & \sigma^y\\ -\sigma^y & \mathbf{0}\end{pmatrix},\quad \gamma^3=\begin{pmatrix}\mathbf{0} & \sigma^z\\ -\sigma^z & \mathbf{0}\end{pmatrix},$$

The fifth gamma matrix is defined by $\gamma^5=i\gamma^0\gamma^1\gamma^2\gamma^3=\sigma^x\otimes\mathbf{I}_2$. Using the explicit form of these gamma matrices, the Hamiltonian matrix $\mathscr{H}_{\rm DIII}(\mathbf{k})$ can be written as

$$\mathscr{H}_{\rm DIII}(\mathbf{k})=\begin{pmatrix}0 & 0 & -i(q^n)_0+(q^n)_3 & (q^n)_1-i(q^n)_2\\ 0 & 0 & (q^n)_1+i(q^n)_2 & -i(q^n)_0-(q^n)_3\\ i(q^n)_0+(q^n)_3 & (q^n)_1+i(q^n)_2 & 0 & 0\\ (q^n)_1-i(q^n)_2 & i(q^n)_0-(q^n)_3 & 0 & 0\end{pmatrix}.$$

The $Q(\mathbf{k})$ matrix can thus be written as

$$Q(\mathbf{k})=\begin{pmatrix}0 & b(\mathbf{k})\\ b^\dagger(\mathbf{k}) & 0\end{pmatrix},\qquad b(\mathbf{k})=-\begin{pmatrix}-i(q^n)_0+(q^n)_3 & (q^n)_1-i(q^n)_2\\ (q^n)_1+i(q^n)_2 & -i(q^n)_0-(q^n)_3\end{pmatrix}/E_+(\mathbf{k}).$$

with $E_+(\mathbf{k})=|q(\mathbf{k})|^n$. Note that for the quaternion q defined in Eq. (3.3.7) of the main text, we have $P[(q)_1]=P[(q)_2]=P[(q)_3]=-P[(q)_0]=-1$ and thus $P[(q^n)_1]=P[(q^n)_2]=P[(q^n)_3]=-P[(q^n)_0]=-1$. With the parity properties, one can easily check that

$$\begin{aligned}(\sigma_x\otimes\sigma_y)[\mathscr{H}_{\rm DIII}(\mathbf{k})]^*(\sigma_x\otimes\sigma_y) &= \mathscr{H}_{\rm DIII}(-\mathbf{k}),\\ (\sigma_y\otimes\sigma_y)[\mathscr{H}_{\rm DIII}(\mathbf{k})]^*(\sigma_y\otimes\sigma_y) &= -\mathscr{H}_{\rm DIII}(-\mathbf{k}).\end{aligned}$$

So the symmetry matrix $T_m = \sigma_x \otimes \sigma_y$ and $C_m = \sigma_y \otimes \sigma_y$ with $T^2 = -1$ and $C^2 = 1$ (as $T_m T_m^* = -\mathbf{I}_4$ and $C_m C_m^* = \mathbf{I}_4$), as it is the case for the DIII-class symmetry.

A.3 Chiral topological insulator

The four Gell-Mann matrices used in the text are defined as

$$\lambda_4 = \begin{pmatrix} 0 & 0 & 1 \\ 0 & 0 & 0 \\ 1 & 0 & 0 \end{pmatrix}, \quad \lambda_5 = \begin{pmatrix} 0 & 0 & -i \\ 0 & 0 & 0 \\ i & 0 & 0 \end{pmatrix}, \quad \lambda_6 = \begin{pmatrix} 0 & 0 & 0 \\ 0 & 0 & 1 \\ 0 & 1 & 0 \end{pmatrix}, \quad \lambda_7 = \begin{pmatrix} 0 & 0 & 0 \\ 0 & 0 & -i \\ 0 & i & 0 \end{pmatrix}.$$

The Hamiltonian matrix $\mathscr{H}_{\mathrm{AIII}}(\mathbf{k})$ for the chiral topological insulator has the following explicit form

$$\mathscr{H}_{\mathrm{AIII}}(\mathbf{k}) = \begin{pmatrix} 0 & 0 & (q^n)_1 - i(q^n)_2 \\ 0 & 0 & (q^n)_3 - i(q^n)_0 \\ (q^n)_1 + i(q^n)_2 & (q^n)_3 + i(q^n)_0 & 0 \end{pmatrix}.$$

The Hamiltonian $\mathscr{H}_{\mathrm{AIII}}(\mathbf{k})$ does not have time-reversal or particle-hole symmetry, but it has a chiral symmetry $S_m \mathscr{H}_{\mathrm{AIII}}(\mathbf{k}) S_m^{-1} = -\mathscr{H}_{\mathrm{AIII}}(\mathbf{k})$ with the unitary matrix

$$S_m = \begin{pmatrix} 1 & 0 & 0 \\ 0 & 1 & 0 \\ 0 & 0 & -1 \end{pmatrix}.$$

APPENDIX B

Zero Chern numbers and surface states

In this appendix, we show a detailed analytical proof of the zero Chern numbers for the Hamiltonians given in Chapter IV. Also, more details on how to obtain the surface states and zero energy modes are provided.

B.1 Proof of zero Chern number

In this section, we give an analytical proof of zero Chern numbers in all three directions for the Hamiltonian in the text. First, let us consider the case of C_x. We work in a gapped phase. For a fixed k_x, in order to prove that $C_x = \int_{-\pi}^{\pi} dk_y \int_{-\pi}^{\pi} dk_z F_x(k_y,k_z) = 0$, we note that a sufficient condition is that $F_x(k_y,k_z) = -F_x(-k_y,-k_z)$. In another word, we wish to show $F_x(k_y,k_z)$ has an odd parity under exchange $(k_y,k_z) \to -(k_y,k_z)$. For convenience, we denote the parity of a given function $\mathscr{F}(k_y,k_z)$ as $P[\mathscr{F}] = \{0,1\}$ when $(k_y,k_z) \to -(k_y,k_z)$. Here, 0 (1) means that the function is an even (odd) function. In this notation, our aim is to prove that $P[F_x] = 1$. A key point is that the expression of $F_x(k_y,k_z)$ does not contain any k_x derivatives. Hence, we can regard k_x as

a constant number at every instance. Let $g_1(k_y,k_z) = \sin k_x = c$, $g_2(k_y,k_z) = t\sin k_y$, $g_3(k_y,k_z) = \sin k_z$, and $g_4(k_y,k_z) = (\cos k_x + \cos k_y + \cos k_z + h)$. It is then obvious that $P[g_1] = P[g_4] = 0$ and $P[g_2] = P[g_3] = 1$. We can normalize the vector function as $\hat{\mathbf{g}}(k_y,k_z) = \mathbf{g}(k_y,k_z)/|\mathbf{g}(k_y,k_z)| = (g_1,g_2,g_3,g_4)/\sqrt{g_1^2+g_2^2+g_3^2+g_4^2}$. The components of $\hat{\mathbf{g}}$ have the same parity as the corresponding components of $\mathbf{g}$. From the text (Eq. 4.2.1), we have:

$$\begin{aligned}
\hat{u}_x &= \mathrm{Re}\left[2\hat{\lambda}(\hat{g}_1+i\hat{g}_2)^p(\hat{g}_3-i\hat{g}_4)^q\right] \\
&= 2\hat{\lambda}\mathrm{Re}\left[\sum_{\alpha=0}^{p}\begin{pmatrix} p \\ \alpha \end{pmatrix}\hat{g}_1^{\alpha}(i\hat{g}_2)^{p-\alpha}\sum_{\beta=0}^{q}\begin{pmatrix} q \\ \beta \end{pmatrix}\hat{g}_3^{\beta}(-i\hat{g}_4)^{q-\beta}\right] \\
&= 2\hat{\lambda}\mathrm{Re}\left[\sum_{\alpha=0}^{p}\sum_{\beta=0}^{q}\begin{pmatrix} p \\ \alpha \end{pmatrix}\begin{pmatrix} q \\ \beta \end{pmatrix}(-1)^{q-\beta}i^{p+q-\alpha-\beta}\hat{g}_1^{\alpha}\hat{g}_4^{q-\beta}\hat{g}_2^{p-\alpha}\hat{g}_3^{\beta}\right], \qquad \text{(B.1.1)}
\end{aligned}$$

where $\hat{\lambda} = 1/(|(\hat{g}_1+i\hat{g}_2)|^{2p} + (\hat{g}_3+i\hat{g}_4)|^{2q})$. From Eq. (B.1.1), one obtains

$$P[\hat{n}_x] = \begin{cases} 0 & \text{if } q \text{ is an even integer} \\ 1 & \text{if } q \text{ is an odd integer} \end{cases}.$$

Similarly, by using $\hat{n}_y = \mathrm{Im}[2\hat{\lambda}(\hat{g}_1+i\hat{g}_2)^p(\hat{g}_3-i\hat{g}_4)^q]$, we have $P[\hat{n}_y] = P[\hat{n}_x]\oplus 1$ with $\oplus$ meaning addition modulo 2. In another word, $\hat{n}_x$ and $\hat{n}_y$ always have opposite parity for any values of p and q. Furthermore, from $\hat{n}_z = \hat{\lambda}(|(\hat{g}_1+i\hat{g}_2)|^{2p} - |(\hat{g}_3+i\hat{g}_4)|^{2q})$, we obtain $P[\hat{n}_z] = 0$. As a consequence, $P[\hat{\mathbf{n}}\cdot(\partial_v\hat{\mathbf{n}}\times\partial_\tau\hat{\mathbf{n}})] = 1$. Thus,

$$P[F_x] = P[\hat{\mathbf{n}}\cdot(\partial_{k_y}\hat{\mathbf{n}}\times\partial_{k_z}\hat{\mathbf{n}})] = 1.$$

This proves that $C_x = 0$. By the same parity arguments, one can prove $C_y = 0$ and $C_z = 0$.

B.2 Surface states and zero energy modes

In this section, we give more details on how to numerically calculate the surface states and zero energy modes. For simplicity, we only focus on the midgap surface states induced by abrupt boundaries in the (001) direction. To this end, we inverse Fourier transform k_z to the real space and retain k_x and k_y in the momentum space. Suppose we consider a N_z-site-thick slab, For any fixed (k_x, k_y), we arrange the $2N_z$ basis of the Hilbert space by $(|\downarrow\rangle_1, |\uparrow\rangle_1, \cdots, |\downarrow\rangle_{N_z}, |\uparrow\rangle_{N_z})$, where the subscript denotes the site number. After the inverse Fourier transform, the Hamiltonian can be written in general as $\mathcal{H} = \sum_{k_x,k_y} \mathscr{H}^{k_x,k_y}$, where

$$\mathscr{H}^{k_x,k_y} = \sum_{i=1}^{2N_z}\sum_{j=1}^{2N_z} t_{ij}^{k_x,k_y} c^\dagger_{k_x,k_y,i} c_{k_x,k_y,j}. \tag{B.2.1}$$

We aimed to find an analytical expression for $t_{ij}^{k_x,k_y}$. From the text, the Hamiltonian in the momentum space reads

$$\mathcal{H} = \sum_{\mathbf{k}} \Psi^\dagger(\mathbf{k}) \mathscr{H}(\mathbf{k}) \Psi(\mathbf{k}) = \sum_{\mathbf{k}} \{u_z c^\dagger_{\mathbf{k},\uparrow} c_{\mathbf{k},\uparrow} - u_z c^\dagger_{\mathbf{k},\downarrow} c_{\mathbf{k},\downarrow} + [(u_x + iu_y) c^\dagger_{\mathbf{k},\uparrow} c_{\mathbf{k},\downarrow} + h.c.]\} \quad ,$$

where

$$\begin{aligned} u_x + iu_y &= 2(\sin k_x + it \sin k_y)^p [\sin k_z - i(\cos k_x + \cos k_y + \cos k_z + h)]^q \\ u_z &= (\sin^2 k_x + t^2 \sin^2 k_y)^p - [\sin^2 k_z + (\cos k_x + \cos k_y + \cos k_z + h)^2]^q. \end{aligned} \tag{B.2.2}$$

Since we only do inverse Fourier transform in the z direction and keep (k_x, k_y) in the momentum space, we can regard k_x and k_y as constants. Let $A = 2(\sin k_x + it \sin k_y)^p$ and $B = -i(\cos k_x +$

$\cos k_y + h)$, then Eq. (B.2.2) reduces to

$$\begin{aligned} u_x + iu_y &= A(-ie^{ik_z} + B)^q \\ &= A\sum_{\kappa=0}^{q} \begin{pmatrix} q \\ \kappa \end{pmatrix} (-i)^\kappa e^{i\kappa k_z} B^{q-\kappa} \\ &= \sum_{\kappa=0}^{q} D_\kappa e^{i\kappa k_z}, \end{aligned} \tag{B.2.3}$$

where $D_\kappa = A \begin{pmatrix} q \\ \kappa \end{pmatrix} (-i)^\kappa B^{q-\kappa}$. Similary, for u_z term, define $R = (\sin^2 k_x + t^2 \sin^2 k_y)^p$, $S = 1 + (\cos k_x + \cos k_y + h)^2$, $T = (\cos k_x + \cos k_y + h)$ and $Q = S/T$, Eq. (B.2.3) reduces to

$$\begin{aligned} u_z &= R - T^q (Q + e^{ik_z} + e^{-ikz})^q \\ &= R - \sum_{\alpha+\beta+\kappa=q} \begin{pmatrix} q \\ \alpha, \beta, \kappa \end{pmatrix} T^q Q^\kappa e^{i(\alpha-\beta)k_z} \\ &= R - \sum_{\alpha+\beta+\kappa=q} J_{\alpha\beta\kappa q} e^{i(\alpha-\beta)k_z}, \end{aligned}$$

where $\begin{pmatrix} q \\ \alpha, \beta, \kappa \end{pmatrix} = \dfrac{q!}{\alpha!\beta!\kappa!}$ is the trinomial coefficients and $J_{\alpha\beta\kappa q} = \begin{pmatrix} q \\ \alpha, \beta, \kappa \end{pmatrix} T^q Q^\kappa$. Now we are ready to do the inverse Fourier transform in z direction:

$$\begin{aligned} c_{k_x,k_y,k_z,\sigma} &= \frac{1}{\sqrt{N_z}} \sum_z e^{izk_z} c_{k_x,k_y,z,\sigma}, \\ c^\dagger_{k_x,k_y,k_z,\sigma} &= \frac{1}{\sqrt{N_z}} \sum_z e^{-izk_z} c^\dagger_{k_x,k_y,z,\sigma}. \end{aligned}$$

After the transformation, we obtain

$$\begin{aligned}\mathscr{H}^{k_x,k_y} &= [(Rc^{\dagger}_{k_x,k_y,z,\uparrow}c_{k_x,k_y,z,\uparrow} - \sum_{\alpha+\beta+\kappa=q} J_{\alpha\beta\kappa q}c^{\dagger}_{k_x,k_y,z,\uparrow}c_{k_x,k_y,z-\alpha+\beta,\uparrow}) - (\uparrow\rightarrow\downarrow)] \\ &+[\sum_{\kappa=0}^{q} D_{\kappa}c^{\dagger}_{k_x,k_y,z,\downarrow}c_{k_x,k_y,z-\kappa,\uparrow} + h.c.]. \end{aligned} \tag{B.2.4}$$

Comparing Eq.(B.2.4) with Eq. (B.2.1), we find the expressions

$$\begin{aligned} t^{k_x,k_y}_{2k,2l} &= R\delta_{k,l} - \sum_{\alpha+\beta+\kappa=q} J_{\alpha\beta\kappa q}\delta_{2k,2k+\alpha-\beta}, \\ t^{k_x,k_y}_{2k-1,2l-1} &= -R\delta_{k,l} + \sum_{\alpha+\beta+\kappa=q} J_{\alpha\beta\kappa q}\delta_{2k,2k+\alpha-\beta}, \\ t^{k_x,k_y}_{2k-1,2l} &= \sum_{\kappa=0}^{q} D_{\kappa}\delta_{2k-1,2l+\kappa}, \\ t^{k_x,k_y}_{2k,2l-1} &= \sum_{\kappa=0}^{q} D^{*}_{\kappa}\delta_{2k+\kappa,2l-1}, \end{aligned}$$

where $0 \leqslant k,l \leqslant N_z$. Hence, for each k_x and k_y, we have a $2N_z \times 2N_z$ matrix t^{k_x,k_y} with its (i,j)-th entry t^{k_x,k_y}_{ij}. Numerically diagonizing this matrix for fixed k_x and k_y, we obtain the energy spectrum of $2N_z$ states. For each k_x and k_y, we count the number of surface states by noticing that surface state energies have huge gaps from the bulk state energies. Fig. B.2.1 shows the number of edge states for all k_x and k_y values by imposing a minimum relative separation from the bulk. The number of surface states is counted as the union of all edge states for all (k_x, k_y). The right diagram shows the case where small random perturbations are included. We see that the surface states are very robust to perturbations. In the text, for easy visualization, we plotted the energy spectrum of the Hamiltonian in Fig. 3 at fix $(k_x,k_y) \approx (0.72,0.72)$. There each midgap point corresponds to a surface state.

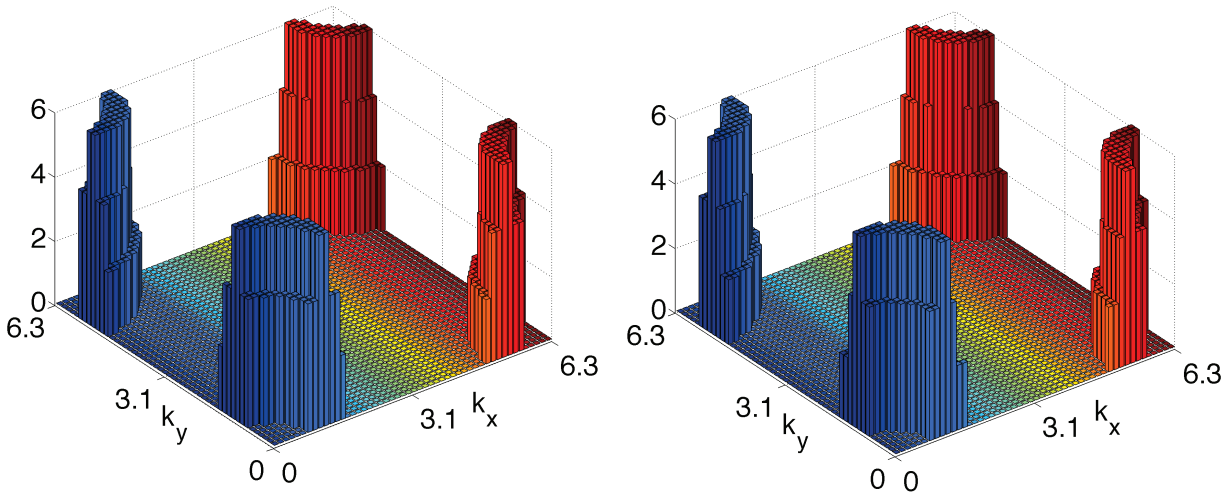

Figure B.2.1: (Color online) Number of surface states for each k_x and k_y in the (001) direction. Both diagrams show the case when $p = 1, q = 3$. The right diagram includes some small random perturbations.

APPENDIX C

Realization of chiral TIs and density of states

In this appendix, we provide more details for Chapter V on the realization of the chiral topological insulator Hamiltonian and include some density of states plots.

C.1 Realization of the effective Hamiltonian

Our main result is to use Raman-assisted tunneling to realize the effective Hamiltonian of the chiral topological insulator given by

$$\begin{aligned} H &= t\sum_{\mathbf{r}}\left[\left(2ihc^{\dagger}_{3,\mathbf{r}}c_{2,\mathbf{r}}+\text{H.c.}\right)+H_{\mathbf{rx}}+H_{\mathbf{ry}}+H_{\mathbf{rz}}\right], \\ H_{\mathbf{rx}} &= ic^{\dagger}_{3,\mathbf{r}-\mathbf{x}}(c_{1,\mathbf{r}}+c_{2,\mathbf{r}})-ic^{\dagger}_{3,\mathbf{r}+\mathbf{x}}(c_{1,\mathbf{r}}-c_{2,\mathbf{r}})+\text{H.c.}, \\ H_{\mathbf{ry}} &= -c^{\dagger}_{3,\mathbf{r}-\mathbf{y}}(c_{1,\mathbf{r}}-ic_{2,\mathbf{r}})+c^{\dagger}_{3,\mathbf{r}+\mathbf{y}}(c_{1,\mathbf{r}}+ic_{2,\mathbf{r}})+\text{H.c.}, \\ H_{\mathbf{rz}} &= 2ic^{\dagger}_{3,\mathbf{r}-\mathbf{z}}c_{2,\mathbf{r}}+\text{H.c.} \end{aligned} \tag{C.1.1}$$

In the following, we provide some complementary details on the realization scheme. The major difficulty is to realize the spin-transferring hopping terms $H_{\mathbf{rx}}, H_{\mathbf{ry}}, H_{\mathbf{rz}}$ along each direction. Let

us focus on a single term first, $H_{\mathbf{rx}}^{(1)} = ic_{3,\mathbf{r}-\mathbf{x}}^{\dagger}(c_{1,\mathbf{r}} + c_{2,\mathbf{r}})$. This corresponds to an atom in the spin state $|1_x\rangle = (|1\rangle + |2\rangle)/\sqrt{2}$ at site $\mathbf{r}$ hopping to site $\mathbf{r}-\mathbf{x}$ while changing the spin state to $|3\rangle$ with hopping strength $i\sqrt{2}$. Diagrammatically, it can be visualized as

$$ic_{3,\mathbf{r}-\mathbf{x}}^{\dagger}(c_{1,\mathbf{r}} + c_{2,\mathbf{r}}) \qquad \Longleftrightarrow \qquad x\text{-direction:} \quad |3\rangle \overset{i\sqrt{2}}{\curvearrowleft} |1_x\rangle \overset{\times}{\curvearrowright} \tag{C.1.2}$$

where $\overset{i\sqrt{2}}{\curvearrowleft}$ means hopping along that direction with strength $i\sqrt{2}$ and $\overset{\times}{\curvearrowright}$ indicates hopping is forbidden. This hopping term can be effected by two Raman beams $\Omega_1^x = i\sqrt{2}\Omega_0 e^{ikz}$ and $\Omega_1^{\pi} = \Omega_0 e^{ikx}$ as shown in Fig. C.1.1.

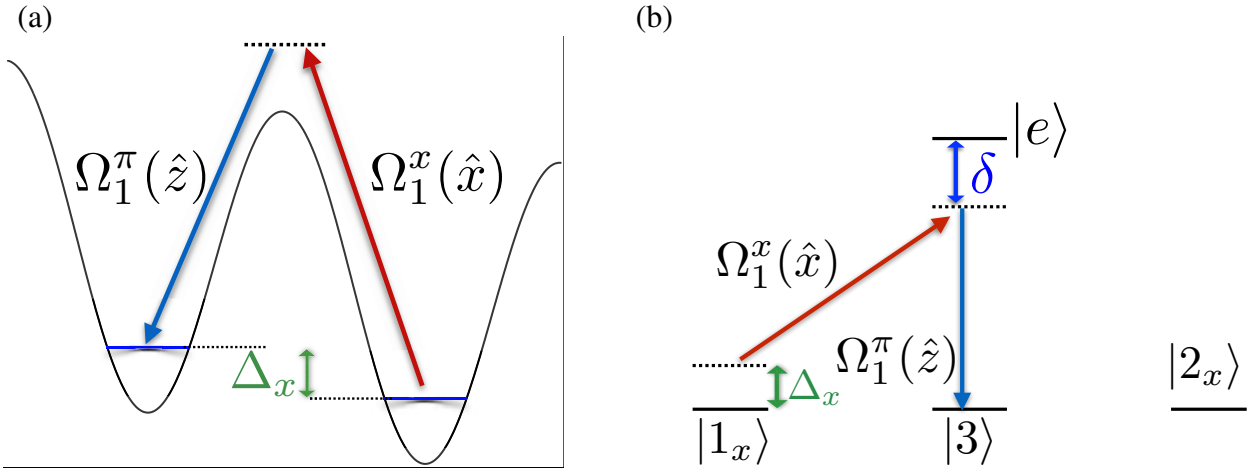

Figure C.1.1: (a) A linear tilt Δ_x per site in the lattice along x-direction. (b) Two Raman beams Ω_1^x and Ω_1^{π} used to produce the tunneling in $H_{\mathbf{rx}}^{(1)}$. The unit vectors in brackets show the polarization direction of the corresponding beam. For the complete optical lattice setup, refer to Fig. 1 in the main text.

The large single-photon detuning δ ensures that the population of the excited state, estimated by $|\Omega_0/\delta|^2$, is negligible. The two-photon detuning Δ_x matches the linear energy shift of the lattice per

site, so that it only allows $|1_x\rangle$ to hop to the left, and the other direction is forbidden by an energy mismatch $2\Delta_x$. The addressing of spin states is done by polarization selection rule. The original spin basis $|1\rangle, |3\rangle, |2\rangle$ differ in the magnetic quantum number m by one successively. So a π-polarized beam Ω_1^π excites the state $|3\rangle$ and a linear $\hat{x}$-polarized beam Ω_1^x excites the superposition state $|1_x\rangle = (|1\rangle + |2\rangle)/\sqrt{2}$ since $\hat{x} \sim (\sigma^+ + \sigma^-)$. So together, these two beams induce a Raman-assisted hopping between $|1_x\rangle$ and $|3\rangle$. The hopping amplitude and phase are controlled by the corresponding Raman beam amplitude and phase. In addition, the wave-vector difference of two beams $\delta\mathbf{k}$ ($(-k, 0, k)$ in this case) has to have a component along the hopping direction (x-direction) to ensure the hopping strength is non-vanishing.

All the other hopping terms in the Hamiltonian are realized in a similar manner. For example, consider the term $c^\dagger_{3,\mathbf{r}+\mathbf{y}}(c_{1,\mathbf{r}} + ic_{2,\mathbf{r}})$, which can be realized by $\Omega_2^y = \sqrt{2}\Omega_0 e^{ikz}$ and $\Omega_2^\pi = \Omega_0 e^{iky}$, polarized along $(\hat{x}+\hat{y})$-direction and $\hat{z}$-direction respectively (see Fig. 1 in the main text). Since $(\hat{x}+\hat{y}) \sim (\sigma^+ + i\sigma^-)$, it couples the state $|2_y\rangle = (|1\rangle + i|2\rangle)/\sqrt{2}$ and $|3\rangle$. A wave-vector difference $\delta\mathbf{k} = (0, -k, k)$ and a two-photon energy detuning Δ_y guarantee the desired hopping along y-direction.

With a number of laser beams required to realize the full Hamiltonian, it is important to check that undesired tunneling terms are forbidden. The linear energy shift per site are taken to satisfy $\Delta_x : \Delta_y : \Delta_z = 1 : 2 : 3$. The energy difference is lower bounded by Δ_x. So if we select a parameter regime such that the Raman-assisted hopping rate t satisfies $t \ll \Delta_x$, then the hopping along the z direction induced by Ω_1^x and Ω_1^π, for instance, have negligible effects because of the large detuning. Other undesired couplings between different beams are disallowed because the wave-vector difference $\delta\mathbf{k}$ may not have the component along a certain direction to induce a hopping along that direction. For example, $\Omega_1^x = i\sqrt{2}\Omega_0 e^{ikz}$ and $\Omega_2^\pi = \Omega_0 e^{iky}$ will not induce a hopping along x-direction as $\delta\mathbf{k}$ does not include a component along x-direction. Moreover, the Raman beams $\Omega_{1,2}^{x,y,z}$ and $\Omega_{1,2}^\pi$ may

induce some on-site spin transferring terms, which can be compensated with some radio-frequency fields.

C.2 Density of States

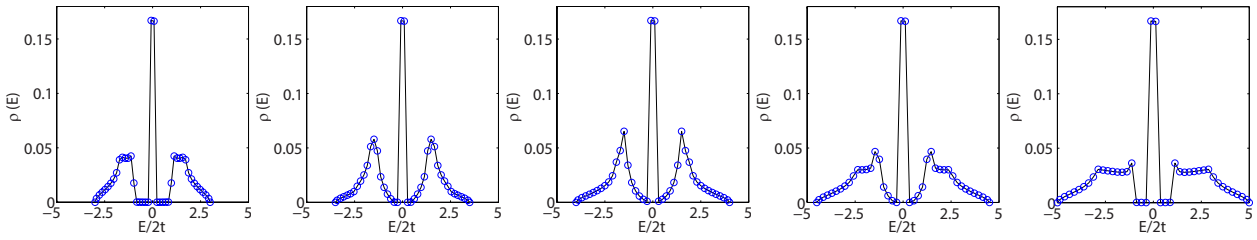

Figure C.2.1: Density of states $\rho(E)$ with respect to the energy E for various values of h ($h = 0, 0.5, 1, 1.5, 2$ from left to right). The middle flat band is clearly visible at zero energy. The bulk band gaps are $2t, t/2, 0, t/2, 2t$ respectively.

In Fig. 2(c) of the main text, we plotted the momentum distribution of atoms $\rho_{\text{cry}}(\mathbf{k})$ for various h at a fixed chemical potential $\mu/2t = -2$. It is useful to include the density of states $\rho(E)$ for various values of the parameter h. In Fig. C.2.1 here, we show the density of states plots. The macroscopic zero-energy flat band is prominent in each plot. The band gap is also clearly visible for $h = 0, 2$ (less visible for $h = 0.5, 1.5$.). In Fig. 2(c) of the main text, the figures correspond to a filling up to $\mu/2t = -2$. A change of Fermi surface topology can be observed in those figures.

APPENDIX D

Measuring topological invariants in optical lattices

This appendix gives more details on the calculations of the topological invariants and the numerical simulations of real experiments. In section one, we show how the density distribution in momentum space is obtained when an open boundary condition is assumed. In section two we show how the random perturbation and harmonic trapping potential are parametrized and added. In section three, we give more results of the numerical simulations and provide the definition of the four Gell-Mann matrices used in the main text.

D.1 Momentum Density distributions with open boundary condition

In Chapter 6, we have numerically simulated the momentum density distribution of an actual ultracold atoms experiment with finite-size lattices and possible imperfections under an open boundary condition. Here, we provide more details on how the momentum density distribution is calculated.

Consider a generic quadratic Hamiltonian in real space:

$$H = \sum_{\mathbf{r},\mathbf{s},\alpha,\beta} a^{\dagger}_{\mathbf{r},\alpha} \mathscr{H}_{\mathbf{r}\alpha,\mathbf{s}\beta} a_{\mathbf{s},\beta}, \tag{D.1.1}$$

where $\mathbf{r},\mathbf{s}$ denote the lattice sites and α,β are the pseudospin indices. One can solve the Schröinger equation $\mathscr{H}\Phi_i = \varepsilon_i \Phi_i$ to obtain the single-particle energy spectrum. In the matrix form, One can diagonalize $\mathscr{H}$ by an unitary matrix U: $\mathscr{H} = U^{\dagger}\mathscr{E}U$, and find the single-particle eigen-mode $b_{\mathbf{r},\alpha} = \sum_{\mathbf{s},\beta} U_{\mathbf{r}\alpha,\mathbf{s}\beta} a_{\mathbf{s},\beta}$. Here $\mathscr{E} = \mathrm{diag}(\varepsilon_1, \varepsilon_2, \cdots)$ is a diagonal matrix. For a free fermonic system described by Eq.(D.1.1), the total particle number $\mathscr{N} = \sum_{\mathbf{r},\alpha} a^{\dagger}_{\mathbf{r},\alpha} a_{\mathbf{r},\alpha}$ is a conserved quantity $[H,\mathscr{N}] = 0$. These $\mathscr{N}$ particles will occupy the first $\mathscr{N}$ eigen-modes with lowest eigen-energies. Consequently, the ground state of the system reads

$$|G\rangle = \prod_{i=1}^{\mathscr{N}} b^{\dagger}_i |0\rangle, \tag{D.1.2}$$

where we have suppressed $\mathbf{r}$ and α into a single index i for the occupied eigen-modes. Then the density distribution in momentum space can be obtained by using of the definition:

$$n_{\alpha}(\mathbf{k}) = \langle G | a^{\dagger}_{\alpha}(\mathbf{k}) a_{\alpha}(\mathbf{k}) | G \rangle. \tag{D.1.3}$$

We do a Fourier transform to go to the real space:

$$\begin{aligned} n_{\alpha}(\mathbf{k}) &= \langle G | a^{\dagger}_{\alpha}(\mathbf{k}) a_{\alpha}(\mathbf{k}) | G \rangle \\ &= \langle G | \frac{1}{\sqrt{\mathscr{L}}} \sum_{\mathbf{r}} e^{i\mathbf{k}\cdot\mathbf{r}} a^{\dagger}_{\mathbf{r},\alpha} \frac{1}{\sqrt{\mathscr{L}}} \sum_{\mathbf{r}'} e^{-i\mathbf{k}\cdot\mathbf{r}'} a_{\mathbf{r}',\alpha} | G \rangle \\ &= \frac{1}{\mathscr{L}} \sum_{\mathbf{r},\mathbf{r}'} \langle G | a^{\dagger}_{\mathbf{r},\alpha} a_{\mathbf{r}',\alpha} | G \rangle e^{i\mathbf{k}\cdot(\mathbf{r}-\mathbf{r}')}, \end{aligned} \tag{D.1.4}$$

where $\mathscr{L}$ denotes the number of lattice sites. Noting that $a_{\mathbf{r},\alpha} = \sum_{\mathbf{s},\beta}(U^\dagger)_{\mathbf{r}\alpha,\mathbf{s}\beta} b_{\mathbf{s},\beta}$, the quantity $\langle G|a^\dagger_{\mathbf{r},\alpha}a_{\mathbf{r}',\alpha}|G\rangle$ can be further simplified as:

$$\begin{aligned}\langle G|a^\dagger_{\mathbf{r},\alpha}a_{\mathbf{r}',\alpha}|G\rangle &= \langle G|\sum_{\mathbf{s},\beta}(U^\dagger)^*_{\mathbf{r}\alpha,\mathbf{s}\beta} b^\dagger_{\mathbf{s},\beta}\sum_{\mathbf{s}',\beta'}(U^\dagger)_{\mathbf{r}'\alpha,\mathbf{s}'\beta'} b_{\mathbf{s}',\beta'}|G\rangle \\ &= \sum_{\mathbf{s},\beta,\mathbf{s}',\beta'}\langle G|b^\dagger_{\mathbf{s},\beta}b_{\mathbf{s}',\beta'}|G\rangle (U^\dagger)^*_{\mathbf{r}\alpha,\mathbf{s}\beta}(U^\dagger)_{\mathbf{r}'\alpha,\mathbf{s}'\beta'} \\ &= \sum_{i}^{\mathscr{N}}(U^\dagger)^*_{\mathbf{r}\alpha,i}(U^\dagger)_{\mathbf{r}'\alpha,i}.\end{aligned} \tag{D.1.5}$$

In the last step of Eq. (D.1.5), we have used the following equation

$$\langle G|b^\dagger_{\mathbf{s},\beta}b_{\mathbf{s}',\beta'}|G\rangle = \begin{cases} 1 & \text{if } \mathbf{s}=\mathbf{s}', \beta=\beta' \text{ and the eigen-mode } b_{\mathbf{s},\beta} \text{ is occupied} \\ 0 & \text{otherwise.}\end{cases}$$

Combining Eq. (D.1.5) and Eq.(D.1.4), we can obtain the momentum density distribution for each pseudospin component from a generic quadratic real-space Hamiltonian with a specific filling number (the filling number is defined as the total particle number devided by the lattice site number: $f = \mathscr{N}/\mathscr{L}$). Similarly, one can rotate the pseudospin and use the same method to compute the momentum density distribution of a superposition state $n_{a|\alpha\rangle+b|\beta\rangle}(\mathbf{k})$.

D.2 Random perturbations and harmonic trapping potential

As have discussed in the main text, a real optical lattice experiment always has a harmonic trapping potential, which is typically of the following form:

$$H_{\text{trap}} = \frac{1}{2}m\omega^2\sum_{\mathbf{r},\alpha}d^2_{\mathbf{r}}a^\dagger_{\mathbf{r},\alpha}a_{\mathbf{r},\alpha}, \tag{D.2.1}$$

where $d_{\mathbf{r}}$ is the distance from the center of the trap to the lattice site $\mathbf{r}$. In our numerical simulations, we use $\gamma_{\mathrm{T}} = m\omega^2 a^2/(2t)$ to parametrize the influence of this trapping potential. Here a is the lattice constant and t is the hopping strength. For a typical experiment, $t/\hbar \sim 1$kHz, $a \sim 400$ nm, and γ_{T} ranges from 10^{-3} (^{6}Li with $\omega/2\pi = 60$ Hz) to 2×1^{-2} (^{40}K with $\omega/2\pi = 100$ Hz). To count other possible imperfections, we also considered a random perturbation term

$$H_{\mathrm{rand}} = \gamma_{\mathrm{R}} t \sum_{\mathbf{r},\mathbf{s},\alpha,\beta} a^{\dagger}_{\mathbf{r},\alpha} \mathscr{R}_{\mathbf{r}\alpha,\mathbf{s}\beta} a_{\mathbf{s},\beta}, \tag{D.2.2}$$

where $\mathscr{R}$ is a random hermitian matrix with its largest eigenvalue normalized to unit.

In the numerical simulations, we add H_{trap} and H_{rand} into the original Hamiltonians and calculated the momentum density distributions using the method described in Sec.I. Although we only showed partial results in Fig. 1, Fig.2 and Table I to keep conciseness, we in fact have done substantial calculations with a number of different choices of parameters $(\gamma_{\mathrm{T}}, \gamma_{\mathrm{R}})$ for both the 2D QAH and 3D CTI cases. Our results consistently manifested that the deduced topological invariants are very robust against the trapping potential and random perturbations.

D.3 More results of the numerical simulations

In this section, we provide more numerical results for both the 2D quantum anomalous Hall effect and 3D chiral topological insulators.

2D QAH effect.—In the main text, we have plotted the momentum density distributions of the first band in Fig. 1, which in fact provided enough information to extract the corresponding topological invariant, i.e., the first Chern number. These density distributions are the rough data coming directly from the TOF measurements. To extract the Chern number, an intermediate step is to cal-

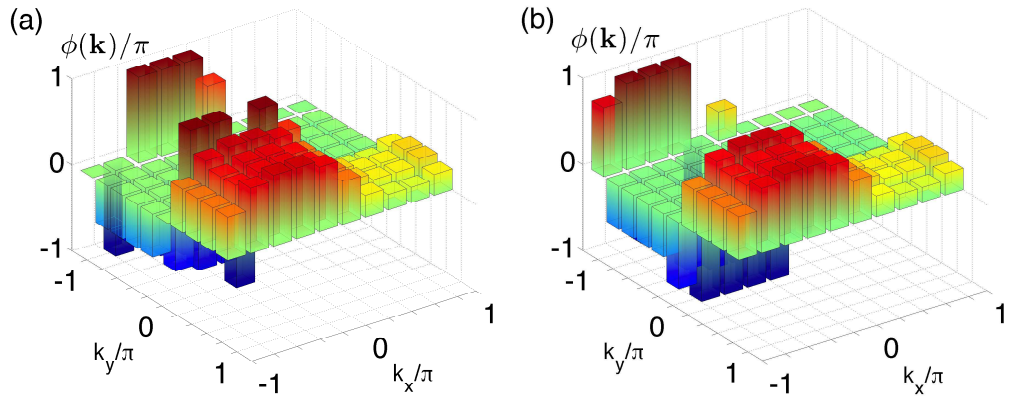

Figure D.2.1: (color online). Relative phase factors in momentum space for the first band of the Hamiltonian H_{QAH} with lattice size 10×10. (a) Periodic boundary condition without perturbation and trapping potential. (b) Open boundary conditions with random perturbations and harmonic trapping. The parameters are chosen the same as in Fig. 1 in the main text.

culate the relative phase between the spin up and down components of the Bloch wavefunction. A little algebra will lead to the following equations:

$$2n_{|\uparrow\rangle+|\downarrow\rangle}(\mathbf{k}) = 1+2\sqrt{n_{\uparrow}(\mathbf{k})\times(1-n_{\uparrow}(\mathbf{k}))}\cos(\phi(\mathbf{k})) \tag{D.3.1}$$

$$2n_{i|\uparrow\rangle+|\downarrow\rangle}(\mathbf{k}) = 1+2\sqrt{n_{\uparrow}(\mathbf{k})\times(1-n_{\uparrow}(\mathbf{k}))}\sin(\phi(\mathbf{k})). \tag{D.3.2}$$

Plugging the density distributions observed from TOF measurements into the above equations, we can obtain the relative phase. We have done this calculation for both periodic and open boundary conditions and the corresponding relative phase factors are shown in Fig. 1. With the relative phases and the density distributions, the Bloch wavefunction for the first band is determined up to an overall phase. Using the method introduced in the main text, we are able to obtain the desired Chern number.

3D CTI.—For 3D chiral topological insulators, let us first write down explicitly the four Gell-Mann matrices used in the Hamiltonian H_{CTI} in the main text:

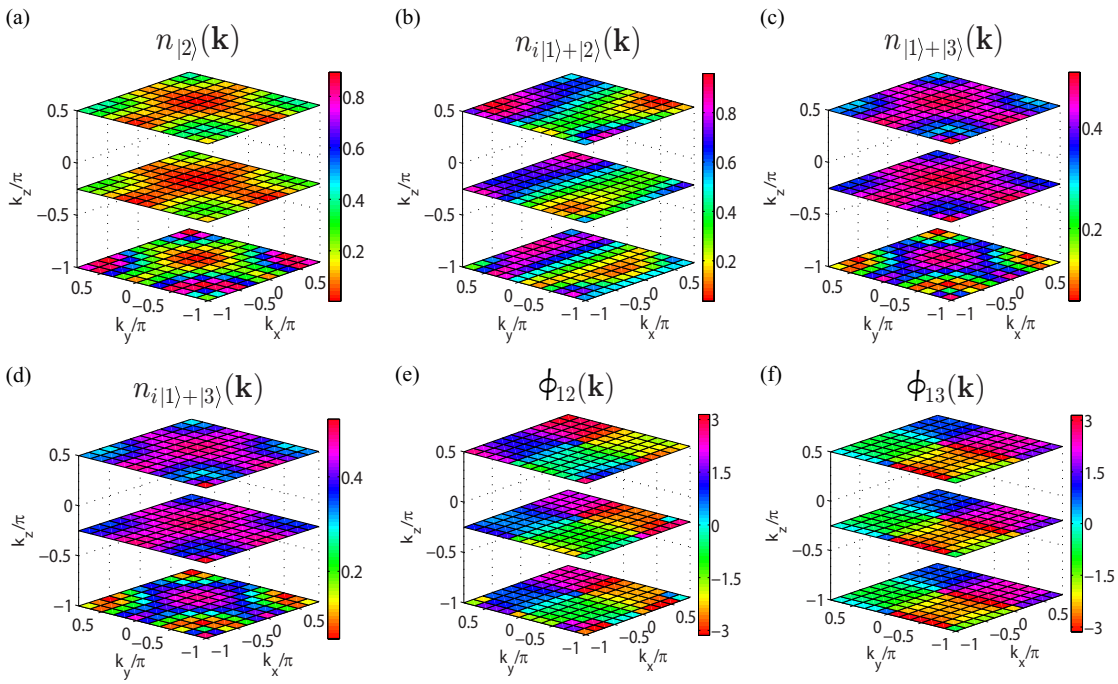

Figure D.3.1: (color online). Momentum density distributions and relative phase factors for the middle flat band with open boundary condition and lattice size $12 \times 12 \times 12$. Only the results for layers correspond to $k_z = -\pi$, $-\pi/4$ and $\pi/2$ are plotted. The parameters are chosen the same as in Fig. 2 in the main text.

$$G_4 = \begin{pmatrix} 0 & 0 & 1 \\ 0 & 0 & 0 \\ 1 & 0 & 0 \end{pmatrix}, \quad G_5 = \begin{pmatrix} 0 & 0 & -i \\ 0 & 0 & 0 \\ i & 0 & 0 \end{pmatrix}, \quad G_6 = \begin{pmatrix} 0 & 0 & 0 \\ 0 & 0 & 1 \\ 0 & 1 & 0 \end{pmatrix}, \quad G_7 = \begin{pmatrix} 0 & 0 & 0 \\ 0 & 0 & -i \\ 0 & i & 0 \end{pmatrix}.$$

One can do a Fourier transformation to get the expression of H_{CTI} in the momentum space [24,80]:

$$H_{\mathrm{CTI}} = \sum_{\mathbf{k}} \psi_{\mathbf{k}}^{\dagger} \mathscr{H}_{\mathrm{CTI}}(\mathbf{k}) \psi_{\mathbf{k}},$$

where $\psi_{\mathbf{k}}^{\dagger} = (a_{\mathbf{k};1}^{\dagger}, a_{\mathbf{k};2}^{\dagger}, a_{\mathbf{k};3}^{\dagger})$ and $\mathscr{H}_{\mathrm{CTI}}(\mathbf{k}) = \sum_{j=1}^{4} G_{3+j} q_j(\mathbf{k})$ with $[q_1(\mathbf{k}), q_2(\mathbf{k}), q_3(\mathbf{k}), q_4(\mathbf{k})] = [\sin k_x, \sin k_y, \sin k_z, m - \cos k_x - \cos k_y - \cos k_z]$. One can easily check that this Hamiltonian in deed has a chiral symmetry represented by $S\mathscr{H}_{\mathrm{CTI}}(\mathbf{k})S^{-1} = -\mathscr{H}_{\mathrm{CTI}}(\mathbf{k})$, where $S \equiv \mathrm{diag}(1,1,-1)$ is a unitary matrix. This chiral symmetry will lead to an exactly flat band with zero energy [24, 80].

In the main text, we have plotted partial of momentum density distributions of the middle flat band in Fig 2 (b) and (c). Here we plot more results of the density distributions and the relative phases in Fig 2. Similar as the case of QAH effect, the momentum density distributions can be observed directly from the layer-by-layer TOF measurements and the relative phases can be calculated from the observed density distributions. After all the density distributions are observed in an actual experiment, the Chern-Simons term characterizing the topological structure of the Block band can be readily extracted using the method described in the main text.

Besides the Chern-Simons term for the middle flat band shown in Table I in the main text, we have also calculated it for both the first (lowest) and third (highest) bands. Our results are shown in Table I of this appendix.

	Size	m	Periodic	Open	Trap	Pert.+Trap
CTI (CS_1/π)	10^3	2	0.246	0.228	0.231	0.231
	12^3	2	0.248	0.228	0.235	0.235
	10^3	4	5.8×10^{-5}	8.6×10^{-5}	1.5×10^{-4}	1.4×10^{-4}
CTI (CS_3/π)	10^3	2	0.246	0.226	0.227	0.227
	12^3	2	0.248	0.229	0.230	0.231
	10^3	4	5.8×10^{-5}	5.0×10^{-5}	1.7×10^{-4}	1.8×10^{-4}

Table D.1: The Chern-Simons terms of the first and third bands for the Hamiltonian H_{CTI}. The parameters are chosen the same as in Fig. 2 in the main text.

D.4 Non-diagonal terms of Green's function

In this section, we show how to derive Eq. (4) in the main text. Let us begin with the expression of spectral function in the zero-temperature limit (we have set $\hbar = 1$ through out this appendix) [179]:

$$A_\tau(\omega,\mathbf{k}) = \sum_n |\langle\psi_n|c_{\mathbf{k},\tau}|\psi_0\rangle|^2\delta(\omega+E_n-E_0) \quad \text{for } \omega<0, \tag{D.4.1}$$

$$A_\tau(\omega,\mathbf{k}) = \sum_n |\langle\psi_n|c^\dagger_{\mathbf{k},\tau}|\psi_0\rangle|^2\delta(\omega+E_0-E_n) \quad \text{for } \omega>0, \tag{D.4.2}$$

where $|\psi_n\rangle$ denotes the eigenstate of $\hat{K}=\hat{H}-\mu\hat{N}$ with eigenvalue E_n and $|\psi_0\rangle$ is the ground state; $\hat{H}$ is the many-particle Hamiltonian, $\hat{N}$ and μ represent the total fermion number operator and the chemical potential, respectively; $c^\dagger_{\mathbf{k},\tau}$ ($c_{\mathbf{k},\tau}$) is the creation (annihilation) operator of the fermionic atom in state $|\tau\rangle$ with momentum $\mathbf{k}$. The spectral function is normalized to unity for each momentum $\mathbf{k}$: $\int d\omega A_\tau(\omega,\mathbf{k})=1$. From the main text, we can measure the spectrum function $A_\tau(\omega,\mathbf{k})$ ($\tau=\eta,\ \eta',\ +,$ or I). by using momentum-resolved Raman or radio frequency (RF) spectroscopy. Here, we want to derive an equation that enables us to compute the non-diagonal

terms of Green's function. To this end, let us define another function $f_{\eta\eta'}(\omega,\mathbf{k})$ as

$$f_{\eta\eta'}(\omega,\mathbf{k}) = \begin{cases} \sum_n \langle\psi_n|c_{\mathbf{k},\eta}|\psi_0\rangle\langle\psi_0|c^\dagger_{\mathbf{k},\eta'}|\psi_n\rangle\delta(\omega+E_n-E_0) & \text{for } \omega<0, \\ \sum_n \langle\psi_0|c_{\mathbf{k},\eta}|\psi_n\rangle\langle\psi_n|c^\dagger_{\mathbf{k},\eta'}|\psi_0\rangle\delta(\omega+E_0-E_n) & \text{for } \omega>0. \end{cases} \tag{D.4.3}$$

Noting that the Matsubara Green's function in the Lehmann representation reads [169]

$$G_{\eta\eta'}(i\omega,\mathbf{k}) = \sum_n [\frac{\langle\psi_n|c_{\mathbf{k},\eta}|\psi_0\rangle\langle\psi_0|c^\dagger_{\mathbf{k},\eta'}|\psi_n\rangle}{i\omega+(E_n-E_0)} + \frac{\langle\psi_0|c_{\mathbf{k},\eta}|\psi_n\rangle\langle\psi_n|c^\dagger_{\mathbf{k},\eta'}|\psi_0\rangle}{i\omega-(E_n-E_0)}],$$

then it is straightforward to get that

$$G_{\eta\eta'}(i\omega,\mathbf{k}) = \int d\omega' \frac{f_{\eta\eta'}(\omega',\mathbf{k})}{i\omega-\omega'}. \tag{D.4.4}$$

Now, let us expand A_+ and A_I in the $|\eta\rangle$, $|\eta'\rangle$ basis using Eq.(D.4.1) and Eq. (D.4.2). For $\omega<0$, we have

$$\begin{aligned} A_+(\omega,\mathbf{k}) &= \sum_n |\langle\psi_n|c_{\mathbf{k},+}|\psi_0\rangle|^2\delta(\omega+E_n-E_0) \\ &= \sum_n |\langle\psi_n|\frac{c_{\mathbf{k},\eta}+c_{\mathbf{k},\eta'}}{\sqrt{2}}|\psi_0\rangle|^2\delta(\omega+E_n-E_0) \\ &= \frac{1}{2}\{[\sum_n \langle\psi_0|c^\dagger_{\mathbf{k},\eta}|\psi_n\rangle\langle\psi_n|c_{\mathbf{k},\eta}|\psi_0\rangle\delta(\omega+E_n-E_0)] \\ &\quad +[\sum_n \langle\psi_0|c^\dagger_{\mathbf{k},\eta'}|\psi_n\rangle\langle\psi_n|c_{\mathbf{k},\eta'}|\psi_0\rangle\delta(\omega+E_n-E_0)] \\ &\quad +[\sum_n \langle\psi_0|c^\dagger_{\mathbf{k},\eta}|\psi_n\rangle\langle\psi_n|c_{\mathbf{k},\eta'}|\psi_0\rangle\delta(\omega+E_n-E_0)] \\ &\quad +[\sum_n \langle\psi_0|c^\dagger_{\mathbf{k},\eta'}|\psi_n\rangle\langle\psi_n|c_{\mathbf{k},\eta}|\psi_0\rangle\delta(\omega+E_n-E_0)] \\ &= \frac{1}{2}[A_\eta(\omega,\mathbf{k})+A_{\eta'}(\omega,\mathbf{k})+f^*_{\eta\eta'}(\omega,\mathbf{k})+f_{\eta\eta'}(\omega,\mathbf{k})], \end{aligned} \tag{D.4.5}$$

and

$$\begin{aligned} A_I(\omega,\mathbf{k}) &= \sum_n |\langle\psi_n|c_{\mathbf{k},I}|\psi_0\rangle|^2\delta(\omega+E_n-E_0) \\ &= \sum_n |\langle\psi_n|\frac{c_{\mathbf{k},\eta}+ic_{\mathbf{k},\eta'}}{\sqrt{2}}|\psi_0\rangle|^2\delta(\omega+E_n-E_0) \\ &= \frac{1}{2}\{A_\eta(\omega,\mathbf{k})+A_{\eta'}(\omega,\mathbf{k})+i[f^*_{\eta\eta'}(\omega,\mathbf{k})-f_{\eta\eta'}(\omega,\mathbf{k})]\}. \end{aligned} \tag{D.4.6}$$

Consequently, we have for $\omega<0$,

$$f_{\eta\eta'} = \frac{1}{2}[(2A_+-A_\eta-A_{\eta'})+i(2A_I-A_\eta-A_{\eta'})]. \tag{D.4.7}$$

By similar calculations using Eq. (D.4.2), one can check that Eq. (D.4.7) is also valid for $\omega>0$. An integration of both sides of Eq. (D.4.7) leads to:

$$\begin{aligned} \int d\omega' \frac{f_{\eta\eta'}(\omega',\mathbf{k})}{i\omega-\omega'} &= \frac{1}{2}\int d\omega' \frac{[2A_+(\omega',\mathbf{k})-A_\eta(\omega',\mathbf{k})-A_{\eta'}(\omega',\mathbf{k})]}{i\omega-\omega'} \\ &+ \frac{i}{2}\int d\omega' \frac{[2A_I(\omega',\mathbf{k})-A_\eta(\omega',\mathbf{k})-A_{\eta'}(\omega',\mathbf{k})]}{i\omega-\omega'}, \end{aligned} \tag{D.4.8}$$

which gives the Eq. (4) in the main text.

D.5 Numerical simulations

In our numerical simulations, we consider a finite size lattice with periodic boundary condition. We exactly diagonalize the total Hamiltonian with the trapping potential to obtain the energy spectrum and corresponding eigenstates. The chemical potential is set to be zero. After we have obtained the full eigenstates and eigenenergies, we compute the spectrum function using Eq. (D.4.1) and

(D.4.2). The creation (annihilation) operators in momentum space are obtained by a Fourier transformation

$$\begin{cases} c_{\mathbf{k},\tau} &= \frac{1}{\sqrt{L_x}} \sum_{\mathbf{r}} e^{-i\mathbf{k}\cdot\mathbf{r}} c_{\mathbf{r},\tau} \\ c^{\dagger}_{\mathbf{k},\tau} &= \frac{1}{\sqrt{L_x}} \sum_{\mathbf{r}} e^{i\mathbf{k}\cdot\mathbf{r}} c^{\dagger}_{\mathbf{r},\tau} \end{cases},$$

where L_x is the lattice size number. Since in a real experiment, we can only measure the spectrum functions at discretized frequency and momentum, we use a Gaussian distribution $D(x,x_0,s) \equiv \frac{1}{\sqrt{2\pi}s} e^{-(x-x_0)^2/(2s^2)}$ to approximate the delta function: $\delta(x-x_0) = \lim_{s\to 0} D(x,x_0,s)$. In Fig 1a in the main text, we have only plotted $A_{\uparrow}(\omega,0)$ and $A_{+}(\omega,0)$ for simplicity. Other spectrum functions at different momentum have similar peak structures. To calculate the topological invariant χ, we first use a discretized version of Eq. (2) in the main text to calculate the diagonal terms of the Green's function at zero frequency. Then we use Eq. (D.4.8) here to calculate the non-diagonal terms. After we obtained the whole Green's function at different momentum, χ can be obtained directly by a discretized version of Eq. (6) in the main text.

APPENDIX E

Stereographic coordinates, perturbations, and Hopf link

In this appendix, we give more details on the definition of stereographic coordinates, the experimental imperfections and the plot of Hopf link from the TOF imaging data.

E.1 Stereographic coordinates

For Hopf insulators with a cubic lattice, the first BZ is a 3D torus $\mathbb{T}^3$. Since it is not convenient to draw and visualize different knots and links in $\mathbb{T}^3$, we first do a map g to go from $\mathbb{T}^3$ to $\mathbb{S}^3$ and use a stereographic coordinate system to represent $\mathbb{S}^3$. The stereographic projection used in this thesis is defined as:

$$(x,y,z) = \frac{1}{1+\eta_4}(\eta_1,\eta_2,\eta_3), \tag{E.1.1}$$

where (x,y,z) and $(\eta_1,\eta_2,\eta_3,\eta_4)$ are points of $\mathbb{R}^3$ and $\mathbb{S}^3$, respectively.

E.2 Perturbations to the Hamiltonian

In realistic experiments, there are additional noises other than the ideal Hamiltonian given by Eq. (7.2.3). The first one is a weak global harmonic trap typically present in cold atom experiment. It is of the form $H_{\text{trap}} = \frac{1}{2}m\omega^2 \sum_{\mathbf{r},\sigma} d_{\mathbf{r}}^2 c_{\mathbf{r},\sigma}^\dagger c_{\mathbf{r},\sigma}$, where $\sigma = \uparrow, \downarrow$, m is the mass of the atom and $d_{\mathbf{r}}$ is the distance from the center of the trap to the lattice site $\mathbf{r}$. We use $\gamma_{\text{t}} = m\omega^2 a^2/2$ to parametrize the relative strength of the trap with a denoting the lattice constant. The other perturbation we consider is a random noise of the form $H_{\text{rand}} = \gamma_{\text{r}} \sum_{\mathbf{r},\mathbf{r}',\sigma,\sigma'} c_{\mathbf{r},\sigma}^\dagger \mathscr{R}_{\mathbf{r}\sigma,\mathbf{r}'\sigma'} c_{\mathbf{r}',\sigma'}$ where γ_{r} characterizes the strength of the noise and $\mathscr{R}$ is a random Hermitian matrix with its largest eigenvalue normalized to unity.

E.3 Seeing links and knots from time-of-flight data

As discussed in the main text, the spin orientation $\hat{\mathbf{S}}(\mathbf{k})$ in real experiment is always pixelized with finite resolution. Therefore, for a specific orientation, $\hat{\mathbf{S}}_1$ for instance, the measured $\hat{\mathbf{S}}(\mathbf{k})$ can only be approximated rather than exactly equal to $\hat{\mathbf{S}}_1$ at any momentum point $\mathbf{k}$. Consequently, one may consider a small ε-neigborhood of $\hat{\mathbf{S}}_1$:

$$N_\varepsilon(\hat{\mathbf{S}}_1) = \{\hat{\mathbf{S}} : \ |\hat{\mathbf{S}} - \hat{\mathbf{S}}_1| \leq \varepsilon\}, \tag{E.3.1}$$

where $|\hat{\mathbf{S}} - \hat{\mathbf{S}}_1| = [(\hat{S}_x - \hat{S}_{1x})^2 + (\hat{S}_y - \hat{S}_{1y})^2 + (\hat{S}_z - \hat{S}_{1z})^2]^{1/2}$ measures the distance between $\hat{\mathbf{S}}$ and $\hat{\mathbf{S}}_1$. Let us denote the preimages of all orientations in $N_\varepsilon(\hat{\mathbf{S}}_1)$ as a set $P_\varepsilon(\hat{\mathbf{S}}_1) = (f \circ g)^{-1}[N_\varepsilon(\hat{\mathbf{S}}_1)]$. With a finite resolution, the BZ is discrete and contains finite momentum points, and so does $P_\varepsilon(\hat{\mathbf{S}}_1)$. As a result, one has to wisely choose an appropriate value for ε so that $P_\varepsilon(\hat{\mathbf{S}}_1)$ contains a

proper amount of momentum points to depict the loop structure of $(f \circ g)^{-1}(\hat{\mathbf{S}}_1)$. To obtain Fig. 7.3.1**b** in our numerical simulation, we examine the discrete $\hat{\mathbf{S}}(\mathbf{k})$ (supposed to be observed from time-of-flight measurements) at each momentum point $\mathbf{k}$ and append $\mathbf{k}$ into the set $P_{1\varepsilon}$ ($P_{2\varepsilon}$) if $\hat{\mathbf{S}}(\mathbf{k})$ is in a ε-neigborhood of $\hat{\mathbf{S}}_1$ ($\hat{\mathbf{S}}_2$). Fig. 7.3.1**b** can in turn be obtained by plotting $g(P_{1\varepsilon})$ and $g(P_{2\varepsilon})$ in the stereographic coordinate system defined above.

APPENDIX F

Time evolution and Majorana correlation functions

In this appendix, we provide more details for Chapter VIII on time evolution and Majorana correlation functions.

F.1 Time evolution

We first Fourier transform the Hamiltonian (1) into real space, with the modes in real space denoted by $c_{\mathbf{r}}$. A line defect has chemical potential μ_d instead of μ_0. We define the Majorana operators at each lattice site with $\gamma_{\mathbf{r},A} = (c^\dagger_{\mathbf{r}} + c_{\mathbf{r}})$ and $\gamma_{\mathbf{r},B} = i(c^\dagger_{\mathbf{r}} - c_{\mathbf{r}})$. In terms of these Majorana operators, the Hamiltonian has the following form:

$$H = \frac{i}{2}\sum_{\mathbf{p},\mathbf{q}} \mathscr{H}_{\mathbf{pq}}\gamma_{\mathbf{p}}\gamma_{\mathbf{q}}, \tag{F.1.1}$$

where $p = (\mathbf{r},\beta)$ and $q = (\mathbf{r}',\beta')$ ($\beta,\beta' = A,B$) are combined indices and $\mathscr{H}$ is a $2N \times 2N$ real skew-symmetric matrix with N being the number of lattice sites.

By locally and adiabatically tuning μ along a T-junction path, MSFs can be braided. During this

process, the Majorana operators evolve according to the following equation in the Heisenberg picture [304]:

$$\gamma_{\mathbf{p}} \to \gamma_{\mathbf{p}}(t) = U\gamma_{\mathbf{p}}(0)U^{\dagger} = \sum_{\mathbf{q}} \mathscr{O}_{\mathbf{qp}}\gamma_{\mathbf{q}}(0)\,, \tag{F.1.2}$$

where $U = \mathscr{T}\exp[i\int_0^t H(\tau)d\tau]$ and $\mathscr{O} = \mathscr{T}\exp[-i\int_0^t \mathscr{H}(\tau)d\tau]$ is an element of the special orthogonal group $\mathscr{O} \in \mathrm{SO}(2N)$; $\mathscr{T}$ is the time-ordering operator.

In our numerical simulation, we first diagonalize $\mathscr{H}$ at time $t = 0$ to obtain the zero-energy eigenmodes $\gamma_i(0) = \sum_{\mathbf{p}} \eta_{i\mathbf{p}}\gamma_{\mathbf{p}}(0)$, where the coefficients $\eta_{i\mathbf{p}}$ represent the mode function and are localized at the ends of the line defects. During the braiding process, the zero-energy eigen modes evolve as $\gamma_i(t) = U\gamma_i(0)U^{\dagger} = \sum_{\mathbf{p}} \eta_{i\mathbf{p}}\gamma_{\mathbf{p}}(t)$, where $\gamma_{\mathbf{p}}(t)$ are calculated via Eq. (F.1.2). Using this method, we obtain the time evolution of the zero-energy MSF modes with the results plotted in the main text.

F.2 Majorana correlation functions

To calculate the Majorana correlations, we use the method introduced in Ref. [305]. Let us define the density operator $\rho = N\exp(-\beta H)$ (N is the normalization constant and β is the inverse temperature) and the antisymmetric covariance matrix Γ with elements $\Gamma_{\mathbf{pq}} = \frac{i}{2}\mathrm{Tr}[\rho(\gamma_{\mathbf{p}}\gamma_{\mathbf{q}} - \gamma_{\mathbf{q}}\gamma_{\mathbf{p}})]$. The Hamiltonian H can be brought into block off-diagonal form $OHO^{\mathrm{T}} = \oplus_{j=1}^{N}\begin{pmatrix} 0 & -\varepsilon_j \\ \varepsilon_j & 0 \end{pmatrix}$ by a special orthogonal matrix $O \in \mathrm{SO}(2N)$, where ε_j characterizes the energy eigen-spectrum of the Hamiltonian. This matrix O also reduces Γ to a block off-diagonal form $O\Gamma O^{\mathrm{T}} = \oplus_{j=1}^{N}\begin{pmatrix} 0 & \eta_j \\ -\eta_j & 0 \end{pmatrix}$ with $\eta_j = \tanh(\beta\varepsilon_j/2)$. The covariance matrix Γ_{G} corresponding to the ground state of H is obtained by letting the inverse temperature $\beta \to \infty$, i.e., $\eta_j \to \mathrm{sgn}(\varepsilon_j)$. After we obtain Γ_{G}, the

Majorana correlations can be computed by Wick's theorem via the equation:

$$i\langle \gamma_{\mathbf{p}} \gamma_{\mathbf{q}} \rangle = \mathrm{Pf}(\Gamma_{\mathrm{G}}^{'}), \tag{F.2.1}$$

where $\Gamma_{\mathrm{G}}^{'} = \begin{pmatrix} (\Gamma_{\mathrm{G}})_{\mathbf{pp}} & (\Gamma_{\mathrm{G}})_{\mathbf{pq}} \\ (\Gamma_{\mathrm{G}})_{\mathbf{qp}} & (\Gamma_{\mathrm{G}})_{\mathbf{qq}} \end{pmatrix}$ is a 2×2 submatrix of Γ_{G} and $\mathrm{Pf}(\Gamma_{\mathrm{G}}^{'})$ is the Pfaffian of $\Gamma_{\mathrm{G}}^{'}$ with $\mathrm{Pf}(\Gamma_{\mathrm{G}}^{'})^2 = \det(\Gamma_{\mathrm{G}}^{'})$. Once we have obtained $i\langle \gamma_{\mathbf{p}} \gamma_{\mathbf{q}} \rangle$ at time $t = 0$, the time evolution of the MSF mode correlations $i\langle \gamma_i \gamma_j \rangle_t$ can be computed directly using $\gamma_i(t) = \sum_{\mathbf{p}} \eta_{i\mathbf{p}} \gamma_{\mathbf{p}}(t) = \sum_{\mathbf{p},\mathbf{q}} \eta_{i\mathbf{p}} \mathscr{O}_{\mathbf{qp}} \gamma_{\mathbf{q}}(0)$.

BIBLIOGRAPHY

Bibliography

[1] L. D. Landau and E. M. Lifshitz, *Statistical Physics. Part 1: Course of Theoretical Physics*. Pergamon Press, Oxford, 1980.

[2] P. W. Anderson, *Basic notions of condensed matter physics*, vol. 55. Westview Press, Bolder, CO, 1997.

[3] S. Sachdev, "Quantum phase transitions," *Quantum Phase Transitions, by Subir Sachdev, Cambridge, UK: Cambridge University Press, 2011*, vol. 1, 2011.

[4] J. G. Bednorz and K. A. Müller, "Possible high t_c superconductivity in the ba-la-cu-o system," *Zeitschrift für Physik B Condensed Matter*, vol. 64, no. 2, pp. 189–193, 1986.

[5] D. C. Tsui, H. L. Stormer, and A. C. Gossard, "Two-dimensional magnetotransport in the extreme quantum limit," *Phys. Rev. Lett.*, vol. 48, pp. 1559–1562, May 1982.

[6] K. von Klitzing, "The quantized hall effect," *Rev. Mod. Phys.*, vol. 58, no. 3, 1986.

[7] X.-L. Qi and S.-C. Zhang, "Topological insulators and superconductors," *Rev. Mod. Phys.*, vol. 83, pp. 1057–1110, Oct 2011.

[8] M. Z. Hasan and C. L. Kane, "Colloquium: Topological insulators," *Rev. Mod. Phys.*, vol. 82, pp. 3045–3067, Nov 2010.

[9] J. E. Moore, "The birth of topological insulators," *Nature*, vol. 464, no. 7286, pp. 194–198, 2010.

[10] B. A. Bernevig, T. L. Hughes, and S.-C. Zhang, "Quantum spin hall effect and topological phase transition in hgte quantum wells," *Science*, vol. 314, no. 5806, pp. 1757–1761, 2006.

[11] L. Fu, C. L. Kane, and E. J. Mele, "Topological insulators in three dimensions," *Phys. Rev. Lett.*, vol. 98, p. 106803, Mar 2007.

[12] C. L. Kane and E. J. Mele, "Z_2 topological order and the quantum spin hall effect," *Phys. Rev. Lett.*, vol. 95, p. 146802, Sep 2005.

[13] C. Kane and E. Mele, "Quantum spin hall effect in graphene," *Phys. Rev. Lett.*, vol. 95, no. 22, p. 226801, 2005.

[14] M. König, S. Wiedmann, C. Brüne, A. Roth, H. Buhmann, L. W. Molenkamp, X.-L. Qi, and S.-C. Zhang, "Quantum spin hall insulator state in hgte quantum wells," *Science*, vol. 318, no. 5851, pp. 766–770, 2007.

[15] A. Roth, C. Brüne, H. Buhmann, L. W. Molenkamp, J. Maciejko, X.-L. Qi, and S.-C. Zhang, "Nonlocal transport in the quantum spin hall state," *Science*, vol. 325, no. 5938, pp. 294–297, 2009.

[16] D. Hsieh, D. Qian, L. Wray, Y. Xia, Y. S. Hor, R. Cava, and M. Z. Hasan, "A topological dirac insulator in a quantum spin hall phase," *Nature*, vol. 452, no. 7190, pp. 970–974, 2008.

[17] X. Chen, Z.-C. Gu, Z.-X. Liu, and X.-G. Wen, "Symmetry-protected topological orders in interacting bosonic systems," *Science*, vol. 338, no. 6114, pp. 1604–1606, 2012.

[18] X. Chen, Z.-C. Gu, Z.-X. Liu, and X.-G. Wen, "Symmetry protected topological orders and the group cohomology of their symmetry group," *Phys. Rev. B*, vol. 87, no. 15, p. 155114, 2013.

[19] A. Kitaev, "Periodic table for topological insulators and superconductors," *AIP Conf. Proc.*, vol. 1134, p. 22, 2009.

[20] A. P. Schnyder, S. Ryu, A. Furusaki, and A. W. W. Ludwig, "Classification of topological insulators and superconductors in three spatial dimensions," *Phys. Rev. B*, vol. 78, p. 195125, Nov 2008.

[21] S. Ryu, A. P. Schnyder, A. Furusaki, and A. W. Ludwig, "Topological insulators and superconductors: tenfold way and dimensional hierarchy," *New J. Phys.*, vol. 12, no. 6, p. 065010, 2010.

[22] D.-L. Deng, S.-T. Wang, and L.-M. Duan, "Systematic construction of tight-binding hamiltonians for topological insulators and superconductors," *Phys. Rev. B*, vol. 89, p. 075126, Feb 2014.

[23] D.-L. Deng, S.-T. Wang, C. Shen, and L.-M. Duan, "Hopf insulators and their topologically protected surface states," *Phys. Rev. B*, vol. 88, no. 20, p. 201105, 2013.

[24] S.-T. Wang, D.-L. Deng, and L.-M. Duan, "Probe of three-dimensional chiral topological insulators in an optical lattice," *Phys. Rev. Lett.*, vol. 113, p. 033002, Jul 2014.

[25] D.-L. Deng, S.-T. Wang, and L.-M. Duan, "Direct probe of topological order for cold atoms," *Phys. Rev. A*, vol. 90, p. 041601, Oct 2014.

[26] D.-L. Deng, S.-T. Wang, K. Sun, and L.-M. Duan, "An experimental proposal to observe non-abelian statistics of majorana-shockley fermions in an optical lattice," *arXiv preprint arXiv:1408.5653*, 2014.

[27] D.-L. Deng and L.-M. Duan, "Fault-tolerant quantum random-number generator certified by majorana fermions," *Phys. Rev. A*, vol. 88, p. 012323, Jul 2013.

[28] X.-L. Qi and S.-C. Zhang, "The quantum spin hall effect and topological insulators," *Phys. Today*, vol. 63, no. 1, pp. 33–38, 2010.

[29] M. Z. Hasan and J. E. Moore, "Three-dimensional topological insulators," *Ann. Rev. Condens. Matter Phys.*, vol. 2, pp. 55–78, 2011.

[30] D. Hsieh, Y. Xia, L. Wray, D. Qian, A. Pal, J. Dil, J. Osterwalder, F. Meier, G. Bihlmayer, C. Kane, *et al.*, "Observation of unconventional quantum spin textures in topological insulators," *Science*, vol. 323, no. 5916, pp. 919–922, 2009.

[31] D. Hsieh, Y. Xia, D. Qian, L. Wray, J. Dil, F. Meier, J. Osterwalder, L. Patthey, J. Checkelsky, N. Ong, *et al.*, "A tunable topological insulator in the spin helical dirac transport regime," *Nature*, vol. 460, no. 7259, pp. 1101–1105, 2009.

[32] T. H. Hsieh and L. Fu, "Majorana fermions and exotic surface andreev bound states in topological superconductors: Application to $Cu_xBi_2Se_3$," *Phys. Rev. Lett.*, vol. 108, p. 107005, Mar 2012.

[33] Y. Xia, D. Qian, D. Hsieh, L. Wray, A. Pal, H. Lin, A. Bansil, D. Grauer, Y. Hor, R. Cava, *et al.*, "Observation of a large-gap topological-insulator class with a single dirac cone on the surface," *Nature Physics*, vol. 5, no. 6, pp. 398–402, 2009.

[34] Y. Chen, J. Analytis, J.-H. Chu, Z. Liu, S.-K. Mo, X.-L. Qi, H. Zhang, D. Lu, X. Dai, Z. Fang, *et al.*, "Experimental realization of a three-dimensional topological insulator, bi2te3," *Science*, vol. 325, no. 5937, pp. 178–181, 2009.

[35] P. Roushan, J. Seo, C. V. Parker, Y. Hor, D. Hsieh, D. Qian, A. Richardella, M. Z. Hasan, R. Cava, and A. Yazdani, "Topological surface states protected from backscattering by chiral spin texture," *Nature*, vol. 460, no. 7259, pp. 1106–1109, 2009.

[36] R. Roy, "Topological phases and the quantum spin hall effect in three dimensions," *Phys. Rev. B*, vol. 79, no. 19, p. 195322, 2009.

[37] L. Fu and C. L. Kane, "Superconducting proximity effect and majorana fermions at the surface of a topological insulator," *Phys. Rev. Lett.*, vol. 100, p. 096407, Mar 2008.

[38] L. Fu and E. Berg, "Odd-parity topological superconductors: Theory and application to $Cu_xBi_2Se_3$," *Phys. Rev. Lett.*, vol. 105, p. 097001, Aug 2010.

[39] L. Fu, "Topological crystalline insulators," *Phys. Rev. Lett.*, vol. 106, no. 10, p. 106802, 2011.

[40] J. E. Moore and L. Balents, "Topological invariants of time-reversal-invariant band structures," *Phys. Rev. B*, vol. 75, p. 121306, Mar 2007.

[41] J. E. Moore, Y. Ran, and X.-G. Wen, "Topological surface states in three-dimensional magnetic insulators," *Phys. Rev. Lett.*, vol. 101, no. 18, p. 186805, 2008.

[42] J. Moore, "Topological insulators: The next generation," *Nat. Phys.*, vol. 5, no. 6, pp. 378–380, 2009.

[43] V. Mourik, K. Zuo, S. Frolov, S. Plissard, E. Bakkers, and L. Kouwenhoven, "Signatures of majorana fermions in hybrid superconductor-semiconductor nanowire devices," *Science*, vol. 336, no. 6084, pp. 1003–1007, 2012.

[44] S. Nadj-Perge, I. K. Drozdov, J. Li, H. Chen, S. Jeon, J. Seo, A. H. MacDonald, B. A. Bernevig, and A. Yazdani, "Observation of majorana fermions in ferromagnetic atomic chains on a superconductor," *Science*, vol. 346, no. 6209, pp. 602–607, 2014.

[45] X.-L. Qi, T. L. Hughes, and S.-C. Zhang, "Topological field theory of time-reversal invariant insulators," *Phys. Rev. B*, vol. 78, p. 195424, Nov 2008.

[46] I. Affleck, T. Kennedy, E. H. Lieb, and H. Tasaki, "Valence bond ground states in isotropic quantum antiferromagnets," *Comm. Math. Phys.*, vol. 115, no. 3, pp. 477–528, 1988.

[47] F. D. M. Haldane, "Continuum dynamics of the 1-d heisenberg antiferromagnet: identification with the o(3) nonlinear sigma model," *Phys. Lett. A*, vol. 93, no. 9, pp. 464–468, 1983.

[48] M. Nakahara, *Geometry, topology, and physics*. CRC Press, 2003.

[49] Z.-C. Gu and X.-G. Wen, "Symmetry-protected topological orders for interacting fermions: Fermionic topological nonlinear σ models and a special group supercohomology theory," *Phys. Rev. B*, vol. 90, p. 115141, Sep 2014.

[50] Y.-M. Lu and A. Vishwanath, "Theory and classification of interacting integer topological phases in two dimensions: A chern-simons approach," *Phys. Rev. B*, vol. 86, p. 125119, Sep 2012.

[51] R. B. Laughlin, "Anomalous quantum hall effect: An incompressible quantum fluid with fractionally charged excitations," *Phys. Rev. Lett.*, vol. 50, pp. 1395–1398, May 1983.

[52] X. G. Wen, F. Wilczek, and A. Zee, "Chiral spin states and superconductivity," *Phys. Rev. B*, vol. 39, pp. 11413–11423, Jun 1989.

[53] X. G. Wen, "Mean-field theory of spin-liquid states with finite energy gap and topological orders," *Phys. Rev. B*, vol. 44, pp. 2664–2672, Aug 1991.

[54] V. Kalmeyer and R. B. Laughlin, "Equivalence of the resonating-valence-bond and fractional quantum hall states," *Phys. Rev. Lett.*, vol. 59, pp. 2095–2098, Nov 1987.

[55] N. Read and S. Sachdev, "Large-n expansion for frustrated quantum antiferromagnets," *Phys. Rev. Lett.*, vol. 66, pp. 1773–1776, Apr 1991.

[56] R. Moessner and S. L. Sondhi, "Resonating valence bond phase in the triangular lattice quantum dimer model," *Phys. Rev. Lett.*, vol. 86, pp. 1881–1884, Feb 2001.

[57] C. Nayak, S. H. Simon, A. Stern, M. Freedman, and S. Das Sarma, "Non-abelian anyons and topological quantum computation," *Rev. Mod. Phys.*, vol. 80, pp. 1083–1159, Sep 2008.

[58] X.-G. Wen, "Quantum orders and symmetric spin liquids," *Phys. Rev. B*, vol. 65, p. 165113, Apr 2002.

[59] S.-P. Kou, M. Levin, and X.-G. Wen, "Mutual chern-simons theory for Z_2 topological order," *Phys. Rev. B*, vol. 78, p. 155134, Oct 2008.

[60] S.-P. Kou and X.-G. Wen, "Translation-symmetry-protected topological orders in quantum spin systems," *Phys. Rev. B*, vol. 80, p. 224406, Dec 2009.

[61] M. Levin and A. Stern, "Fractional topological insulators," *Phys. Rev. Lett.*, vol. 103, p. 196803, Nov 2009.

[62] X.-G. Wen, "Quantum order from string-net condensations and the origin of light and massless fermions," *Phys. Rev. D*, vol. 68, p. 065003, Sep 2003.

[63] A. Mesaros and Y. Ran, "Classification of symmetry enriched topological phases with exactly solvable models," *Phys. Rev. B*, vol. 87, p. 155115, Apr 2013.

[64] J. C. Wang, Z.-C. Gu, and X.-G. Wen, "Field-theory representation of gauge-gravity symmetry-protected topological invariants, group cohomology, and beyond," *Phys. Rev. Lett.*, vol. 114, p. 031601, Jan 2015.

[65] A. Kapustin, "Bosonic topological insulators and paramagnets: a view from cobordisms," *arXiv preprint arXiv:1404.6659*, 2014.

[66] A. Kapustin, "Symmetry protected topological phases, anomalies, and cobordisms: Beyond group cohomology," *arXiv preprint arXiv:1403.1467*, 2014.

[67] C. Wang, A. C. Potter, and T. Senthil, "Classification of interacting electronic topological insulators in three dimensions," *Science*, vol. 343, no. 6171, pp. 629–631, 2014.

[68] A. Altland and M. R. Zirnbauer, "Nonstandard symmetry classes in mesoscopic normal-superconducting hybrid structures," *Phys. Rev. B*, vol. 55, no. 2, p. 1142, 1997.

[69] A. Y. Kitaev, "Fault-tolerant quantum computation by anyons," *Ann. Phys.*, vol. 303, no. 1, pp. 2–30, 2003.

[70] S. D. Sarma and A. Pinczuk, *Perspectives in quantum Hall effects*. John Wiley & Sons, 2008.

[71] N. Read and D. Green, "Paired states of fermions in two dimensions with breaking of parity and time-reversal symmetries and the fractional quantum hall effect," *Phys. Rev. B*, vol. 61, pp. 10267–10297, Apr 2000.

[72] I. Bloch, J. Dalibard, and S. Nascimbène, "Quantum simulations with ultracold quantum gases," *Nat. Phys.*, vol. 8, no. 4, pp. 267–276, 2012.

[73] X.-L. Qi, T. L. Hughes, S. Raghu, and S.-C. Zhang, "Time-reversal-invariant topological superconductors and superfluids in two and three dimensions," *Phys. Rev. Lett.*, vol. 102, no. 18, p. 187001, 2009.

[74] R. Roy, "Topological superfluids with time reversal symmetry," *arXiv preprint arXiv:0803.2868*, 2008.

[75] Y. Li and C. Wu, "High-dimensional topological insulators with quaternionic analytic landau levels," *Phys. Rev. Lett.*, vol. 110, p. 216802, May 2013.

[76] Y. Li, K. Intriligator, Y. Yu, and C. Wu, "Isotropic landau levels of dirac fermions in high dimensions," *Phys. Rev. B*, vol. 85, p. 085132, Feb 2012.

[77] A. P. Schnyder, S. Ryu, and A. W. Ludwig, "Lattice model of a three-dimensional topological singlet superconductor with time-reversal symmetry," *Phys. Rev. Lett.*, vol. 102, no. 19, p. 196804, 2009.

[78] B. Yan, C.-X. Liu, H.-J. Zhang, C.-Y. Yam, X.-L. Qi, T. Frauenheim, and S.-C. Zhang, "Theoretical prediction of topological insulators in thallium-based iii-v-vi2 ternary chalcogenides," *EPL (Europhy. Lett.)*, vol. 90, no. 3, p. 37002, 2010.

[79] M. Sato, "Topological odd-parity superconductors," *Phys. Rev. B*, vol. 81, p. 220504, Jun 2010.

[80] T. Neupert, L. Santos, S. Ryu, C. Chamon, and C. Mudry, "Noncommutative geometry for three-dimensional topological insulators," *Phys. Rev. B*, vol. 86, no. 3, p. 035125, 2012.

[81] J. H. Whitehead, "An expression of hopf's invariant as an integral," *Proc. Nat. Acad. Sci.*, vol. 33, no. 5, p. 117, 1947.

[82] J. C. Budich, "Charge conservation protected topological phases," *Phys. Rev. B*, vol. 87, p. 161103, Apr 2013.

[83] R. H. Fox, "Homotopy groups and torus homotopy groups," *Annals of Mathematics*, pp. 471–510, 1948.

[84] L. S. Pontryagin, "Characteristic cycles on differentiable manifolds," *Matematicheskii Sbornik*, vol. 63, no. 2, pp. 233–284, 1947.

[85] F. Wilczek and A. Zee, "Linking numbers, spin, and statistics of solitons," *Phys. Rev. Lett.*, vol. 51, pp. 2250–2252, Dec 1983.

[86] K. v. Klitzing, G. Dorda, and M. Pepper, "New method for high-accuracy determination of the fine-structure constant based on quantized hall resistance," *Phys. Rev. Lett.*, vol. 45, no. 6, pp. 494–497, 1980.

[87] T. Neupert, L. Santos, S. Ryu, C. Chamon, and C. Mudry, "Topological hubbard model and its high-temperature quantum hall effect," *Phys. Rev. Lett.*, vol. 108, p. 046806, Jan 2012.

[88] J. Dalibard, F. Gerbier, G. Juzeliūnas, and P. Öhberg, "Colloquium: Artificial gauge potentials for neutral atoms," *Rev. Mod. Phys.*, vol. 83, pp. 1523–1543, Nov 2011.

[89] Y.-J. Lin, K. Jimenez-Garcia, and I. Spielman, "Spin-orbit-coupled bose-einstein condensates," *Nature*, vol. 471, no. 7336, pp. 83–86, 2011.

[90] A. Micheli, G. Brennen, and P. Zoller, "A toolbox for lattice-spin models with polar molecules," *Nature Physics*, vol. 2, no. 5, pp. 341–347, 2006.

[91] N. Y. Yao, A. V. Gorshkov, C. R. Laumann, A. M. Läuchli, J. Ye, and M. D. Lukin, "Realizing fractional chern insulators in dipolar spin systems," *Phys. Rev. Lett.*, vol. 110, p. 185302, Apr 2013.

[92] A. Chotia, B. Neyenhuis, S. A. Moses, B. Yan, J. P. Covey, M. Foss-Feig, A. M. Rey, D. S. Jin, and J. Ye, "Long-lived dipolar molecules and feshbach molecules in a 3d optical lattice," *Phys. Rev. Lett.*, vol. 108, p. 080405, Feb 2012.

[93] T. Kitagawa, M. A. Broome, A. Fedrizzi, M. S. Rudner, E. Berg, I. Kassal, A. Aspuru-Guzik, E. Demler, and A. G. White, "Observation of topologically protected bound states in photonic quantum walks," *Nature communications*, vol. 3, p. 882, 2012.

[94] M. Karski, L. Förster, J.-M. Choi, A. Steffen, W. Alt, D. Meschede, and A. Widera, "Quantum walk in position space with single optically trapped atoms," *Science*, vol. 325, no. 5937, pp. 174–177, 2009.

[95] M. A. Broome, A. Fedrizzi, B. P. Lanyon, I. Kassal, A. Aspuru-Guzik, and A. G. White, "Discrete single-photon quantum walks with tunable decoherence," *Phys. Rev. Lett.*, vol. 104, p. 153602, Apr 2010.

[96] T. Kitagawa, "Topological phenomena in quantum walks: elementary introduction to the physics of topological phases," *Quantum Information Processing*, vol. 11, no. 5, pp. 1107–1148, 2012.

[97] A. Hatcher, *Algebraic Topology*. Cambridge University Press, 2002.

[98] S.-C. Zhang and J. Hu, "A four-dimensional generalization of the quantum hall effect," *Science*, vol. 294, no. 5543, pp. 823–828, 2001.

[99] A. M. Essin and V. Gurarie, "Antiferromagnetic topological insulators in cold atomic gases," *Phys. Rev. B*, vol. 85, no. 19, p. 195116, 2012.

[100] P. Hosur, S. Ryu, and A. Vishwanath, "Chiral topological insulators, superconductors, and other competing orders in three dimensions," *Phys. Rev. B*, vol. 81, p. 045120, Jan. 2010.

[101] D. Jaksch and P. Zoller, "Creation of effective magnetic fields in optical lattices: the hofstadter butterfly for cold neutral atoms," *New J. Phys.*, vol. 5, no. 1, p. 56, 2003.

[102] H. Miyake, G. A. Siviloglou, C. J. Kennedy, W. C. Burton, and W. Ketterle, "Realizing the harper hamiltonian with laser-assisted tunneling in optical lattices," *Phys. Rev. Lett.*, vol. 111, p. 185302, Oct 2013.

[103] M. Aidelsburger, M. Atala, M. Lohse, J. T. Barreiro, B. Paredes, and I. Bloch, "Realization of the hofstadter hamiltonian with ultracold atoms in optical lattices," *Phys. Rev. Lett.*, vol. 111, p. 185301, Oct 2013.

[104] C. Chin, R. Grimm, P. Julienne, and E. Tiesinga, "Feshbach resonances in ultracold gases," *Rev. Mod. Phys.*, vol. 82, pp. 1225–1286, Apr 2010.

[105] G.-B. Jo, J. Guzman, C. K. Thomas, P. Hosur, A. Vishwanath, and D. M. Stamper-Kurn, "Ultracold atoms in a tunable optical kagome lattice," *Phys. Rev. Lett.*, vol. 108, no. 4, p. 045305, 2012.

[106] E. Tang, J.-W. Mei, and X.-G. Wen, "High-temperature fractional quantum hall states," *Phys. Rev. Lett.*, vol. 106, no. 23, p. 236802, 2011.

[107] T. Neupert, L. Santos, C. Chamon, and C. Mudry, "Fractional quantum hall states at zero magnetic field," *Phys. Rev. Lett.*, vol. 106, no. 23, p. 236804, 2011.

[108] K. Sun, Z. Gu, H. Katsura, and S. DasSarma, "Nearly flatbands with nontrivial topology," *Phys. Rev. Lett.*, vol. 106, no. 23, p. 236803, 2011.

[109] I. B. Spielman, W. D. Phillips, and J. V. Porto, "Mott-insulator transition in a two-dimensional atomic bose gas," *Phys. Rev. Lett.*, vol. 98, p. 080404, Feb 2007.

[110] V. A. Kashurnikov, N. V. Prokof'ev, and B. V. Svistunov, "Revealing the superfluid–mott-insulator transition in an optical lattice," *Phys. Rev. A*, vol. 66, p. 031601, Sep 2002.

[111] M. Köhl, H. Moritz, T. Stöferle, K. Günter, and T. Esslinger, "Fermionic atoms in a three dimensional optical lattice: Observing fermi surfaces, dynamics, and interactions," *Phys. Rev. Lett.*, vol. 94, no. 8, p. 080403, 2005.

[112] D. M. Stamper-Kurn, A. P. Chikkatur, A. Görlitz, S. Inouye, S. Gupta, D. E. Pritchard, and W. Ketterle, "Excitation of phonons in a bose-einstein condensate by light scattering," *Phys. Rev. Lett.*, vol. 83, no. 15, p. 2876, 1999.

[113] S.-L. Zhu, B. Wang, and L.-M. Duan, "Simulation and detection of dirac fermions with cold atoms in an optical lattice," *Phys. Rev. Lett.*, vol. 98, no. 26, p. 260402, 2007.

[114] U. Schneider, L. Hackermüller, S. Will, T. Best, I. Bloch, T. A. Costi, R. W. Helmes, D. Rasch, and A. Rosch, "Metallic and insulating phases of repulsively interacting fermions in a 3d optical lattice," *Science*, vol. 322, no. 5907, pp. 1520–1525, 2008.

[115] X.-J. Liu, K. T. Law, and T. K. Ng, "Realization of 2d spin-orbit interaction and exotic topological orders in cold atoms," *Phys. Rev. Lett.*, vol. 112, p. 086401, 2014.

[116] P. Wang, Z.-Q. Yu, Z. Fu, J. Miao, L. Huang, S. Chai, H. Zhai, and J. Zhang, "Spin-orbit coupled degenerate fermi gases," *Phys. Rev. Lett.*, vol. 109, no. 9, p. 095301, 2012.

[117] D.-W. Zhang, C.-J. Shan, F. Mei, M. Yang, R.-Q. Wang, and S.-L. Zhu, "Valley-dependent gauge fields for ultracold atoms in square optical superlattices," *Phys. Rev. A*, vol. 89, p. 015601, Jan 2014.

[118] J. K. Pachos, E. Alba, V. Lahtinen, and J. J. Garcia-Ripoll, "Seeing majorana fermions in time-of-flight images of staggered spinless fermions coupled by *s*-wave pairing," *Phys. Rev. A*, vol. 88, p. 013622, Jul 2013.

[119] A. E. Leanhardt, T. A. Pasquini, M. Saba, A. Schirotzek, Y. Shin, D. Kielpinski, D. E. Pritchard, and W. Ketterle, "Cooling bose-einstein condensates below 500 picokelvin," *Science*, vol. 301, no. 5639, pp. 1513–1515, 2003.

[120] P. Medley, D. M. Weld, H. Miyake, D. E. Pritchard, and W. Ketterle, "Spin gradient demagnetization cooling of ultracold atoms," *Phys. Rev. Lett.*, vol. 106, p. 195301, May 2011.

[121] I. Bloch, "Ultracold quantum gases in optical lattices," *Nat. Phys.*, vol. 1, no. 1, pp. 23–30, 2005.

[122] D. J. Thouless, M. Kohmoto, M. P. Nightingale, and M. den Nijs, "Quantized hall conductance in a two-dimensional periodic potential," *Phys. Rev. Lett.*, vol. 49, pp. 405–408, Aug 1982.

[123] Y.-J. Lin, R. L. Compton, K. Jimenez-Garcia, J. V. Porto, and I. B. Spielman, "Synthetic magnetic fields for ultracold neutral atoms," *Nature*, vol. 462, no. 7273, pp. 628–632, 2009.

[124] X.-J. Liu, M. F. Borunda, X. Liu, and J. Sinova, "Effect of induced spin-orbit coupling for atoms via laser fields," *Phys. Rev. Lett.*, vol. 102, no. 4, p. 046402, 2009.

[125] L. W. Cheuk, A. T. Sommer, Z. Hadzibabic, T. Yefsah, W. S. Bakr, and M. W. Zwierlein, "Spin-injection spectroscopy of a spin-orbit coupled fermi gas," *Phys. Rev. Lett.*, vol. 109, no. 9, p. 095302, 2012.

[126] V. Galitski and I. B. Spielman, "Spin-orbit coupling in quantum gases," *Nature*, vol. 494, no. 7435, pp. 49–54, 2013.

[127] M. Lewenstein, A. Sanpera, V. Ahufinger, B. Damski, A. Sen, and U. Sen, "Ultracold atomic gases in optical lattices: mimicking condensed matter physics and beyond," *Adv. Phys.*, vol. 56, no. 2, pp. 243–379, 2007.

[128] S.-L. Zhu, H. Fu, C.-J. Wu, S.-C. Zhang, and L.-M. Duan, "Spin hall effects for cold atoms in a light-induced gauge potential," *Phys. Rev. Lett.*, vol. 97, no. 24, p. 240401, 2006.

[129] S.-L. Zhu, L.-B. Shao, Z. D. Wang, and L.-M. Duan, "Probing non-abelian statistics of majorana fermions in ultracold atomic superfluid," *Phys. Rev. Lett.*, vol. 106, p. 100404, Mar 2011.

[130] B. Béri and N. Cooper, "Z_ {2} topological insulators in ultracold atomic gases," *Phys. Rev. Lett.*, vol. 107, no. 14, p. 145301, 2011.

[131] C.-Z. Chang, J. Zhang, X. Feng, J. Shen, Z. Zhang, M. Guo, K. Li, Y. Ou, P. Wei, L.-L. Wang, *et al.*, "Experimental observation of the quantum anomalous hall effect in a magnetic topological insulator," *Science*, vol. 340, no. 6129, pp. 167–170, 2013.

[132] J.-P. Brantut, J. Meineke, D. Stadler, S. Krinner, and T. Esslinger, "Conduction of ultracold fermions through a mesoscopic channel," *Science*, vol. 337, no. 6098, pp. 1069–1071, 2012.

[133] L. B. Shao, S.-L. Zhu, L. Sheng, D. Y. Xing, and Z. D. Wang, "Realizing and detecting the quantum hall effect without landau levels by using ultracold atoms," *Phys. Rev. Lett.*, vol. 101, p. 246810, Dec 2008.

[134] A. Dauphin and N. Goldman, "Extracting the chern number from the dynamics of a fermi gas: Implementing a quantum hall bar for cold atoms," *Phys. Rev. Lett.*, vol. 111, p. 135302, Sep 2013.

[135] L. Wang, A. A. Soluyanov, and M. Troyer, "Proposal for direct measurement of topological invariants in optical lattices," *Phys. Rev. Lett.*, vol. 110, p. 166802, Apr 2013.

[136] X.-J. Liu, X. Liu, C. Wu, and J. Sinova, "Quantum anomalous hall effect with cold atoms trapped in a square lattice," *Phys. Rev. A*, vol. 81, p. 033622, Mar 2010.

[137] N. Goldman, J. Beugnon, and F. Gerbier, "Detecting chiral edge states in the hofstadter optical lattice," *Phys. Rev. Lett.*, vol. 108, p. 255303, Jun 2012.

[138] H. M. Price and N. R. Cooper, "Mapping the berry curvature from semiclassical dynamics in optical lattices," *Phys. Rev. A*, vol. 85, p. 033620, Mar 2012.

[139] X.-J. Liu, K. T. Law, T. K. Ng, and P. A. Lee, "Detecting topological phases in cold atoms," *Phys. Rev. Lett.*, vol. 111, p. 120402, Sep 2013.

[140] D. A. Abanin, T. Kitagawa, I. Bloch, and E. Demler, "Interferometric approach to measuring band topology in 2d optical lattices," *Phys. Rev. Lett.*, vol. 110, p. 165304, Apr 2013.

[141] M. Atala, M. Aidelsburger, J. T. Barreiro, D. Abanin, T. Kitagawa, E. Demler, and I. Bloch, "Direct measurement of the zak phase in topological bloch bands," *Nat. Phys.*, vol. 9, no. 16, pp. 795–800, 2013.

[142] E. Alba, X. Fernandez-Gonzalvo, J. Mur-Petit, J. K. Pachos, and J. J. Garcia-Ripoll, "Seeing topological order in time-of-flight measurements," *Phys. Rev. Lett.*, vol. 107, p. 235301, Nov 2011.

[143] W. P. Su, J. R. Schrieffer, and A. J. Heeger, "Solitons in polyacetylene," *Phys. Rev. Lett.*, vol. 42, pp. 1698–1701, Jun 1979.

[144] A. J. Heeger, S. Kivelson, J. R. Schrieffer, and W. P. Su, "Solitons in conducting polymers," *Rev. Mod. Phys.*, vol. 60, pp. 781–850, Jul 1988.

[145] T. Fukui, Y. Hatsugai, and H. Suzuki, "Chern numbers in discretized brillouin zone: Efficient method of computing (spin) hall conductances," *J. Phys. Soc. Jpn.*, vol. 74, no. 6, pp. 1674–1677, 2005.

[146] F. Haldane, "Model for a quantum hall effect without landau levels: Condensed-matter realization of the "parity anomaly"," *Phys. Rev. Lett.*, vol. 61, no. 18, pp. 2015–2018, 1988.

[147] X. Zhang, H. Zhang, J. Wang, C. Felser, and S.-C. Zhang, "Actinide topological insulator materials with strong interaction," *Science*, vol. 335, no. 6075, pp. 1464–1466, 2012.

[148] S. Raghu, X.-L. Qi, C. Honerkamp, and S.-C. Zhang, "Topological mott insulators," *Phys. Rev. Lett.*, vol. 100, p. 156401, Apr 2008.

[149] L. Fidkowski and A. Kitaev, "Effects of interactions on the topological classification of free fermion systems," *Phys. Rev. B*, vol. 81, p. 134509, Apr 2010.

[150] M. Hohenadler, T. C. Lang, and F. F. Assaad, "Correlation effects in quantum spin-hall insulators: A quantum monte carlo study," *Phys. Rev. Lett.*, vol. 106, p. 100403, Mar 2011.

[151] D. Sheng, Z.-C. Gu, K. Sun, and L. Sheng, "Fractional quantum hall effect in the absence of landau levels," *Nat. Commun.*, vol. 2, p. 389, 2011.

[152] J. Maciejko, X.-L. Qi, A. Karch, and S.-C. Zhang, "Fractional topological insulators in three dimensions," *Phys. Rev. Lett.*, vol. 105, p. 246809, Dec 2010.

[153] A. Go, W. Witczak-Krempa, G. S. Jeon, K. Park, and Y. B. Kim, "Correlation effects on 3d topological phases: From bulk to boundary," *Phys. Rev. Lett.*, vol. 109, p. 066401, Aug 2012.

[154] S.-L. Zhu, Z.-D. Wang, Y.-H. Chan, and L.-M. Duan, "Topological bose-mott insulators in a one-dimensional optical superlattice," *Phys. Rev. Lett.*, vol. 110, p. 075303, Feb 2013.

[155] R. P. Feynman, "Simulating physics with computers," *Int. J. Theor. Phys.*, vol. 21, no. 6, pp. 467–488, 1982.

[156] J. F. Sherson, C. Weitenberg, M. Endres, M. Cheneau, I. Bloch, and S. Kuhr, "Single-atom-resolved fluorescence imaging of an atomic mott insulator," *Nature*, vol. 467, no. 7311, pp. 68–72, 2010.

[157] C. Weitenberg, M. Endres, J. F. Sherson, M. Cheneau, P. Schauß, T. Fukuhara, I. Bloch, and S. Kuhr, "Single-spin addressing in an atomic mott insulator," *Nature*, vol. 471, no. 7338, pp. 319–324, 2011.

[158] W. S. Bakr, J. I. Gillen, A. Peng, S. Fölling, and M. Greiner, "A quantum gas microscope for detecting single atoms in a hubbard-regime optical lattice," *Nature*, vol. 462, no. 7269, pp. 74–77, 2009.

[159] W. S. Bakr, A. Peng, M. E. Tai, R. Ma, J. Simon, J. I. Gillen, S. Foelling, L. Pollet, and M. Greiner, "Probing the superfluid–to–mott insulator transition at the single-atom level," *Science*, vol. 329, no. 5991, pp. 547–550, 2010.

[160] M. Greiner, O. Mandel, T. Esslinger, T. W. Hänsch, and I. Bloch, "Quantum phase transition from a superfluid to a mott insulator in a gas of ultracold atoms," *Nature*, vol. 415, no. 6867, pp. 39–44, 2002.

[161] J. Stewart, J. Gaebler, and D. Jin, "Using photoemission spectroscopy to probe a strongly interacting fermi gas," *Nature*, vol. 454, no. 7205, pp. 744–747, 2008.

[162] G. Jotzu, M. Messer, R. Desbuquois, M. Lebrat, T. Uehlinger, D. Greif, and T. Esslinger, "Experimental realization of the topological haldane model with ultracold fermions," *Nature*, vol. 515, pp. 237–240, Nov. 2014.

[163] P. Hauke, M. Lewenstein, and A. Eckardt, "Tomography of band insulators from quench dynamics," *Phys. Rev. Lett.*, vol. 113, p. 045303, Jul 2014.

[164] N. Goldman, J. Dalibard, A. Dauphin, F. Gerbier, M. Lewenstein, P. Zoller, and I. B. Spielman, "Direct imaging of topological edge states in cold-atom systems," *Proc. Natl. Acad. Sci.*, vol. 110, no. 17, pp. 6736–6741, 2013.

[165] E. Zhao, N. Bray-Ali, C. J. Williams, I. B. Spielman, and I. I. Satija, "Chern numbers hiding in time-of-flight images," *Phys. Rev. A*, vol. 84, p. 063629, Dec 2011.

[166] J. de Lisle, S. De, E. Alba, A. Bullivant, J. J. Garcia-Ripoll, V. Lahtinen, and J. K. Pachos, "Detection of chern numbers and entanglement in topological multi-component systems through subsystem winding numbers," *New J. Phys.*, vol. 16, p. 083022, Aug 2014.

[167] N. Goldman, E. Anisimovas, F. Gerbier, P. Öhberg, I. Spielman, and G. Juzeliūnas, "Measuring topology in a laser-coupled honeycomb lattice: From chern insulators to topological semi-metals," *New J. Phys.*, vol. 15, no. 1, p. 013025, 2013.

[168] Q. Niu, D. J. Thouless, and Y.-S. Wu, "Quantized hall conductance as a topological invariant," *Phys. Rev. B*, vol. 31, pp. 3372–3377, Mar 1985.

[169] Z. Wang and S.-C. Zhang, "Simplified topological invariants for interacting insulators," *Phys. Rev. X*, vol. 2, p. 031008, Aug 2012.

[170] K. Ishikawa and T. Matsuyama, "Magnetic field induced multi-component qed3 and quantum hall effect," *Z. Phys. C*, vol. 33, no. 1, pp. 41–45, 1986.

[171] G. E. Volovik, *The Universe in a Helium Droplet*, vol. 117. Oxford University Press, 2003.

[172] Z. Wang, X.-L. Qi, and S.-C. Zhang, "Topological field theory and thermal responses of interacting topological superconductors," *Phys. Rev. B*, vol. 84, p. 014527, Jul 2011.

[173] Z. Wang, X.-L. Qi, and S.-C. Zhang, "Topological order parameters for interacting topological insulators," *Phys. Rev. Lett.*, vol. 105, p. 256803, Dec 2010.

[174] V. Gurarie, "Single-particle green's functions and interacting topological insulators," *Phys. Rev. B*, vol. 83, p. 085426, Feb 2011.

[175] A. M. Essin and V. Gurarie, "Bulk-boundary correspondence of topological insulators from their respective green's functions," *Phys. Rev. B*, vol. 84, p. 125132, Sep 2011.

[176] Z. Wang and B. Yan, "Topological hamiltonian as an exact tool for topological invariants," *J. Phys. Condens. Matter.*, vol. 25, no. 15, 2013.

[177] S. R. Manmana, A. M. Essin, R. M. Noack, and V. Gurarie, "Topological invariants and interacting one-dimensional fermionic systems," *Phys. Rev. B*, vol. 86, p. 205119, Nov 2012.

[178] Z. Wang and S.-C. Zhang, "Strongly correlated topological superconductors and topological phase transitions via green's function," *Phys. Rev. B*, vol. 86, p. 165116, Oct 2012.

[179] G. D. Mahan, *Many-particle physics*. Springer, 2000.

[180] A. Damascelli, "Probing the electronic structure of complex systems by arpes," *Phys. Scr.*, vol. 2004, no. T109, p. 61, 2004.

[181] T.-L. Dao, I. Carusotto, and A. Georges, "Probing quasiparticle states in strongly interacting atomic gases by momentum-resolved raman photoemission spectroscopy," *Phys. Rev. A*, vol. 80, p. 023627, Aug 2009.

[182] T.-L. Dao, A. Georges, J. Dalibard, C. Salomon, and I. Carusotto, "Measuring the one-particle excitations of ultracold fermionic atoms by stimulated raman spectroscopy," *Phys. Rev. Lett.*, vol. 98, p. 240402, Jun 2007.

[183] Q. Chen and K. Levin, "Momentum resolved radio frequency spectroscopy in trapped fermi gases," *Phys. Rev. Lett.*, vol. 102, p. 190402, May 2009.

[184] L.-M. Duan, "Detecting correlation functions of ultracold atoms through fourier sampling of time-of-flight images," *Phys. Rev. Lett.*, vol. 96, p. 103201, Mar 2006.

[185] Z. Wang and S.-C. Zhang, "Topological invariants and ground-state wave functions of topological insulators on a torus," *Phys. Rev. X*, vol. 4, p. 011006, Jan 2014.

[186] L. Kelvin, "On vortex atoms," in *Proc. R. Soc. Edin*, vol. 6, pp. 94–105, 1867.

[187] A. D. Bates, A. Maxwell, and O. Press, *DNA topology*. Oxford Univ. Press, Oxford, ed. 2, 2005, 2005.

[188] D. Meluzzi, D. E. Smith, and G. Arya, "Biophysics of knotting," *Annu. Rev. Biophys.*, vol. 39, pp. 349–366, 2010.

[189] K. S. Chichak, S. J. Cantrill, A. R. Pease, S.-H. Chiu, G. W. Cave, J. L. Atwood, and J. F. Stoddart, "Molecular borromean rings," *Science*, vol. 304, no. 5675, pp. 1308–1312, 2004.

[190] D. Han, S. Pal, Y. Liu, and H. Yan, "Folding and cutting dna into reconfigurable topological nanostructures," *Nat. Nanotechnol.*, vol. 5, no. 10, pp. 712–717, 2010.

[191] N. Ponnuswamy, F. B. Cougnon, J. M. Clough, G. D. Pantoş, and J. K. Sanders, "Discovery of an organic trefoil knot," *Science*, vol. 338, no. 6108, pp. 783–785, 2012.

[192] P. G. de Gennes, *Scaling concepts in polymer physics*. Cornell Univ. Press, New York, 1979, 1979.

[193] L. Faddeev and A. J. Niemi, "Stable knot-like structures in classical field theory," *Nature*, vol. 387, no. 6628, pp. 58–61, 1997.

[194] R. L. Ricca, D. C. Samuels, and C. F. Barenghi, "Evolution of vortex knots," *J. Fluid Mech.*, vol. 391, pp. 29–44, 1999.

[195] L. Woltjer, "A theorem on force-free magnetic fields," *Proc. Natl. Acad. Sci.*, vol. 44, no. 6, p. 489, 1958.

[196] Y. Kawaguchi, M. Nitta, and M. Ueda, "Knots in a spinor bose-einstein condensate," *Phys. Rev. Lett.*, vol. 100, no. 18, p. 180403, 2008.

[197] T. Machon and G. P. Alexander, "Knots and nonorientable surfaces in chiral nematics," *Proceedings of the National Academy of Sciences*, vol. 110, no. 35, pp. 14174–14179, 2013.

[198] T. Machon and G. P. Alexander, "Knotted defects in nematic liquid crystals," *Phys. Rev. Lett.*, vol. 113, p. 027801, 2014.

[199] G. P. Alexander, B. G.-g. Chen, E. A. Matsumoto, and R. D. Kamien, "Colloquium: Disclination loops, point defects, and all that in nematic liquid crystals," *Rev. Mod. Phys.*, vol. 84, pp. 497–514, Apr 2012.

[200] R. V. Buniy and T. W. Kephart, "A model of glueballs," *Phys. Lett. B*, vol. 576, no. 1, pp. 127–134, 2003.

[201] E. Witten, "Quantum field theory and the jones polynomial," *Commun. Math. Phys.*, vol. 121, no. 3, pp. 351–399, 1989.

[202] B. Senyuk, Q. Liu, S. He, R. D. Kamien, R. B. Kusner, T. C. Lubensky, and I. I. Smalyukh, "Topological colloids," *Nature*, vol. 493, no. 7431, pp. 200–205, 2013.

[203] U. Tkalec, M. Ravnik, S. Čopar, S. Žumer, and I. Muševič, "Reconfigurable knots and links in chiral nematic colloids," *Science*, vol. 333, no. 6038, pp. 62–65, 2011.

[204] B. G.-g. Chen, P. J. Ackerman, G. P. Alexander, R. D. Kamien, and I. I. Smalyukh, "Generating the hopf fibration experimentally in nematic liquid crystals," *Phys. Rev. Lett.*, vol. 110, no. 23, p. 237801, 2013.

[205] A. Martinez, M. Ravnik, B. Lucero, R. Visvanathan, S. Žumer, and I. I. Smalyukh, "Mutually tangled colloidal knots and induced defect loops in nematic fields," *Nature materials*, 2014.

[206] M. R. Dennis, R. P. King, B. Jack, K. O/'Holleran, and M. J. Padgett, "Isolated optical vortex knots," *Nat. Phys.*, vol. 6, pp. 118–121, Feb. 2010.

[207] D. Kleckner and W. T. Irvine, "Creation and dynamics of knotted vortices," *Nature Physics*, vol. 9, no. 4, pp. 253–258, 2013.

[208] W. T. Irvine and D. Kleckner, "Liquid crystals: Tangled loops and knots," *Nature materials*, vol. 13, no. 3, pp. 229–231, 2014.

[209] X.-L. Qi, R. Li, J. Zang, and S.-C. Zhang, "Inducing a magnetic monopole with topological surface states," *Science*, vol. 323, no. 5918, pp. 1184–1187, 2009.

[210] G. Rosenberg, H.-M. Guo, and M. Franz, "Wormhole effect in a strong topological insulator," *Phys. Rev. B*, vol. 82, no. 4, p. 041104, 2010.

[211] G. Rosenberg and M. Franz, "Witten effect in a crystalline topological insulator," *Phys. Rev. B*, vol. 82, no. 3, p. 035105, 2010.

[212] L. Faddeev, "Quantization of solitons," *Princeton preprint IAS-75-QS70*, 1975.

[213] M. Beeler, R. Williams, K. Jimenez-Garcia, L. LeBlanc, A. Perry, and I. Spielman, "The spin hall effect in a quantum gas," *Nature*, 2013.

[214] L. H. Kauffman, *Knots and physics*, vol. 53. World scientific, 2013.

[215] J. Hietarinta, J. Palmu, J. Jäykkä, and P. Pakkanen, "Scattering of knotted vortices (hopfions) in the faddeev–skyrme model," *New Journal of Physics*, vol. 14, no. 1, p. 013013, 2012.

[216] T. H. R. Skyrme, "A unified field theory of mesons and baryons," *Nucl. Phys.*, vol. 31, pp. 556–569, 1962.

[217] X. Yu, Y. Onose, N. Kanazawa, J. Park, J. Han, Y. Matsui, N. Nagaosa, and Y. Tokura, "Real-space observation of a two-dimensional skyrmion crystal," *Nature*, vol. 465, no. 7300, pp. 901–904, 2010.

[218] U. Rößler, A. Bogdanov, and C. Pfleiderer, "Spontaneous skyrmion ground states in magnetic metals," *Nature*, vol. 442, no. 7104, pp. 797–801, 2006.

[219] M. Aidelsburger, M. Atala, S. Nascimbène, S. Trotzky, Y.-A. Chen, and I. Bloch, "Experimental realization of strong effective magnetic fields in an optical lattice," *Phys. Rev. Lett.*, vol. 107, no. 25, p. 255301, 2011.

[220] N. Goldman and J. Dalibard, "Periodically driven quantum systems: Effective hamiltonians and engineered gauge fields," *Phys. Rev. X*, vol. 4, p. 031027, Aug 2014.

[221] T. Jungwirth, J. Wunderlich, V. Novák, K. Olejnik, B. Gallagher, R. Campion, K. Edmonds, A. Rushforth, A. Ferguson, and P. Němec, "Spin-dependent phenomena and device concepts explored in (Ga,Mn)As," *Rev. Mod. Phys.*, vol. 86, pp. 855–896, Jul 2014.

[222] F. Wilczek, "Majorana returns," *Nat. Phys.*, vol. 5, no. 9, pp. 614–618, 2009.

[223] A. Stern, "Non-abelian states of matter," *Nature*, vol. 464, no. 7286, pp. 187–193, 2010.

[224] J. Hisano, S. Matsumoto, and M. M. Nojiri, "Explosive dark matter annihilation," *Phys. Rev. Lett.*, vol. 92, p. 031303, Jan 2004.

[225] A. Das, Y. Ronen, Y. Most, Y. Oreg, M. Heiblum, and H. Shtrikman, "Zero-bias peaks and splitting in an al-inas nanowire topological superconductor as a signature of majorana fermions," *Nat. Phys.*, vol. 8, no. 12, pp. 887–895, 2012.

[226] L. P. Rokhinson, X. Liu, and J. K. Furdyna, "The fractional ac josephson effect in a semiconductor-superconductor nanowire as a signature of majorana particles," *Nat. Phys.*, vol. 8, no. 11, pp. 795–799, 2012.

[227] M. Veldhorst, M. Snelder, M. Hoek, T. Gang, V. Guduru, X. Wang, U. Zeitler, W. van der Wiel, A. Golubov, H. Hilgenkamp, *et al.*, "Josephson supercurrent through a topological insulator surface state," *Nat. Mater.*, vol. 11, no. 5, pp. 417–421, 2012.

[228] J. Alicea, "New directions in the pursuit of majorana fermions in solid state systems," *Rep. Prog. Phys.*, vol. 75, no. 7, p. 076501, 2012.

[229] C. Beenakker, "Search for majorana fermions in superconductors," *Annu. Rev. Condens. Matter Phys.*, vol. 4, no. 1, pp. 113–136, 2013.

[230] E. J. Lee, X. Jiang, M. Houzet, R. Aguado, C. M. Lieber, and S. De Franceschi, "Spin-resolved andreev levels and parity crossings in hybrid superconductor-semiconductor nanostructures," *Nat. Nanotechnol.*, vol. 9, pp. 79–84, 2014.

[231] M. Lewenstein, A. Sanpera, and V. Ahufinger, *Ultracold Atoms in Optical Lattices: Simulating quantum many-body systems*. Oxford University Press, 2012.

[232] M. Sato, Y. Takahashi, and S. Fujimoto, "Non-abelian topological order in *s*-wave superfluids of ultracold fermionic atoms," *Phys. Rev. Lett.*, vol. 103, p. 020401, Jul 2009.

[233] S. Tewari, S. Das Sarma, C. Nayak, C. Zhang, and P. Zoller, "Quantum computation using vortices and majorana zero modes of a $p_x + ip_y$ superfluid of fermionic cold atoms," *Phys. Rev. Lett.*, vol. 98, p. 010506, Jan 2007.

[234] D. A. Ivanov, "Non-abelian statistics of half-quantum vortices in *p*-wave superconductors," *Phys. Rev. Lett.*, vol. 86, pp. 268–271, Jan 2001.

[235] A. Stern, F. von Oppen, and E. Mariani, "Geometric phases and quantum entanglement as building blocks for non-abelian quasiparticle statistics," *Phys. Rev. B*, vol. 70, p. 205338, Nov 2004.

[236] V. Gurarie, L. Radzihovsky, and A. V. Andreev, "Quantum phase transitions across a *p*-wave feshbach resonance," *Phys. Rev. Lett.*, vol. 94, p. 230403, Jun 2005.

[237] J. P. Gaebler, J. T. Stewart, J. L. Bohn, and D. S. Jin, "*p*-wave feshbach molecules," *Phys. Rev. Lett.*, vol. 98, p. 200403, May 2007.

[238] Y.-J. Han, Y.-H. Chan, W. Yi, A. J. Daley, S. Diehl, P. Zoller, and L.-M. Duan, "Stabilization of the *p*-wave superfluid state in an optical lattice," *Phys. Rev. Lett.*, vol. 103, p. 070404, Aug 2009.

[239] A. Bühler, N. Lang, C. V. Kraus, G. Möller, S. D. Huber, and H. P. Büchler, "Majorana modes and p-wave superfluids for fermionic atoms in optical lattices," *Nat. Commun.*, vol. 5, p. 4504, 2014.

[240] N. Syassen, D. M. Bauer, M. Lettner, T. Volz, D. Dietze, J. J. GarcÃa-Ripoll, J. I. Cirac, G. Rempe, and S. DÃŒrr, "Strong dissipation inhibits losses and induces correlations in cold molecular gases," *Science*, vol. 320, no. 5881, pp. 1329–1331, 2008.

[241] P. Würtz, T. Langen, T. Gericke, A. Koglbauer, and H. Ott, "Experimental demonstration of single-site addressability in a two-dimensional optical lattice," *Phys. Rev. Lett.*, vol. 103, p. 080404, Aug 2009.

[242] M. Wimmer, A. R. Akhmerov, M. V. Medvedyeva, J. Tworzydło, and C. W. J. Beenakker, "Majorana bound states without vortices in topological superconductors with electrostatic defects," *Phys. Rev. Lett.*, vol. 105, p. 046803, Jul 2010.

[243] W. Shockley, "On the surface states associated with a periodic potential," *Phys. Rev.*, vol. 56, pp. 317–323, Aug 1939.

[244] J. Alicea, Y. Oreg, G. Refael, F. von Oppen, and M. P. Fisher, "Non-abelian statistics and topological quantum information processing in 1d wire networks," *Nat. Phys.*, vol. 7, no. 5, pp. 412–417, 2011.

[245] C. V. Kraus, P. Zoller, and M. A. Baranov, "Braiding of atomic majorana fermions in wire networks and implementation of the deutsch-jozsa algorithm," *Phys. Rev. Lett.*, vol. 111, p. 203001, Nov 2013.

[246] J. D. Sau, R. M. Lutchyn, S. Tewari, and S. Das Sarma, "Generic new platform for topological quantum computation using semiconductor heterostructures," *Phys. Rev. Lett.*, vol. 104, p. 040502, Jan 2010.

[247] P. Di Francesco, P. Mathieu, and D. Snchal, *Conformal field theory*. Citeseer, 1997.

[248] X.-J. Liu, M. Wong, Chris L. and T. Law, K. "Non-abelian majorana doublets in time-reversal-invariant topological superconductors," *Phys. Rev. X*, vol. 4, p. 021018, Apr 2014.

[249] J. C. Y. Teo and C. L. Kane, "Majorana fermions and non-abelian statistics in three dimensions," *Phys. Rev. Lett.*, vol. 104, p. 046401, Jan 2010.

[250] E. Majorana, "Teoria simmetrica dellelettrone e del positrone," *Nuovo Cimento*, vol. 14, pp. 171–184, 1937.

[251] A. Kitaev, "Anyons in an exactly solved model and beyond," *Annals of Physics*, vol. 321, no. 1, pp. 2–111, 2006.

[252] R. M. Lutchyn, J. D. Sau, and S. D. Sarma, "Majorana fermions and a topological phase transition in semiconductor-superconductor heterostructures," *Phys. Rev. Lett.*, vol. 105, no. 7, p. 077001, 2010.

[253] Y. Oreg, G. Refael, and F. von Oppen, "Helical liquids and majorana bound states in quantum wires," *Phys. Rev. Lett.*, vol. 105, p. 177002, Oct 2010.

[254] M.-X. Wang, C. Liu, J.-P. Xu, F. Yang, L. Miao, M.-Y. Yao, C. Gao, C. Shen, X. Ma, X. Chen, *et al.*, "The coexistence of superconductivity and topological order in the bi_2se_3 thin films," *Science*, vol. 336, no. 6077, pp. 52–55, 2012.

[255] P. Bonderson, D. J. Clarke, C. Nayak, and K. Shtengel, "Implementing arbitrary phase gates with ising anyons," *Phys. Rev. Lett.*, vol. 104, p. 180505, May 2010.

[256] J. Ackermann, U. Tangen, B. Bödekker, J. Breyer, E. Stoll, and J. McCaskill, "Parallel random number generator for inexpensive configurable hardware cells," *Computer physics communications*, vol. 140, no. 3, pp. 293–302, 2001.

[257] P. F. Hultquist, "A good random number generator for microcomputers," *Simulation*, vol. 57, no. 4, pp. 258–259, 1991.

[258] S.-J. Tu and E. Fischbach, "Geometric random inner products: A family of tests for random number generators," *Phys. Rev. E*, vol. 67, p. 016113, Jan 2003.

[259] N. Gisin, G. Ribordy, W. Tittel, and H. Zbinden, "Quantum cryptography," *Rev. Mod. Phys.*, vol. 74, pp. 145–195, Mar 2002.

[260] S. Pironio, A. Acín, S. Massar, A. B. de La Giroday, D. N. Matsukevich, P. Maunz, S. Olmschenk, D. Hayes, L. Luo, T. A. Manning, *et al.*, "Random numbers certified by bell's theorem," *Nature*, vol. 464, no. 7291, pp. 1021–1024, 2010.

[261] M. Isida and H. Ikeda, "Random number generator," *Annals of the Institute of Statistical Mathematics*, vol. 8, no. 1, pp. 119–126, 1956.

[262] K. Svozil, "The quantum coin toss-testing microphysical undecidability," *Physics Letters A*, vol. 143, no. 9, pp. 433–437, 1990.

[263] J. Rarity, P. Owens, and P. Tapster, "Quantum random-number generation and key sharing," *Journal of Modern Optics*, vol. 41, no. 12, pp. 2435–2444, 1994.

[264] T. Jennewein, U. Achleitner, G. Weihs, H. Weinfurter, and A. Zeilinger, "A fast and compact quantum random number generator," *Review of Scientific Instruments*, vol. 71, no. 4, pp. 1675–1680, 2000.

[265] R. Colbeck, "Quantum and relativistic protocols for secure multi-party computation," *arXiv preprint arXiv:0911.3814*, 2009.

[266] J. F. Clauser, M. A. Horne, A. Shimony, and R. A. Holt, "Proposed experiment to test local hidden-variable theories," *Phys. Rev. Lett.*, vol. 23, pp. 880–884, Oct 1969.

[267] D. N. Matsukevich, P. Maunz, D. L. Moehring, S. Olmschenk, and C. Monroe, "Bell inequality violation with two remote atomic qubits," *Phys. Rev. Lett.*, vol. 100, p. 150404, Apr 2008.

[268] G. Brennen, S. Iblisdir, J. Pachos, and J. Slingerland, "Non-locality of non-abelian anyons," *New Journal of Physics*, vol. 11, no. 10, p. 103023, 2009.

[269] M. Ardehali, "Bell inequalities with a magnitude of violation that grows exponentially with the number of particles," *Phys. Rev. A*, vol. 46, pp. 5375–5378, Nov 1992.

[270] N. D. Mermin, "Extreme quantum entanglement in a superposition of macroscopically distinct states," *Phys. Rev. Lett.*, vol. 65, pp. 1838–1840, Oct 1990.

[271] Belinskiĭ, "Interference of light and bell's theorem,"

[272] S. Pironio and S. Massar, "Security of practical private randomness generation," *Phys. Rev. A*, vol. 87, p. 012336, Jan 2013.

[273] R. Konig, R. Renner, and C. Schaffner, "The operational meaning of min-and max-entropy," *Information Theory, IEEE Transactions on*, vol. 55, no. 9, pp. 4337–4347, 2009.

[274] L. Vandenberghe and S. Boyd, "Semidefinite programming," *SIAM review*, vol. 38, no. 1, pp. 49–95, 1996.

[275] N. Nisan, "Extracting randomness: how and why. a survey," in *Computational Complexity, 1996. Proceedings., Eleventh Annual IEEE Conference on*, pp. 44–58, IEEE, 1996.

[276] C. A. Miller and Y. Shi, "Universal security for randomness expansion," *arXiv preprint arXiv:1411.6608*, 2014.

[277] C. A. Miller and Y. Shi, "Robust protocols for securely expanding randomness and distributing keys using untrusted quantum devices," in *Proceedings of the 46th Annual ACM Symposium on Theory of Computing*, pp. 417–426, ACM, 2014.

[278] A. Ahlbrecht, L. S. Georgiev, and R. F. Werner, "Implementation of clifford gates in the ising-anyon topological quantum computer," *Phys. Rev. A*, vol. 79, p. 032311, Mar 2009.

[279] S. Bravyi, "Universal quantum computation with the $\nu = 5/2$ fractional quantum hall state," *Phys. Rev. A*, vol. 73, p. 042313, Apr 2006.

[280] S. Bravyi and A. Kitaev, "Universal quantum computation with ideal clifford gates and noisy ancillas," *Phys. Rev. A*, vol. 71, p. 022316, Feb 2005.

[281] F. Hassler, A. Akhmerov, C. Hou, and C. Beenakker, "Anyonic interferometry without anyons: How a flux qubit can read out a topological qubit," *New Journal of Physics*, vol. 12, no. 12, p. 125002, 2010.

[282] M. S. Rudner, N. H. Lindner, E. Berg, and M. Levin, "Anomalous edge states and the bulk-edge correspondence for periodically driven two-dimensional systems," *Phys. Rev. X*, vol. 3, p. 031005, Jul 2013.

[283] T. Kitagawa, E. Berg, M. Rudner, and E. Demler, "Topological characterization of periodically driven quantum systems," *Phys. Rev. B*, vol. 82, p. 235114, Dec 2010.

[284] L. Jiang, T. Kitagawa, J. Alicea, A. R. Akhmerov, D. Pekker, G. Refael, J. I. Cirac, E. Demler, M. D. Lukin, and P. Zoller, "Majorana fermions in equilibrium and in driven cold-atom quantum wires," *Phys. Rev. Lett.*, vol. 106, p. 220402, Jun 2011.

[285] D. E. Liu, A. Levchenko, and H. U. Baranger, "Floquet majorana fermions for topological qubits in superconducting devices and cold-atom systems," *Phys. Rev. Lett.*, vol. 111, p. 047002, Jul 2013.

[286] D. Y. H. Ho and J. Gong, "Topological effects in chiral symmetric driven systems," *Phys. Rev. B*, vol. 90, p. 195419, Nov 2014.

[287] J. M. Zeuner, M. C. Rechtsman, Y. Plotnik, Y. Lumer, M. S. Rudner, M. Segev, and A. Szameit, "Probing topological invariants in the bulk of a non-hermitian optical system," *arXiv preprint arXiv:1408.2191*, 2014.

[288] M. S. Rudner and L. S. Levitov, "Topological transition in a non-hermitian quantum walk," *Phys. Rev. Lett.*, vol. 102, p. 065703, Feb 2009.

[289] S. Diehl, E. Rico, M. A. Baranov, and P. Zoller, "Topology by dissipation in atomic quantum wires," *Nature Physics*, vol. 7, no. 12, pp. 971–977, 2011.

[290] R.-J. Slager, A. Mesaros, V. Juričić, and J. Zaanen, "The space group classification of topological band-insulators," *Nature Physics*, vol. 9, no. 2, pp. 98–102, 2013.

[291] X. Chen, Z.-C. Gu, and X.-G. Wen, "Local unitary transformation, long-range quantum entanglement, wave function renormalization, and topological order," *Phys. Rev. B*, vol. 82, p. 155138, Oct 2010.

[292] M. A. Levin and X.-G. Wen, "String-net condensation: a physical mechanism for topological phases," *Phys. Rev. B*, vol. 71, p. 045110, Jan 2005.

[293] M. Freedman, C. Nayak, K. Shtengel, K. Walker, and Z. Wang, "A class of p, t-invariant topological phases of interacting electrons," *Annals of Physics*, vol. 310, no. 2, pp. 428–492, 2004.

[294] G. Moore and N. Read, "Nonabelions in the fractional quantum hall effect," *Nuclear Physics B*, vol. 360, no. 2, pp. 362–396, 1991.

[295] Y.-M. Lu, X.-G. Wen, Z. Wang, and Z. Wang, "Non-abelian quantum hall states and their quasiparticles: From the pattern of zeros to vertex algebra," *Phys. Rev. B*, vol. 81, p. 115124, Mar 2010.

[296] A. Kapustin, R. Thorngren, A. Turzillo, and Z. Wang, "Fermionic symmetry protected topological phases and cobordisms," *arXiv preprint arXiv:1406.7329*, 2014.

[297] T. H. Hsieh, H. Lin, J. Liu, W. Duan, A. Bansil, and L. Fu, "Topological crystalline insulators in the snte material class," *Nat. Commun.*, vol. 3, p. 982, 2012.

[298] P. Dziawa, B. Kowalski, K. Dybko, R. Buczko, A. Szczerbakow, M. Szot, E. Łusakowska, T. Balasubramanian, B. M. Wojek, M. Berntsen, *et al.*, "Topological crystalline insulator states in pb1- xsnxse," *Nature materials*, vol. 11, no. 12, pp. 1023–1027, 2012.

[299] M. Hafezi, S. Mittal, J. Fan, A. Migdall, and J. Taylor, "Imaging topological edge states in silicon photonics," *Nature Photonics*, vol. 7, no. 12, pp. 1001–1005, 2013.

[300] S. Mittal, J. Fan, S. Faez, A. Migdall, M. Taylor, J. and M. Hafezi, "Topologically robust transport of photons in a synthetic gauge field," *Phys. Rev. Lett.*, vol. 113, p. 087403, Aug 2014.

[301] Z.-X. Liu, Z.-C. Gu, and X.-G. Wen, "Microscopic realization of two-dimensional bosonic topological insulators," *Phys. Rev. Lett.*, vol. 113, p. 267206, Dec 2014.

[302] J. Alicea and A. Stern, "Designer non-abelian anyon platforms: from majorana to fibonacci," *arXiv preprint arXiv:1410.0359*, 2014.

[303] K. Mong, Roger S. D. J. Clarke, J. Alicea, N. H. Lindner, P. Fendley, C. Nayak, Y. Oreg, A. Stern, E. Berg, K. Shtengel, and A. Fisher, Matthew P. "Universal topological quantum computation from a superconductor-abelian quantum hall heterostructure," *Phys. Rev. X*, vol. 4, p. 011036, Mar 2014.

[304] C. V. Kraus, M. M. Wolf, and J. I. Cirac, "Quantum simulations under translational symmetry," *Phys. Rev. A*, vol. 75, p. 022303, Feb 2007.

[305] C. V. Kraus, M. M. Wolf, J. I. Cirac, and G. Giedke, "Pairing in fermionic systems: A quantum-information perspective," *Phys. Rev. A*, vol. 79, p. 012306, Jan 2009.